Author:
Orrock, Paulo

Title:
An investigation into the effects of scaling on structural integrity assessments

AN INVESTIGATION INTO THE EFFECTS OF SCALING ON STRUCTURAL INTEGRITY ASSESSMENTS

PAULO JOHN ORROCK

A dissertation submitted to the University of Bristol in accordance with the requirements for award of the degree of Doctor of Philosophy in the Faculty of Engineering

Department of Mechanical Engineering

December 2017

c. 35 000 words

Abstract

The work described in this thesis investigates the effects that scaling has on key structural integrity concepts, namely, stress fields, stress intensity factors, and the J-integral. Scaled models are an attractive concept in scenarios where full scale testing is not possible, and they are used extensively in other engineering fields. Little research into the practical applications of scaling in a structural integrity context exist however, which provided the motivation for the work.

Scaling laws for these three structural integrity parameters are developed, such that the load can be scaled, along with the geometry, while maintaining the parameter of interest. Two sets of experiments and their results are described, which consist of simple aluminium beams in four point bend configurations, to verify the scaling laws for stress fields and stress intensity factors, and to highlight practical issues surrounding scaling in real life.

The scaling laws themselves do not take into account the effect of scaling on the other parameters. As each parameter follows a different law, and as all the parameters are capable of contributing to failure, it is shown that the scaling laws are not capable of describing the behaviour of a component for a complete range of scale factors. By extrapolating results, and with the use of failure assessment diagrams to visualise this, it is possible to see that depending on the geometry, material properties, and loading regime, there will come a point with which the failure mechanisms will change.

There are certain conditions however, in which scaling is an appropriate and useful tool. For specimens where fracture occurs, if the small scale yielding conditions at the crack tip are maintained across the sizes, then scaled models can be reliably used to produce a model that accurately replicates the fracture conditions, and from which results from the scaled model can be transferred across to the full size. For the small scale yielding conditions to be maintained, the limitation will be on how small the scaled model can be made. Similarly for models where failure is due to the global stress field, scaling can be used provided this remains the dominant contributor to failure. Where there are stress concentrating features, care must be taken if the scaled model is larger in sizes than the original specimen, as this can tend towards small scale yielding con-

ditions, and consequently a change in failure mechanism. Where these conditions are met however, then scaled models may confidently be used to replicate and further investigate the failure conditions of the original specimens.

The case studies considered throughout the development of the scaling laws, and in the experiments, are relatively straightforward, and while representative of test specimens used in materials testing, they are not accurate representations of real components. A complex case study is finally considered, which relates the results and findings from the work to a real component, and subject to realistic constraints and boundary conditions. The case study consists of a parametric finite element study, which aims to replicate failure criteria in a scaled down component. The resultant models obtained are able to meet this criteria, however in doing so the geometry is altered, and drifts from what might be considered true scaling. No "all encompassing" scaling law is derived to describe how to produce the scaled component, and prior knowledge of the stress state is required for the parametric study. The methodology is deemed useful, however, for scenarios where full scale modelling is not possible, yet physical validation of the modelling methods are required.

Acknowledgements

First and foremost, my thanks go out to all the members of the Solid Mechanics Research Group for providing a relaxed, fun place to work, especially those I had the pleasure of sitting next to over the course of our five office moves. In particular I'd like to thank Dr Graeme Horne for the extended coffee breaks and late starts, which I used as a template for my own PhD.

I would also like to thank Dr Harry Coules for his collaboration on the complex case study work, discussed in Chapter 6, and whose complicated mechanical models, and knowledge on processing ABAQUS results directly in MATLAB, formed the backbone of the project. His specific contributions are described in more detail in Chapter 6.

Ian Milnes, Steve Harding and Guy Pearne deserve my thanks for all their help in setting up, and carrying out, all the experiments throughout this PhD.

I would like to thank Dr Robert Wimpory, for his help in carrying out the neutron diffraction experiments, and then processing the results afterwards. The extra set of measurements he generously carried out for me in his own time, were greatly appreciated, and they contributed substantially to the later results chapter. I also thank the Helmholtz-Zentrum Berlin for the allocation of neutron beamtime.

This work would not have been possible without the help and support of my supervisor, Professor Chris Truman. His encouragement and advice over the last six years (beginning in the final two years of my undergraduate degree), have been invaluable, and I would not have undertaken this PhD without him. Professor Julian Booker's advice throughout the later stages of this PhD, in particular on the statistical and experimental side, have also been a great help, and I'd like to thank him for carrying out my first and second year reviews, before joining as my supervisor.

Last but not least, I would like to thank my supervisor Professor David Smith. His enthusiasm in the residual stress lectures contributed to my decision to do a PhD, and then later on in project meetings was a huge source of motivation and new ideas. David sadly passed away two years into my PhD.

Author's declaration

I declare that the work in this dissertation was carried out in accordance with the requirements of the University's Regulations and Code of Practice for Research Degree Programmes and that it has not been submitted for any other academic award. Except where indicated by specific reference in the text, the work is the candidate's own work. Work done in collaboration with, or with the assistance of, others, is indicated as such. Any views expressed in the dissertation are those of the author.

Signed: Date:

Publications

The following publications were published during the course of the work presented in this dissertation:

- Orrock, P., Smith, D. J., and Truman, C. E. (2015). A study of the effects of scaling on structural integrity assessment. In *ASME 2015 Pressure Vessels and Piping Conference*. American Society of Mechanical Engineers
- Orrock, P. and Truman, C. E. (2016). A study of the effects of scaling on structural integrity assessment and feasibility of physical validation. In *ASME 2016 Pressure Vessels and Piping Conference*. American Society of Mechanical Engineers
- Orrock, P., Booker, J., and Truman, C. E. (2017). Scaled four point bend specimens and the transferability of their results. In *Proc. 14th International Conference on Fracture (ICF)*
- Coules, H., Orrock, P., and Truman, C. (2017a). Feasibility of reduced-size spinning cylinder specimens for pressurised thermal shock testing. In *ASME 2017 Pressure Vessels and Piping Conference*. American Society of Mechanical Engineers
- Coules, H., Orrock, P., and Truman, C. (2017b). Parametric design of scaled-down pressurised thermal shock test specimens using inelastic analysis. *Engineering Fracture Mechanics*, 176:308–325

Contents

Greek Symbols

β	Shape factor for use in stress intensity factor calculations
δ	Shrink fit interference
θ	Angle
Γ	Contour integral surrounding crack tip
γ_{s}	Specific surface energy
λ	Scale factor
ν	Poisson's ratio
Π	Potential strain energy
ρ	Density of material
ρ_c	Elliptical radius of curvature
ρ_e	Radius pf curvature
σ_A	Stress at tip of ellipse
σ_{c}	Fracture stress
σ_{flow}	Uniaxial flow stress
σ_p^{ref}	Reference stress
σ_{rr}	Radial stresses
$\sigma_{\theta\theta}$	Hoop stresses
σ_{UTS}	Ultimate tensile strength
σ_{y}	Yield stress
ω	Angular velocity

Latin Symbols

a	Half crack length
B	Beam thickness
C	Stiffness matrix
E	Young's modulus
$f\left(a/b\right)$	Shape parameter, a function of a/b
F_i	Ranked value
$\mathcal{G}$	Strain energy release rate
J	J contour integral
K_0	Normalised factor in Weibull distribution
K_I	Mode I stress intensity factor
K_I^P	Mode I stress intensity factor arising from primary loads
K_I^S	Mode I stress intensity factor arising from secondary loads
K_mat	Material fracture toughness
K_min	Minimum value of K_I, below which fracture will not occur
K_r	Proximity to brittle fracture
L_r	Proximity to plastic collapse
L_r^max	Bounding L_r value for use in a failure assessment diagram
m_1	Weibull modulus describing the shape of the distribution

$\hat{n}$	Unit normal
P	Applied load
p	Interface pressure between two surfaces
p_f	Probability function
R_i	Inner radius
R_o	Outer radius
r_p	Radius of plastic zone
S	Probability of failure
s	Arc length when evaluating contour integral
S_o	Outer pin span in a four point bend
S_i	Inner pin span in a four point bend
P_y	The limit load
T	Temperature
t	Thickness
T_0	Initial temperature
$\hat{T}$	Traction vector
$\hat{u}$	Displacement vector
W	Strain energy density
W_S	Energy required for create of new crack surface
x_0	Spacing of atomic planes

List of Figures

List of Tables

Chapter 1

Introduction

1.1 Background

When designing a structure or component, and it is known that it be under a load of some sort during its lifetime, it is important to understand how its structural integrity will be affected, and consequently design with this in mind. The degree of importance the designer attaches to this will, of course, depend on the component, and the impact of its failure. However even for low cost, simple components, this becomes important when dealing with sufficiently large volumes.

It is also important to understand how damage affects structures; in many cases damage is unavoidable, and does not necessarily indicate disaster if it is measured and understood. Flaws and small cracks are an inescapable feature of the welding process (Maddox, 1974), due to the complicated phase changes and variety of material properties involved, but depending on the nature of the material, the cracks and of the loading it will be subjected to, they may never cause any issues.

There are essentially three methods of ensuring the structural integrity of a design, of which a combination should be used:

- Analytical studies and models can be carried out, where analytical solutions for the parameters in question are known, and can be evaluated for the design.

- Finite element models can be carried out, if sufficient information is known about the design that it can be fully modelled. The advantage to this method is that much more complex models can be generated than using analytical solutions (which are sometimes arrived at with the help of finite element analysis (Newman and Raju, 1981)), however they rely heavily on the information provided by the user, and require computing power.

- Lastly, physical or experimental models can be carried out, from which

the results for particular in service scenarios can be found. The model could be of the whole structure, or just part of it, with the appropriate boundary conditions to simulate the environment of interest.

In reality, combinations of the three are typically used; while analytical models are useful where they exist, they are often limited to simple geometries and idealised components. Finite element analysis on the other hand is used ever more frequently, due largely to the rapid increase in the availability of computer processing power, allowing for quick turnarounds and with rising accuracy and resolution.

The drawback to finite element analyses however, is that as already mentioned, they rely entirely on the correct formulation of the problem being investigated. This means that as well as accurate material properties (which itself is not trivial, as these properties can themselves be dependent on other model parameters), the entire model has to accurately depict the real component, with the relevant loads and boundary conditions all carefully defined. The outcome from any of these not being entirely correct, may be a model whose results appear to be completely believable, whilst being entirely wrong; the adage *"garbage in, garbage out"*, is particularly appropriate in this context.

In addition to this, finite element packages are not guaranteed to produce the correct results, even when all the inputs are correct. They are undeniably incredibly powerful, however their foundation is still in the mathematical interpretation of physics and mechanics, which have in turn been programmed by people and therefore susceptible to mistakes or misinterpretation. Updates and revisions to these different software packages are constantly being released, hopefully improving them each time, but a reminder that they are not flawless (Ainsworth and Oden, 1997; Bažant et al., 2012).

The upshot of this is that even with the increasing availability and improvement of finite element solutions, there still remains a need for physical validation and experimentation. In many cases, however, the physical validation can be prohibitively costly and impractical.

A nuclear reactor pressure vessel is one such example. These pressure vessels are comprised (if viewed simplistically) of a steel cylinder, with multiple layers and components attached using welding, and which have to be capable of withstanding extreme conditions, as well as sudden changes in these conditions. What makes the harsh environments they operate in particularly challenging, are the welds which join much of the assembly together, as these are known to be a common cause of failure in engineering components. Understanding the stress state of the pressure vessel, in any of the multitude of scenarios in which it can find itself, is therefore vital. Finite element simulations can give the engineers valuable insight into this, but experimental validation is required in some form too.

The designs of these pressure vessels are understandably closely guarded secrets, however it is relatively common knowledge that they can be extremely large in size, measuring up to 5 m in diameter, and over 12 m in height, with wall thicknesses of 250 mm (Leitz and Koban, 1989). Common sense tells us that a structure of this size cannot be quickly "mocked up", or easily moved into a laboratory to conduct structural integrity tests.

This is where the idea of scaled models comes in. The advantages of being able to produce a scaled model, small enough that it could be used to carry out tests and assess its behaviour, without being prohibitively expensive or impractical, are obvious. Scaled models are already used extensively in other engineering disciplines for exactly these reasons (this is discussed further in Chapter 2), and so this forms the basis of the rest of this work.

1.2 Objectives

The topic of scaling is a broad one which could go in many directions, so a number of objectives are presented here, and which are the focus of this work:

- Determine the current start of scaling research in a structural integrity context.
- Develop simple scaling laws, which can be used in structural tests, highlighting any shortcomings.
- Investigate the feasibility of producing a scaled complex model that can be used in the structural integrity evaluation of a large component.

1.3 Research methodology

The research methodology used in this investigation broadly adopted the three previously described methods of assessing structural integrity, namely, analytical investigation, modelling, and experimental validation, and which are reflected in the individual objectives.

The analytical approach is used to first explain the fundamentals with regards to scaling, establishing the general behaviours of the parameters of interest when scaled. This approach was used so as to arrive at general scaling laws, rather than basing them on complex examples where an understanding of the fundamentals is missing.

Finite element analysis was used to compliment this approach, providing validation for the simple examples utilised in the analytical approach. With the simple examples established, finite element analysis was used to

investigate more complex geometries and loading regimes, providing further validation and allowing an investigation into the limitations of these simple approaches.

Experimental validation was use to verify the analytical and finite element approaches were correct, tying them together, as well as to highlight practical issues surrounding the implementation of these laws in a practical context, which is the final aim listed in the objectives. The nature of experimental work, particularly in this field, where residual stress measurements and fracture are both associated with scatter (Hutchings et al., 2005; Jayatilaka and Trustrum, 1977), would have required substantial significantly more work in order to support the research on its own. Combined with the theoretical and analytical backing, however, experimental validation was a useful tool. Given the practical aims of this work, it was important to have experimental validation so as to investigate the applicability of this research.

A final complex case study was carried out using extensive finite element modelling. The purpose of this investigation was to examine the feasibility of conducting a scaled complex test. No experimental validation was carried out for this, however, data from an earlier case study was available for comparison. This was a very well documented case study, with substantial information and results available, which were used as a benchmark against which the models could be compared, and which was used to inform the final set of models.

1.4 Chapter summaries

The work in this thesis is divided up into chapters, as follows. Chapter 2 addresses the first objective, presenting a review of the available literature on this subject (and other topics relevant to this investigation) and highlighting the areas in which there is room for further work.

Chapter 3 describes the derivation of the simple scaling laws for key structural integrity parameters, using a combination of finite element analysis and analytical solutions. Chapters 4 and 5 present the design of the experiments to further investigate and validate the scaling laws, with an examination of the results and the difficulties encountered.

Chapter 6 addresses the third objective, looking at the feasibility of producing a complex scaled model, as well as its ultimate utility.

Chapter 7 finally discusses the findings from this work, the conclusions that are ultimately drawn in relation to the objectives described above, and the future work that this research points towards.

Throughout this thesis, all finite element simulations were carried out using ABAQUS/CAE 6.12-1 (Dassault Systémes. Vélizy-Villacoublay, 2013). The Python programming language (version 2.7.13 (Rossum, 1995)) was used for the majority of the coding in this work, as well as for interacting

with ABAQUS, via the ABAQUS scripting interface.

Chapter 2

Literature Review

2.1 Introduction

This chapter gives a summary of the currently available literature pertaining not only to the topic of scaling, but also to the some of the more general structural integrity fields that this subject utilises and builds upon. By the end, it should give the reader an idea of where the field currently stands, and in particular highlight the areas in which research is lacking, and which this thesis investigates and addresses further.

2.2 Residual stresses

A natural starting point to the structural integrity topic are residual stresses, defined by Mura (1987) as, self-equilibrated internal stresses which exist as a result of incompatibilities within the bodies, and independently of external loads and constraints. The mechanisms resulting in residual stresses operate over varying length scales, and as such this is often used as a method of categorisation(Withers and Bhadeshia, 2001; Withers, 2007).

Type I These macrostresses equilibrate over length scales in the same order of magnitude as that of the component. The material involved is generally thought of as a continuum (and ignoring the micro or atomic structure) when working with type I stresses.

Type II These stresses equilibrate over the granular scales and as such are also referred to as intergranular stresses. These can occur as a result of varying grain orientations and their resultant characteristics, or as a result of incompatibilities caused by phase transformations.

Type III Finally microstresses are a result of misfit at the atomic level, potentially occurring due to dislocations or microscopic defects giving rise to stresses that equilibrate over microscopic length scales.

The mechanisms behind these different types of residual stress are interlinked, and it is possible to have type III microstresses which in sufficient numbers cause a type I macrostress. The type of scaling considered in this thesis assumes that the microstructure remains unchanged, and so the stress fields are those that over the body as a whole.

Residual stresses are not inherently problematic or damaging and there are many cases where the stresses are introduced intentionally; glass is often tempered to introduce compressive residual stresses at the surface as this impedes crack growth. The compressive surface stresses are balanced by tensile stresses in the interior, resulting in the distinctive complete shattering if a crack does manage to propagate. A similar effect can be achieved chemically by carrying out an ion-exchange, whereby large ions are introduced into the surface of the glass and the resultant misfit producing a compressive residual stress (Withers, 2007; Gy, 2008). Peening produces a similar effect in metals, by mechanically compressing the surfaces so as to introduce a plastically deformed layer, often to add fatigue resistance (Wang et al., 1998a).

Despite their useful applications when introduced intentionally, residual stresses are often an unavoidable by-product of manufacturing and can contribute severely to failure when not accounted for. Just as the described compressive surface stresses can hinder the initial propagation of surface cracks, tensile surface stresses will have the opposite effect. Fatigue life can be strongly affected by the residual stresses present (Webster and Ezeilo, 2001), leading to failures much earlier on than predicted by a normal fatigue analysis (Novovic et al., 2004). Both brittle and ductile fracture are also affected by the residual stresses present, with the failure loads potentially being much lower than predicted if the stresses are not included (Panontin and Hill, 1996).

The associated problems from these residual stresses stem from them being potentially difficult to predict, measure or even detect, which consequently make them hard to design around. Analytical solutions exist for many simple geometries and loading conditions, provided accurate material data is available, and finite element analysis is powerful enough that detailed and complex models can now be carried out, with computing power rapidly becoming a non-issue. The drawback is that these models need to be accurately defined, which in the case of complex procedures such as welding, can be very challenging; welding involves hard to control physical parameters, microstructure changes, energy fluxes and temperature distributions (Smith and Smith, 2017), and progress is still being made in producing reliable models.

In light of the difficulties in predicting residual stresses, physical validation is often required to provide confidence in the modelling methods, as well as for cases where modelling has not been possible. A variety of techniques exist for measuring residual stresses, ranging from fully destruc-

tive methods, to non invasive, with each method having its own set of advantages and disadvantages. The destructive techniques mostly revolve around the principle of mechanical strain relief, whereby deformations are measured during the course of machining in some form, after which it is assumed that the strains have been released, and from which the original stresses can then be back-calculated (Mahmoudi et al., 2009). Non destructive techniques, which include neutron and x-ray diffraction, measure the distortion of the crystallographic structure of the materials, from which the stresses can then be calculated (Hauk, 1997).

Each measurement technique has its own characteristics that make it suitable, or unsuitable, for different measurements. If the measurement has to be carried out in-situ for example, then the neutron diffraction based methods will typically not be possible, as they require dedicated facilities. X-ray diffraction is possible in-situ, but this is limited to measuring surface stresses (Farrell et al., 2010). The size of the component also has to be taken into account, not just because of the space constraints inside the facilities, but because the non destructive methods cannot penetrate as far into materials as many of the destructive methods can.

2.3 Fracture mechanics

2.3.1 Introduction

Following on from residual stresses, this next section looks at another key structural integrity topic, fracture mechanics. This is an entire subject in its own right, and deals with the behaviour of a structure containing a notch, flaw or stress concentrator, in the presence of stresses. The nature of fracture means that when failure occurs, it can often appear to be instantaneous, and which has resulted in many notable catastrophic failures.

A frequently touted famous example is that of the Liberty ships, built during the Second World War, which suffered from hundreds of fracture problems, including some dramatic failures where the fracture resulted in the boats completely splitting in half. The cause of these failures was eventually found to be welding used in assembling the hulls, which had replaced the previously used technique of riveting. The welding was a problem as it not only introduced a multitude of unseen cracks inside the weld, but also allowed for these cracks to then propagate all the way through the hull, where they would previously have been stopped at the interface between the two adjoining yet separate sheets. The problem was worsened by square hatches containing sharp corners, which we now know to be stress concentrators, and low toughness steel (Anderson, 2017).

What follows is a description of how the field has developed, from a history of analysing failures, to designing structures with an understanding

of the materials processing methods used, so as to avoid these catastrophic failures. This does not always translate to manufacturing components or structures with no flaws or stress concentrators, but instead to understanding how they will behave in the presence of the unavoidable defects, and so to ensure the designs account for them.

2.3.2 Linear elastic approaches

In an idealised elastic material, the energy required for fracture to occur is described by the force required for the separation of the material at the atomic level (i.e. the breaking of the atomic bonds), and for the creation of two new surfaces. In this case the fracture stress, σ_c, would be described by:

$$\sigma_c = \left(\frac{\gamma_s E}{x_0}\right)^{0.5}, \tag{2.1}$$

where γ_s is the specific surface energy, E is the Young's modulus and x_0 is the spacing of the atomic planes (Orowan, 1949).

Experiments demonstrated that in reality this was not the case, and that the force required was significantly lower, leading to the conclusion that there must be additional factors at play besides the inherent strength of the atomic bonds. This led Griffith (1921) to introduce the idea that this *"weakness of isotropic solids"* must be due to flaws contained within the material acting to significantly the failure loads, and theorised that without these the strength of a material could be increased by an an order of magnitude.

It was already known at this time that geometry affected the distribution of stresses, and that features could act as stress concentrators. An early analysis by Inglis (1913) had looked at elliptical holes in plates, and derived that the stress at the tip of the ellipse, σ_A, when loaded under a remote stress field, σ, was equal to

$$\sigma_A = \sigma\left(1 + 2\sqrt{\frac{a_e}{\rho_c}}\right), \tag{2.2}$$

where ρ_c is the radius of curvature at the end of the major axis of the ellipse and is equal to

$$\rho_c = \frac{b_e^2}{a_e}, \tag{2.3}$$

and $2a_e$ and $2b_e$ are the major and minor axes respectively (in this case the major axis becomes the crack length). The problem with this method is that cracks can be described as being elliptical, where $2a_e \gg 2b_e$ and ρ_c tends to zero, and as such the stresses at the crack tip from Eq. (2.2) tend to infinity. Clearly this is an impossibility, as the result of this would suggest that the slightest application of load would cause a hugely increasing stress at the tip of the crack, resulting in immediate failure.

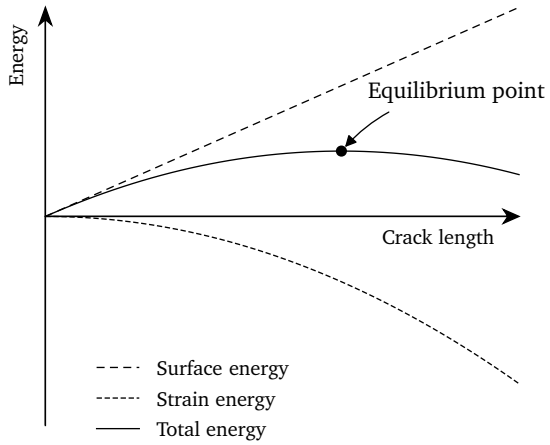

Figure 2.1: An illustration of the critical point during crack growth due to energy changes

Griffith addressed this infinite stress problem by devising an energy based criterion to describe the phenomena, whereby the energy in a system experiencing stable crack is described by:

$$\frac{dE}{dA} = \frac{d\Pi}{dA} + \frac{dW_S}{dA}, \tag{2.4}$$

where E is the total energy contained in the system, Π is the potential strain energy and W_S is the energy associated with the creation of the new crack surfaces. As the crack grows the body releases potential strain energy, but also absorbs energy in the formation of new surfaces. As long as the released strain energy is smaller than the amount of energy required for the formation of crack surfaces then the crack is considered to be stable. If this point is surpassed however then energy required to produce new surfaces can be obtained entirely from the released strain energy and the crack can grow unstably.

In order to obtain a failure stress from Eq. (2.4) Griffith used the stress analysis conducted by Inglis for a crack in an infinite place to calculate the potential stain energy component, which he gave as:

$$\Pi = -\frac{\pi\sigma^2 a^2 B}{E}, \tag{2.5}$$

where $2B$ is the plate width and $2a$ is the crack width. The second part of the equation, the crack surface energy, is given by:

$$W_S = 4aB\gamma_S, \tag{2.6}$$

with the factor of 4 arising due to the crack consisting of two matching surfaces. Substituting Eqs. (2.5) and (2.6) into Eq. (2.4) and differentiating gives:

$$\frac{dE}{dA} = 2\gamma_S - \frac{\pi\sigma^2 a}{E}. \tag{2.7}$$

2.3.3 The stress intensity factor

Building on the work by Griffith, and taking Eq. (2.4), Irwin (1956) defined a new parameter, $\mathcal{G}$, which he called the strain energy release rate, and defined as:

$$\mathcal{G} = -\frac{d\Pi}{dA}. \tag{2.8}$$

Following on from this, Irwin then used $\mathcal{G}$ as a way of quantifying the stress condition at the crack tip, while continuing to use the analysis that predicted infinite stresses at the root of the crack. Using an earlier analysis by Westergaard (1939), in which he analysed the stress distribution in a centre cracked infinite plate subject to a uniform tension, using a cartesian complex number coordinate system, Irwin proposed a form using a polar coordinate system, which described the stresses at a distance, r, and angle, θ, ahead of the tip. He produced the generalised form of this equation,

$$\begin{bmatrix}\sigma_{xx}\\ \sigma_{yy}\\ \tau_{xy}\end{bmatrix} = \left(\frac{\mathcal{G}E}{\pi}\right)^{0.5} \frac{\cos\theta}{\sqrt{2r}} \begin{bmatrix}1 - \sin\frac{\theta}{2}\sin\frac{3\theta}{2}\\ 1 + \sin\frac{\theta}{2}\sin\frac{3\theta}{2}\\ \sin\frac{\theta}{2}\cos\frac{3\theta}{2}\end{bmatrix}, \tag{2.9}$$

of which he then referred to the $\sqrt{\mathcal{G}E/\pi}$ part as being the intensity factor, which we now refer to as K_I (Irwin, 1957; Hayes, 1975).

The companion failure parameter to the stress intensity factor is the fracture toughness, K_IC, the critical value at which a linear elastic material will theoretically fail. Analytical solutions to specific geometries and loading systems exist, typically in the form of:

$$K_\mathrm{I} = P\sqrt{\pi a}\beta, \tag{2.10}$$

where P is the applied load, and β is a shape function which covers both the specimen geometry, and the application of the load.

2.3.4 The J-integral

This section briefly introduces the J-integral, which was first introduced by Rice (1967, 1968), as a parameter that could overcome the limitations of assuming a perfectly elastic response when using K_I.

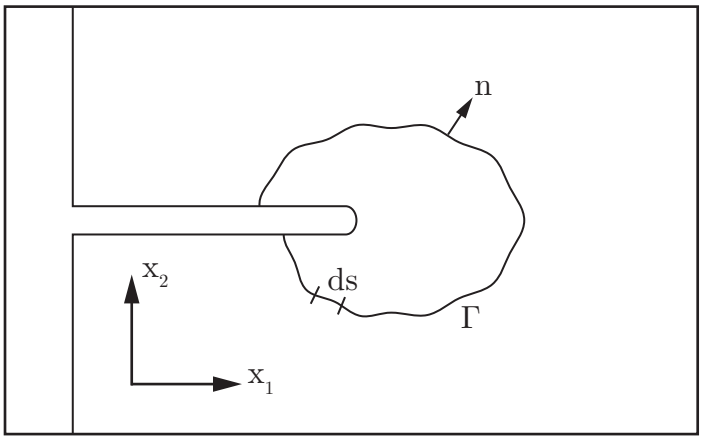

Figure 2.2: Schematic of the J-integral parameters

The J-integral was originally described as a path independent contour surrounding a crack tip, as shown in Fig. 2.2, describing the energy decrease rate (with respect to crack length, as opposed to time). It was defined as:

$$J = \int_{\Gamma} \left(W \, dy - \hat{T} \frac{\partial \hat{u}}{\partial x} \, ds \right), \tag{2.11}$$

where Γ describes a contour completely enclosing the crack tip, W is the strain energy density, $\hat{u}$ is the displacement vector and s is the arc length across the contour Γ. $\hat{T}$ is the traction vector, defined with respect to the unit vector $\hat{n}$, normal to Γ, such that:

$$\hat{T} = \hat{\sigma} \cdot \hat{n}, \tag{2.12}$$

where so that $\hat{T} = 0$ at the crack surface. The strain energy density, W, is a function of the stresses and strains in the body,

$$W = \frac{1}{2} \sigma_{ij} \varepsilon_{ij}. \tag{2.13}$$

The J-integral can be calculated by monitoring crack growth, and load displacement curves (Begley and Landes, 1972), and experimental validation using this method confirmed that the J-integral was suitable as a fracture criterion even in the presence of crack tip yielding (Kobayashi et al., 1973).

With advances in computing power and technology, the J-integral is able to be calculated in-situ using digital image correlation, which can provide full field strain measurements for a loaded component (Becker et al., 2012), as well as with relative ease using finite element analysis.

2.4 Failure assessment diagrams

2.4.1 Introduction

The nature of structural integrity work means that the safety of a structure is often being assessed. The R6 Procedure (British Energy Generation Ltd., 2000) is a methodical approach used by the British Nuclear industry, for the assessment of the structural integrity of components that potentially contain defects. It considers a wide range of loading regimes, in a multitude of different configurations common to nuclear reactors, to help establish whether a component will fail or not, using a number of different assessment procedures.

One such procedure is the failure assessment diagram (FAD), which provides a graphical method of determining the safety of a component using varying degrees of confidence, and ultimately providing the user with a simple "safe" or "unsafe" result. By taking into account the degree of plasticity or brittleness in the failure of a component, they also provide a convenient way of visualising the failure mechanism of a component. The parameters that make up the failure assessment diagram are described here, along with the procedure used to generate them

2.4.2 K_r and L_r

The x and y axes of a failure assessment diagram use two parameters to define the safety of a component, L_r and K_r, which refer to the component's proximity to plastic collapse, and proximity to brittle fracture, respectively. L_r is defined as:

$$L_r = \frac{P}{P_y}, \tag{2.14}$$

where P is the applied load and P_y is the limit load causing plastic collapse of the defect containing component. It can alternatively be defined using a reference stress σ^p_{ref} as:

$$L_r = \frac{\sigma^p_{\text{ref}}}{\sigma_{\text{y}}}, \tag{2.15}$$

where σ_{y} is the yield stress (Ainsworth et al., 2000).

The next parameter, K_r, is defined as:

$$K_r = \frac{K_{\text{I}}}{K_{\text{mat}}}, \tag{2.16}$$

where K_{I} is the applied linear elastic stress intensity factor, and K_{mat} is the material fracture toughness. K_{I} is comprised of the stress intensity factors for primary and secondary stresses, and so Section 2.4.2 becomes:

$$K_r = \frac{K^P_{\text{I}} + K^S_{\text{I}}}{K_{\text{mat}}} + \rho, \tag{2.17}$$

where K_{I}^{P} and K_{I}^{S} are the stress intensity factors for primary and secondary stresses respectively, and ρ is a factor introduced to cover the interaction between the two types of stresses.

2.4.3 Curve calculation procedures

The R6 procedure gives three different methods for calculating the FAD curves, each one less conservative than the last, but requiring more information to generate:

Option 1 The option 1 curve is empirical and the easiest of the three curves to apply, requiring only the limit load to draw. The function is given by:

$$f_1(L_r) = \left(1 + 0.5L_r^2\right)^{-1/2} \left(0.3 + 0.7 \exp\left[-0.6L_r^6\right]\right). \tag{2.18}$$

The option 1 curve is the most conservative and does not take geometry or detailed material properties into account.

Option 2 The second curve is less conservative, but requires more information. The function is given by:

$$f_2(L_r) = \left(\frac{E\varepsilon_{\mathrm{ref}}}{L_r\sigma_{\mathrm{y}}} + \frac{L_r^3\sigma_{\mathrm{y}}}{2E\varepsilon_{\mathrm{ref}}}\right)^{-1/2}, \tag{2.19}$$

where E is the Young's modulus and $\varepsilon_{\mathrm{ref}}$ is the true reference strain.

Option 3 The third curve is the most computationally expensive, but least conservative of the three, as it takes into account both geometry and elastic-plastic behaviour. The curve is defined by:

$$f_3(L_r) = \left(\frac{J_{\mathrm{e}}}{J}\right)^{1/2}, \tag{2.20}$$

where J_{e} refers to the elastic J-integral value for a given L_r. This typically requires elastic and elastic-plastic finite element analyses be carried out to obtain the specific J-integrals.

The option 1 curve is derived from the option 2 curve using material properties for a range of austenitic steels, intended as a lower bound approximation for geometry independent steel components (Budden, 2006). Given R6's use in the nuclear industry, where austenitic stainless steels are frequently used, the option 1 curve may suffice.

For cases however, where the stress intensity factors are suspected of being dependent on the geometry of the component, as well as the geometry of the flaw, it is advisable to use the option 3 curve (Smith, 2000).

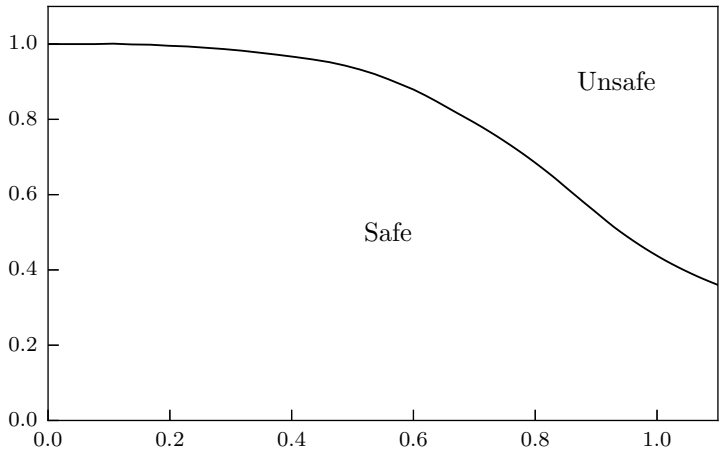

Figure 2.3: An example option 3 FAD for an arbitrary geometry, showing the safe and unsafe zones

All three curves are bound by $L_r^{\max}$, such that

$$K_r = f(L_r) \text{ for } L_r < L_r^{\max} \tag{2.21}$$

$$\text{and } f(L_r) = 0 \quad \text{for } L_r \geq L_r^{\max}, \tag{2.22}$$

and $L_r^{\max}$ is given by:

$$L_r^{\max} = \frac{\sigma_{\text{flow}}}{\sigma_{\text{y}}}, \tag{2.23}$$

where σ_{flow} is the uniaxial flow stress.

An example option 3 FAD for an arbitrary geometry is shown in Fig. 2.3, with the safe and unsafe zones marked. With the curves drawn, an assessment would typically involve calculating the K_r values for the specified L_r values, which would then be plotted on the FAD. Any points falling outside the curve in the unsafe area would be deemed to be unsafe, with degree of plasticity and brittleness being dictated by where the component crossed the curve. The coloured areas highlight the conservatism of the options 1 and 2 curves, showing how a component that would be deemed safe using the more in depth option 3 analysis, would be deemed unsafe.

2.5 Scaling

2.5.1 Introduction

The final topic discussed here is that of scaling. Throughout the majority of this work, the term scaling refers to geometric scaling, where all key dimensions in the structure or system are multiplied by one common scale factor.

The main exception to this is in Chapter 6, where a more general approach to scaling is taken, and which is discussed further later.

Scaling is not a new concept, and is already used extensively in other fields; wind tunnels are commonly used in aerodynamic research to measure reaction forces and the effects on flow, and whilst there do exist very large tunnels, work is frequently required on structures that are impractically large and where it is easier to use a scaled model, such as in the case of offshore wind turbines. Bottasso et al. (2014) describe the case of a 90 m diameter wind turbine rotor, which is scaled by a factor of $1/45$ to produce a 2 m diameter scaled rotor model for use in the wind tunnel. The designing of the International Space Station required the use of scaled models for the assessment of its dynamic behaviour; the final structure was too large for the available testing facilities at the time, and testing at full size also introduced the problem of weight that would not be present in orbit (Gronet et al., 1989). Scaled models are frequently used in fluid dynamics, such as in the case described by Eik and Marchenko (2010), where a tow tank was used with a $1/40$ scale model to investigate the towing of dangerous icebergs using towing vessels.

The above examples all stem from the need to understand the dynamic behaviour of large structures, where it was impractical or not possible to conduct the experiments at full size. One thing they all have in common is the need for careful interpretation of the data, as the results produced at a small scale are not directly applicable to the large scale, or any size in between. The fluid dynamics examples for instance use dimensionless numbers, including Froude, Lock and Reynolds, to allow for the results at one scale to be translated to another. While there has been extensive research into these dynamic problems, research into the scaling of static problems, in particular focusing on structural integrity applications, is more limited. A review is presented here.

2.5.2 Previous work and current applications

When deriving scaling laws, the general purpose is to relate how one size behaves in comparison to another, and so either translate the results, or design the experiment such that the desired results are achieved. One of the first recorded mentions of the idea that the structural behaviour of a material might be influenced by its size, and therefore that scaling laws might be required, is attributed to Leonardo da Vinci, who noted that *"Among cords of equal thickness, the longest is the least strong"* (Williams, 1957). The mechanisms for this were not understood at the time, but it was the first recorded mention of there being a size effect associated with structural strength. Centuries later, this observation was addressed further by Griffith (1921), in the same paper as described in Section 2.3.2, who observed that the apparent tensile strength of wires was inversely proportional to the cross sectional

area, leading him to the conclusion of internal flaws being present.

Not long after, Weibull (1939) approached the problem, as he did not consider the available theories at the time as providing a full explanation for what he perceived as the inconsistencies in breaking stresses, noting that *"experimental measurements give many results which may hardly be brought to agree with this theory"*. Instead, Weibull proposed a statistical approach, using the classical theories to predict failure.

He presented a thought experiment, where a bar of length l and cross sectional area A would rupture under tension at a load P, which would produce a uniform stress of σ across the cross sectional area. Repeating this test using the same geometry and dimensions would produce a different failure load, and given enough tests a distribution would form around a mean failure load and failure stress.

Weibull then defined the probability of rupture for a given stress as $S = f(\sigma)$, where $S = 0$ for very low stresses and $S = 1$ for very high stresses. S_1 in Fig. 2.4a represents this function, with σ_1 corresponding to a probability of 0.5, i.e. if a large number of specimens are loaded to σ_1 then approximately half will fail and half will survive.

If the loaded bar were to then be replaced with a system consisting of two identical bars connected in parallel and the whole system now loaded by $2P$, the internal stress would still be equal to σ. In this new system however, if either bar should fail, then the load on the other one would be doubled and would almost certainly fail too. The survival of the system as a whole in that case would depend on neither bar failing. If the probabilities of each bar failing are given by S_1 and S_2, then the probabilities of both surviving are given by:

$$1 - S_{12} = (1 - S_1) \cdot (1 - S_2) \tag{2.24a}$$

$$= (1 - S_1)^2 , \tag{2.24b}$$

(noting that $S_1 = S_2$) which can be written using logarithms as:

$$\log (1 - S_{12}) = 2 \log (1 - S_1) , \tag{2.24c}$$

and so for the previous stress of σ_1, which corresponded to a probability of a single bar failing of 0.5, the probability of survival of the two bar system would now be 0.25. Weibull observed that this result would also apply to two bars joined in series, again loaded by P, so as to cause a stress of σ_1, and which would again lead to

$$\log (1 - S_{12}) = 2 \log (1 - S_1) , \tag{2.25}$$

which can also be seen in Fig. 2.4a. He then extended this argument to say that the if a distribution, S_1, is known for a unit length, then the probability of survival for for any length, L, can be known via:

$$\log (1 - S_L) = L \cdot \log (1 - S_1) . \tag{2.26}$$

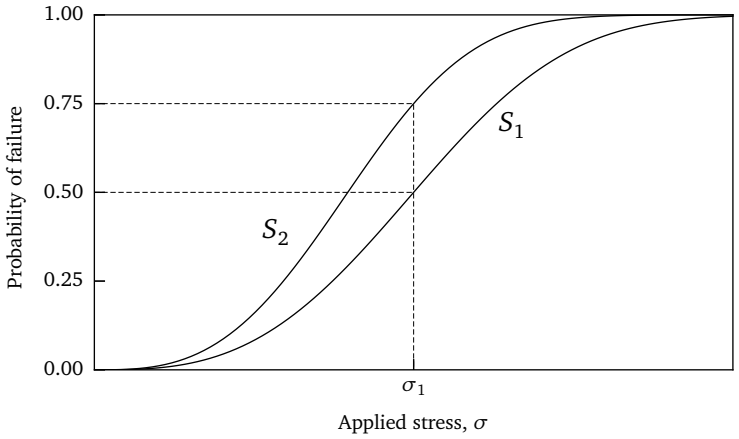

(a) An comparison of the Weibull failure curves for a single and two bar system (reproduced from (Weibull, 1939))

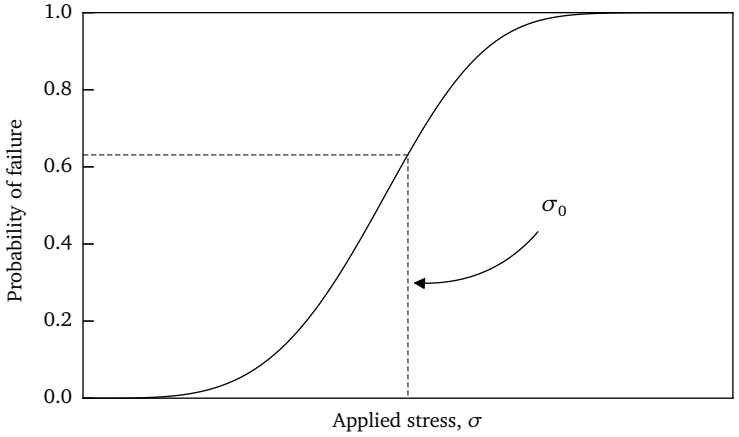

(b) An example of a typical Weibull cumulative distribution function

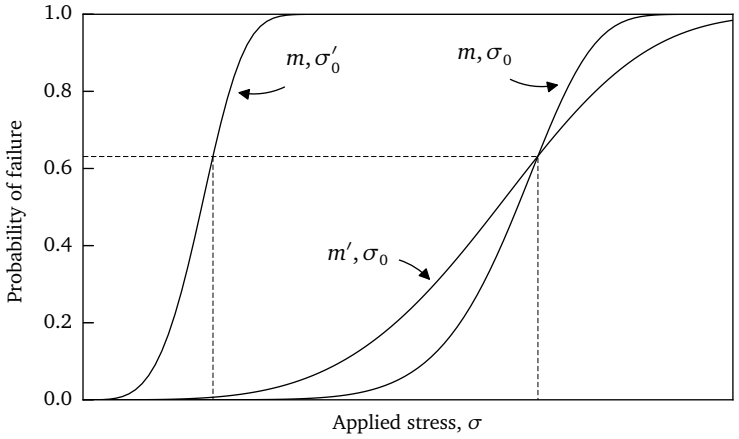

(c) Showing the effect of varying the key parameters in a Weibull cumulative distribution function

Figure 2.4: Three different Weibull cumulative distribution curves

Likewise, if S_0 is said to correspond to the probability of failure of a volume element, then probability of survival for a volume, V, could be said to be equal to:

$$\log(1-S) = V \cdot \log(1-S_0). \tag{2.27}$$

The probability $(1-S_0)$ is an unknown function of the applied stress, σ. If $\log(1-S)$ denotes the probability of survival, then we can define a probability of failure, which Weibull called B, as simply:

$$B = -\log(1-S). \tag{2.28}$$

From that, we the probability of survival for a volume element, dv, is given by:

$$dB = -\log(1-S_0)\, dv \tag{2.29}$$

The right hand side of the equation is purely a function of the applied stress, σ, and so can be replaced by $n(\sigma)$. By integrating Eq. (2.29) with respect to a a volume element, dv, Weibull produced the general formula for the probability of survival of a volume as:

$$B = \int n(\sigma) dv, \tag{2.30}$$

which can then be substituted into Eq. (2.28) and rearranged to give,

$$S = 1 - e^{-\int^V n(\sigma) dv}, \tag{2.31}$$

where $n(\sigma)$ is a material function. Using experimental data he was able to determine that the $n(\sigma) = k\sigma^m$ produced close agreement, with k and m being material constants. Substituting this into Eq. (2.31) and solving produced the following well known equation:

$$S = 1 - e^{-V(\sigma/\sigma_0)^m} \tag{2.32}$$

where σ_0 corresponds to the stress giving the probability of rupture of 0.63. Equation (2.32) is now known as the Weibull distribution, and is used in relating the size to scatter of fracture based failures. Figure 2.4b shows a typical Weibull plot, with Fig. 2.4c showing the effect that varying σ_0 and m has on the distributions, where $m' > m$, and $\sigma_0' < \sigma_0$.

In the past few decades there has been a focus on thickness based sized effects, i.e. how changing the thickness (in the direction of the crack front) affects fracture. A paper by Wallin (1985) specifically addressed what he viewed as the lack of consensus on the issue in the context of fracture experiments, and the conflicting reports on the thickness effect, with some reporting an apparent increase in toughness as the specimen thickness was reduced, with others reporting no change at all. Wallin approached it by

considering the fundamentals of fracture, focusing on brittle and ductile fracture as separate mechanisms.

For brittle fracture, he cited the weakest-link reasoning used by Weibull, where in a thin specimen there was a statistically lower chance of there being a critical defect or flaw along the crack, along with a decrease in stress triaxiality, which together would have the effect of an apparent increase in toughness. He proposed a simple correction factor that could be used in cases of purely brittle fracture to account for this however.

For ductile fracture, he examined the two most commonly used parameters, J and K_{I}. Using finite element analysis, he observed that for normal specimen geometries, the highest values were always observed in the centre of the crack front, i.e. in the middle of the specimen, and that this could be approximated by the plane strain value. He found that this remains true in the centre of even very thin specimens, and so if the specimens were to fail at a critical value of J or K_{I}, then this should be independent of thickness.

Ductile fracture involves a particular failure mechanism, microvoid coalescence, whereby microvoids become elongated and distorted, before merging into unified larger voids, when under large strains (Beachem and Meyn, 1968). Being highly dependent on the maximum strain along the crack front, it would clearly form at the centre of the specimen, where his modelling has confirmed the highest strains were always to be found. Given how the strains there were always in a state of plane strain, they would be unaffected by the thickness of the specimen, and consequently ductile fracture would be unaffected by a thickness effect.

Scaling at the small scale

A number of authors have focussed on the limitations of the thickness effect, which presents itself when the thicknesses in question approach the same orders of magnitude as those of the microstructure. Engelen et al. (2006) provided a critique of the available literature concerning the behaviour of metals when considering dimensions in the micrometre length scale. At these thicknesses, they noted that flow strength appeared to increase as the thickness of the specimen was reduced; similarly, the hardness of metals appeared to increase as the indenter size was reduced in hardness tests, when using indenter sizes in the order of microns. Torsion tests carried out on thin wires followed this trend, with shear strength appearing to increase as the radius of the wire was reduced, and bending tests performed using foils showed an increasing strength as the thickness of the foil was decreased.

As the classical plasticity theories did not account for these behaviours, they turned higher-order strain theories, which included not just strains, but strain gradients, in their analyses of stress states. These theories are only applicable at specific length scales, between approximately 0.1 to 10 µm; below these lengths, the dislocations in the material which contribute to hardening

(Taylor, 1934), become so large relative to the length scales, and of such density, that they are no longer able to be regarded as part of a continuum, and instead have to be regarded as discrete entities to which these models no longer apply (Fleck and Hutchinson, 1997). At these lengths scales though, the strain gradients occur over distances which are not far removed from those of the individual grains and dislocations, leading to this size affect (Fleck et al., 1994).

This area of research, focussing on the very small scale brittle failures, was also investigated by (Danzer, 2006), specifically looking at the effects on ceramic components. This area is becoming increasingly important in electronic applications, as the size of components, which undergo continual cyclic thermal loading, are gradually reducing in size. Performing an analysis on existing sets of fracture data, and then a theoretical analysis, he came to the conclusion that for extremely small components, where the volumes being considered are in the order of 10^{-4} mm. At these sizes, he argued that the flaw size and distribution density, predicted by Weibull statistics for the analysed data, would be so small that flaw interactions would begin to dominate the behaviour of the material, and consequently that a modified form of the theory was needed to explain material strength at this size.

Similar work on the failure of the available methods at small sizes was carried out by Morel (2007), who focussed on using the R-curve rather than Weibull statistics in the analysis of quasi-brittle materials; quasi-brittle materials, such as concrete, exhibit micro-cracking ahead of the main crack that causes them to behave differently during fracture to perfectly brittle materials, and not be accurately modelled using Weibull statistics (Labuz and Biolzi, 1998).

The R-curve, which was developed by Irwin and Kies (1954), is a graphical representation of a crack's resistance to growth, taking into account geometry and loading (Heyer, 1973). Morel found that more complicated analyses would be needed to fully account for the scaling of quasi-brittle structures, but concluded that the current theories had the advantage of always underestimating the nominal strength, should safety be an issue.

More general size effects, and the work of Bažant

The work on the effects of scaling described up till now have largely focused on the limitations of the classical theories at the extreme end, in particular focussing on when the size approaches that of the internal microstructure. In more recent years however, there has been an increasing amount of work looking at more general size effects, and how components or tests can be miniaturised, and the results extrapolated or interpreted. One author in particular who has been heavily involved in this topic is Zdeněk Bažant, and some of his work is presented here. As with a lot of the previous research however, much of the focus has been on quasi-brittle materials. Bažant de-

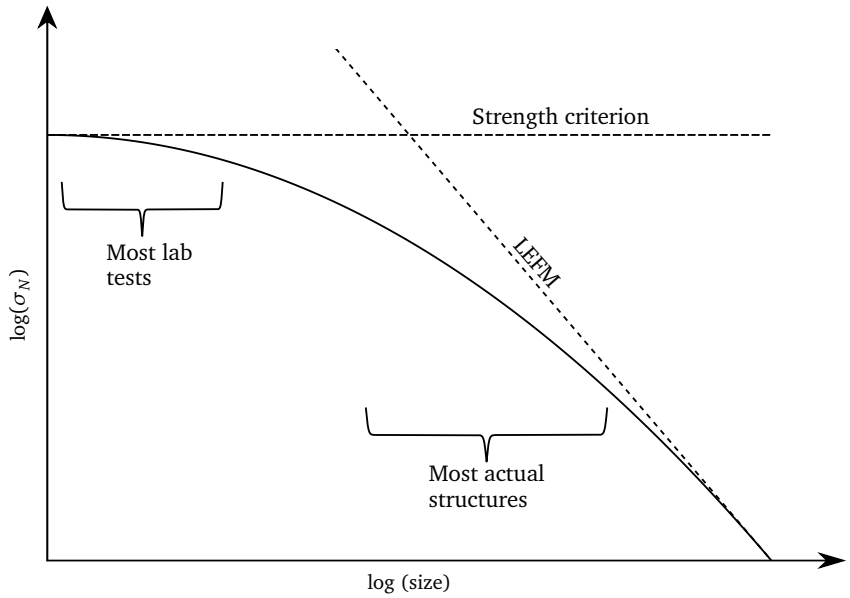

Figure 2.5: Bazant's scaling laws, showing where there was a lack of data, reproduced from Bažant (2005)

scribes these materials as having typically brittle properties, but which are capable of displaying the energy absorbing characteristics of elastic-plastic materials through micro-cracking ahead of the crack tip, and which consequently can be compared with elastic-plastic materials (Bažant, 2000).

One such comparison he made was with front blunting during fracture, either by micro-cracking in quasi-brittle materials, or yielding in elastic-plastic metals. By analysing experimental data carried out by Walsh (1979) on an assortment of concrete fracture specimens, he determined that the classical theories of plasticity and fracture could not be completely extrapolated down to very small, or very large sizes. He also noted that there was a lack of data available for the larger scales at which the failure mechanisms might start to transition (Bažant, 1984), as shown in Fig. 2.5, where he plotted his analysis of the size effect and highlighted where he viewed there to be a lack of test data

A more complex case of fracture he looked at was as part of a project where the failures were in the form of metal-composite joints, where the fractures occurred at stress concentrating corners as opposed to at notches. The focus was again on the size effect, however the use of corners was interesting as the stress concentrator was in this case a dimensionless feature. Using a series of finite element models, and energy release rate analyses, the authors found that there was a strong size effect in these cases; they determined that as the scale factor tended to 0, the model failures became almost entirely dependent on the material strength, whereas when the scale factor tended to infinity, fracture would take over. They also found that these

scaling effects were dependent on the sharpness of the corner, and that as the filleting at the corner was increased, the scaling effects were less pronounced (Le et al., 2010).

A number of effects that are indirectly a result of scaling, were also described (Bažant and Chen, 1997):

- The Poisson effect, describing how plane strain can only exist internally within a specimen and not at its surface (Bažant et al., 1986).
- Stress singularities where a crack meets the surface of the structure, and how the behaviour of the stresses here are different to the internal stresses inside the material.
- Time dependent effects due to diffusion, both physical, e.g. of water and chemicals, though this mostly affects porous materials, and of energy, e.g. the diffusion of heat, and how the time scales associated with these are affected by scaling, consequently affecting cracking.
- Scaling will also affect other time dependent physical phenomena, such as creep and strain softening, which will ultimately lead to a size effect on failure in some way.

These size effects are clearly important as they affect the way a structure may fail, however the last two in particular are beyond the scope of this thesis to fully address; whilst diffusion processes are clerly related to the structural integrity of a component, to provide focus, the work in this thesis addresses the material as a continuum.

2.6 Summary

As stated in the Introduction in Chapter 1, the objectives of this work are to investigate the effects of scaling, and in particular focus on the feasibility of producing a scaled model for use in structural integrity tests, and from which useful information can be gleaned.

Some of the main parameters used in structural integrity assessments have been discussed, namely residual stresses, and those that pertain to fracture mechanics, K_{I} and J. The fundamental theory behind these parameters is a relatively well understood area, that has matured over the last few decades, however there are still advances to be made in the interaction between them, and their applicability to non-idealised materials. The parameters describe the state of the stresses and energy within the component, and so provide a meaningful way of characterising the effects of scaling.

On the actual subject of scaling, the majority of the work has also been carried out over the last few decades, which ins unsurprising given how it builds upon fracture mechanics work, which is also a reasonably new

field. A large amount of work already exists, and is currently ongoing, on the subject of scaling at the very small scale. The motivation behind a lot of this research is the increasing use of small (and continually decreasing in size) electronic components, and so the focus here is on the transferability of structural integrity tests carried out at the large scale, to the real components on the small scale.

The effects of microstructure and will not be explored in this work, with material treated as a continuum, however the relevance of this work as still clear. One of the main objectives of this work is to investigate the feasibility of producing scaled models. The general motivation for this thesis is to be able to obtain information from a scaled down component that conveys information about the original size component.

This is essentially the reverse of what many of the authors listed here were doing, which was investigating the limitations of the classical strength theories when approaching microstructure length scales. Despite this being the other way round however, it is important to be aware of the limitations as they will still be applicable to the research carried out and described here.

The more general scaling research focused on scaling structural tests, and how the size can affect the results. Despite a large proportion of the research having been carried out on quasi-brittle materials, particularly concrete and in civil engineering contexts, the general scaling behaviours are directly applicable, with the work by Bažant showing how specimens at extreme sizes are likely to exhibit different behaviours.

The topic of producing scaled structural models, similar to those used in aeronautical and fluid dynamics research fields however, remains relatively unexplored, and will be addressed in this thesis, in particular any advantages, disadvantages and practical issues that may arise in the process.

Chapter 3

Simple scaling laws

This chapter looks at some simple scaling laws for stress fields, stress intensity factors and J-integrals. These concepts are fundamental when considering the structural integrity of a component or system, and they provide a good starting point for investigating the concept of scaling generally. These three factors are by no means exhaustive, however, and the initial approach taken which focuses on loads and displacement is also basic. This provides a foundation for a more complex formulation, addressing failure more generally, and which is addressed in more detail in Chapter 6.

3.1 The effect of scaling on stress fields

The effect of size on the relationship between applied loads and stress fields is relatively straightforward, provided one stays within a range that allows us to treat the material as a continuum and not have to factor in microstructure. If we consider a component subjected to a load or distortion, internally a strain and corresponding stress field develop, due to the redistribution of loads around the body. The redistribution will be dependent on the body's material properties, geometry, and the distribution of the load itself.

To start with, an elastic material is considered; plasticity will be considered later, however this builds upon (and is extension of) elastic theory, and so is subject to the same scaling laws. For an elastic material, Hooke's law applies, and as such, the stress state at any point can be described by the generalised stress tensor, $\sigma_{ij} = C_{ijkl}\varepsilon_{kl}$, where σ is the stress, ε the strain tensor, and C the stiffness matrix. For a three dimensional material this is given

by:

$$\begin{bmatrix} \sigma_{11} \\ \sigma_{22} \\ \sigma_{33} \\ \sigma_{23} \\ \sigma_{31} \\ \sigma_{12} \end{bmatrix} = \begin{bmatrix} C_{1111} & C_{1122} & C_{1133} & C_{1123} & C_{1131} & C_{1112} \\ C_{2211} & C_{2222} & C_{2233} & C_{2223} & C_{2231} & C_{2212} \\ C_{3311} & C_{3322} & C_{3333} & C_{3323} & C_{3331} & C_{3312} \\ C_{2311} & C_{2322} & C_{2333} & C_{2323} & C_{2331} & C_{2312} \\ C_{3111} & C_{3122} & C_{3133} & C_{3123} & C_{3131} & C_{3112} \\ C_{1211} & C_{1222} & C_{1233} & C_{1223} & C_{1231} & C_{1212} \end{bmatrix} \begin{bmatrix} \varepsilon_{11} \\ \varepsilon_{22} \\ \varepsilon_{33} \\ 2\varepsilon_{23} \\ 2\varepsilon_{31} \\ 2\varepsilon_{12} \end{bmatrix}, \tag{3.1}$$

where subscripts 1,2 and 3 refer to the principal stress and strain directions. When the problem being considered is in a state of plane stress or plane strain, this can be greatly simplified by setting the relevant parts of the stiffness matrix to 0.

The question considered here is how to produce the same stress field in a geometrically scaled model, i.e. one that has had all its dimensions scaled by λ. If we assume that the material properties of the component are independent of size, then it follows that the stress field of a component should remain the same provided the internal strains also remain the same. We know that strains are dimensionless and are simply a relative change in length, and so in order to obtain the same strain field in the scaled model, the deformations must also be scaled by λ. The applied stresses in this case then remain the same, and as a stress is simply a force over an area we need to change the load proportionally to take into account this change in area. Scaling dimensions by a factor of λ will produce a scaling of area by λ^2. The applied load must therefore also be scaled by λ^2, such that:

$$P_{\mathrm{m}} = \lambda^2 P_{\mathrm{p}}, \tag{3.2}$$

where P is the applied load, and the subscripts m and p refer to the full size prototype and scaled model respectively. Provided the material properties of the different sized specimens remain the same then this law holds true regardless of whether plasticity develops or not. Some examples demonstrating this scaling law follow.

3.1.1 Shrink fits and residual stresses

A relatively well understood method of generating a known stress field is via the use of shrink fits, and so this was chosen as the initial case study due to both its simplicity and relevance. A shrink fit, also known as an interference fit, is an assembly method whereby the relative movement between two parts is prevented by radial pressure at their interfaces. This interface pressure is created through interference between the inner diameter of the outer component, and the outer diameter of the inner component. This assembly typically involves the expansion of the outer component and/or the contraction of the inner component, through respective heating and/or

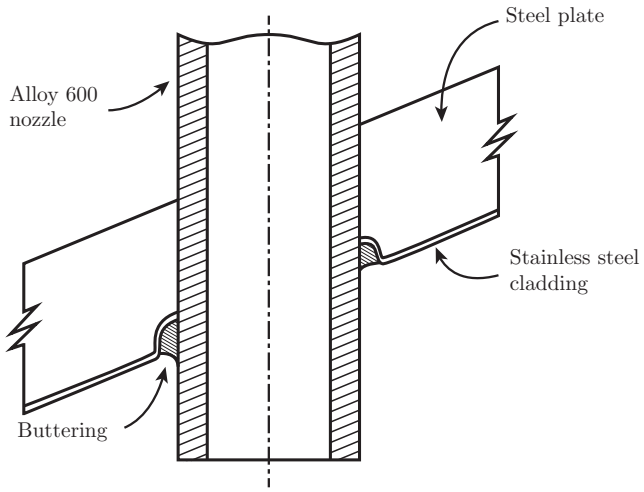

Figure 3.1: Diagram showing features of a typical CRDM nozzle and weld

cooling, so that on their return to the operating temperature, the interference and pressure are created (Truman and Booker, 2007).

The nuclear power industry utilised components that are often welded together and subjected to extreme operating conditions, where potential failures are an obvious cause of concern. One such component is the assembly where the control rod drive mechanism (CRDM) nozzles join the pressure vessel head (see Fig. 3.1), and which is typically shrink fitted together before being welded. The example that follows is simpler than this welded component but will share some of the basic features, and thus allow us to explore the scaling laws.

The equations governing shrink fits can be described using Lamé's solutions for the stresses in thick walled cylinders (Timoshenko, 1956), given below in Eqs. (3.3) to (3.5),

$$p = \frac{\delta}{R}\left[\frac{1}{E_\mathrm{o}}\left(\frac{b^2+R^2}{b^2-R^2}+\nu_\mathrm{o}\right)+\frac{1}{E_\mathrm{i}}\left(\frac{R^2+a^2}{R^2-a^2}-\nu_\mathrm{i}\right)\right]^{-1}, \tag{3.3}$$

$$\text{Inner cylinder}\begin{cases}\sigma_{rr} = \dfrac{R^2p}{r^2}\left(\dfrac{a^2-r^2}{R^2-a^2}\right) & \text{(3.4a)}\\ \sigma_{\theta\theta} = -\dfrac{R^2p}{r^2}\left(\dfrac{a^2+r^2}{R^2-a^2}\right), & \text{(3.4b)}\end{cases}$$

$$\text{Outer cylinder}\begin{cases}\sigma_{rr} = \dfrac{R^2p}{r^2}\left(\dfrac{r^2-b^2}{b^2-R^2}\right) & \text{(3.5a)}\\ \sigma_{\theta\theta} = \dfrac{R^2p}{r^2}\left(\dfrac{r^2+b^2}{b^2-R^2}\right), & \text{(3.5b)}\end{cases}$$

where p is the interface pressure, E is the Young's modulus, ν is the Poisson's ratio and σ_{rr} and $\sigma_{\theta\theta}$ are the radial and hoop stresses respectively.

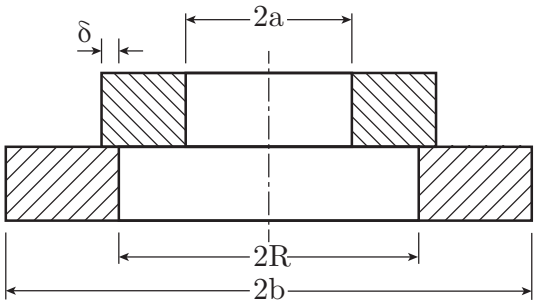

Figure 3.2: Schematic of shrink fit prior to assembly, showing notation

As shown in Fig. 3.2, a and b denote the inner and outer radii of the shrink fit respectively, R the interface position, δ the interference between the two cylinders and r the radial distance from the centre. Subscripts i and o refer to the inner and outer cylinders. As is often the case in the literature when dealing with shrink fits, for simplicity there will be no mention of length, as a state of plane stress is assumed. This assumption is not always valid, as there are documented edge effects that can affect the stress distribution at the edge of shrink fits (Pedersen, 2006), however these are much harder to solve analytically, and for the purposes of this example the plane stress assumption is perfectly acceptable. An analysis of scaling the shrink fit dimensions and the effect on the stress field follows.

Geometric scaling

Equations (3.3) to (3.5) were implemented in a Python program able to calculate the stress distribution and interface pressure throughout the shrink fit whilst varying the dimensions and material properties so as to be able to investigate the effects of scaling dimensions. The material properties and shrink fit dimensions in Tables 3.1 and 3.2 were used; both were arbitrarily chosen as representative values of a component that might be fabricated, using approximate material properties for a generic steel.

An additional scalable finite element model was produced using the same material properties and dimensions. The models used 1200 quad elements and axisymmetric boundary conditions. The stress distributions from the analytical and finite element simulations unsurprisingly showed very good agreement given the simplicity of the models. The results from the different sizes all returned identical stress distributions and stress magnitudes, when normalised against the inner and outer faces, i.e. across the entire thickness of the specimen, and so allowing for the stress fields to be directly compared. These results are shown in Fig. 3.3, displaying the hoop and radial stresses against the normalised distance from the inner to outer surface. As the horizontal axis has been normalised these results apply to both scales.

	E (GPa)	ν
Inner and outer rings	200	0.3

Table 3.1: Material properties used in the shrink fit models

	a	b	R	δ
Initial	20	30	25	0.025
Scaled	10	15	12.5	0.0125

Table 3.2: Dimensions (in mm) used in shrink fit models

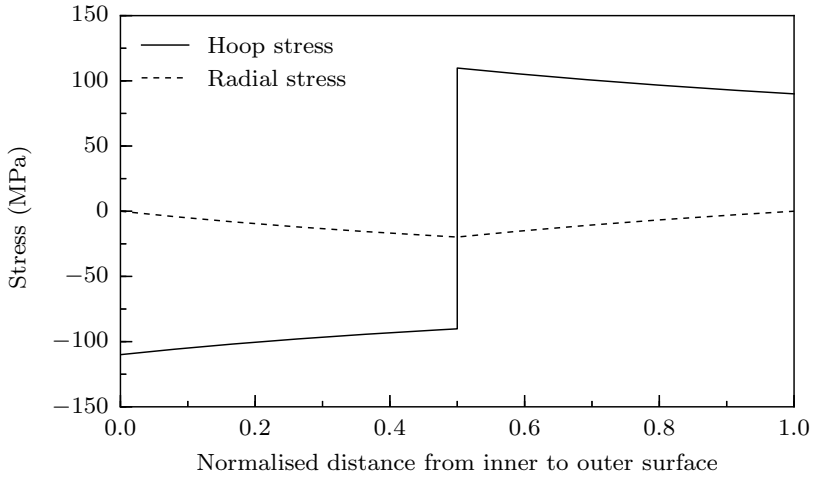

Figure 3.3: Stress profile in shrink fit

Examining Eq. (3.3) it can be seen that variables relating to dimensions cancel each other out, as shown below:

$$p = \frac{\lambda\delta}{\lambda R}\left[\frac{1}{E_\mathrm{o}}\left(\frac{\lambda\left(b^2+R^2\right)}{\lambda\left(b^2-R^2\right)}+\nu_\mathrm{o}\right)+\frac{1}{E_\mathrm{i}}\left(\frac{\lambda\left(R^2+a^2\right)}{\lambda\left(R^2-a^2\right)}-\nu_\mathrm{i}\right)\right]^{-1}, \tag{3.6}$$

As such, if all dimensions are uniformly scaled (including the interference) the resultant interface pressures will remain the same. The same applies to Eqs. (3.4) to (3.5), as shown in Eq. (3.6), and so as a result the normalised stress distribution shown in Fig. 3.3 applies to scaled models.

Non-geometric scaling

Non-geometric scaling, i.e. where not all dimensions are scaled by the same scale factor, was then considered, with the rationale being that when physically producing a scaled model limits may be imposed, such as a minimum possible interference due to machining constraints and tolerances, minimum inner radii so as to be compatible with other components, in order to adhere to weight limits, etc.

For the reasons described above explaining why uniform scaling produces the same stress distribution in different sized models, the same is therefore not true for models scaled non-uniformly. The ratios of dimensions in Eqs. (3.3) to (3.5) mean that a non uniform change will result in an altered combination of interface pressure and distribution and magnitude of stresses. In these cases it may be that some aspects of the model are more important than others, for example maintaining the same interface pressure in a scaled down model despite there being lower limit on the size of the interference.

The following example demonstrates the effects on the stresses of attempting to produce a half sized model which produces the same interference pressure, whilst capping the interference δ at a minimum value of 0.02 mm. In order to approximate a half model the position of the interface, R, has been scaled by 0.5, leaving a and b as the variables to be solved for. Equation (3.3) can be simplified for the case where the material properties of the inner and outer cylinders are the same:

$$p = \frac{E\delta}{R}\left[\frac{\left(b^2-R^2\right)\left(R^2-a^2\right)}{2R^2\left(b^2-a^2\right)}\right], \tag{3.7}$$

which can then be solved for a and b if attempting to match the interface pressures, assuming the same material properties as in the Table 3.2. The original unscaled shrink fit created an interface pressure of 19.8 MPa; by substituting this into Eq. (3.7) the solutions for a and b could then be found. A selection of these values that produce the same interface pressure, along with the remaining the dimensions, are shown in Table 3.3.

	a	b	R	δ
Unscaled	20	30.0	25.0	0.025
$a/b = 0.60$	8	13.44	12.5	0.020
$a/b = 0.73$	10	13.63	12.5	0.020
$a/b = 0.78$	11	14.11	12.5	0.020

Table 3.3: Dimensions (in mm) used in scaled shrink fit models

The stress distributions that were produced as a result of these scaled dimensions are displayed in Figs. 3.4a and 3.4b, normalised against through wall thickness. Clearly the radial stress distributions are quite similar due to the interface pressures having been maintained (which is equal to radial stress at the interface). The hoop stresses however show very different distributions, particularly the magnitudes of the peak stresses in the outer cylinders. One could argue that by scaling dimensions by different scale factors you are no longer dealing with scaling, but rather a different geometry, and this example shows the difficulties that can arise when dealing with non-geometric scaling. The nature of implementing scaled models in a practical scenario, means that there will often be constraints imposed where non-geometric scaling is ultimately required, however uniform scaling serves as a useful method for investigating this further.

3.1.2 Suspended beam under its own weight

Finally, a simple example showing how consideration is needed when scaling even basic models is examined. The example consists of a bar suspended under its own weight, as shown in Fig. 3.5 where L is the length of the bar and A the cross sectional area. The material properties for the bar are denoted by, E, for Young's modulus, and ρ for density. The weight of the unscaled bar, W_U, is therefore given by:

$$W_U = \rho A L g, \tag{3.8}$$

where g is gravitational acceleration. If the bar is then scaled geometrically by λ, then the cross sectional A area will scale by λ^2. Combined with the L being scaled by λ, this results in a volume increase by a scale factor of λ^3, and so the weight of the scaled bar, W_S, is also scaled by λ^3:

$$W_S = \rho \left(A\lambda^2 \right) (L\lambda)\, g \tag{3.9}$$

We have already seen that in order to produce the same stress field in a scaled model the applied load only has to be scaled by λ^2, so the resultant stress field in this case will be different simply from hanging under its own

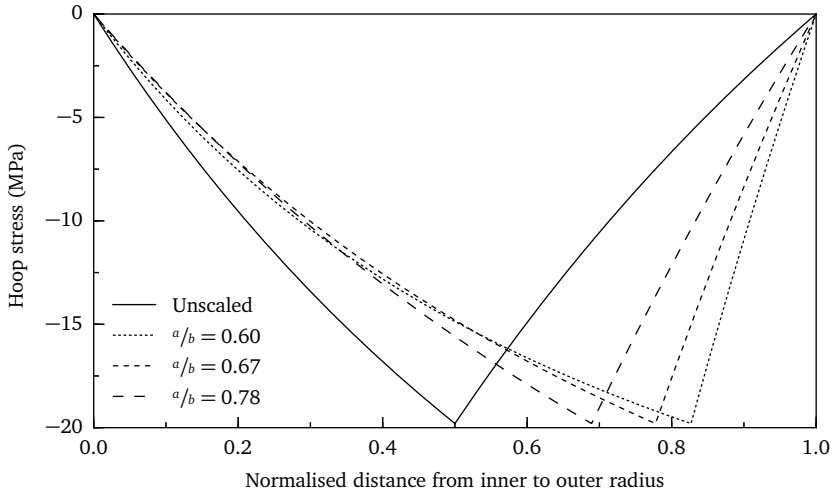

(a) Resultant radial stresses when dimensions scaled so as to maintain interface pressure

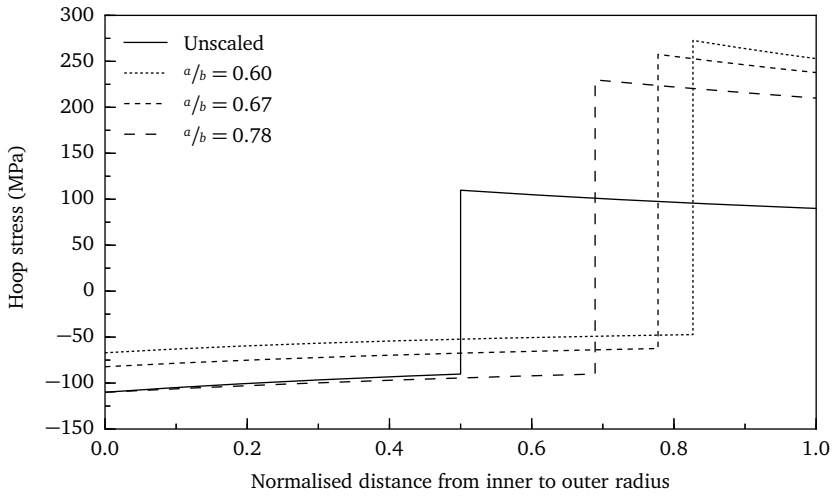

(b) Resultant hoop stresses when dimensions scaled so as to maintain interface pressure

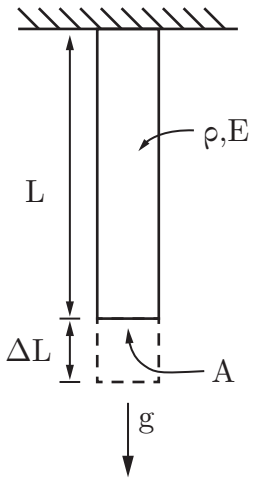

Figure 3.5: Schematic of suspended beam under its own weight

weight. The change in length of the unscaled bar, in this case denoted by ΔL_U, is given by

$$\Delta L_U = \frac{\rho A L^2 g}{2EA}. \tag{3.10}$$

The change in length of the scaled bar is then given by:

$$\Delta L_S = \frac{\rho \left(A\lambda^2\right) \left(L\lambda\right)^2 g}{2E \left(A\lambda^2\right)}, \tag{3.11}$$

the result of which is that the relative change in length, i.e. the strain, will be different to that of its unscaled counterpart due to the additional λ^2 factor that has been introduced. This example has only considered the elastic regime for simplicity of analysis, however these differences are directly applicable to the plastic regime; for components with sufficiently large or small scale factors this could result in failure at one size and structural stability at another with no additional applied loading or stress. It may be the case that this effect is unimportant if the applied loads or residual stresses are large enough that this scaling incompatibility is wiped out. However, for large or heavy components this will certainly have to be considered; this effect demonstrates some one of the compromises that may have to be made even when dealing with very simple components.

3.2 The effect of scaling on stress intensity factors

The next area of interest was that of the stress intensity factor, K_I, a key parameter used when considering brittle fracture and which describes the stresses immediately ahead of the crack tip. Again, the effect that scaling

plays on the stress intensity factor is straightforward to analyse. The generalised equation for the stress intensity factor for a crack undergoing small scale yielding, as described in Chapter 2, is given by:

$$K_{\mathrm{I}} = \sigma\sqrt{a_{\mathrm{eff}}}Y, \tag{3.12}$$

where a_{eff} is the effective crack length, and Y is a geometry factor taking into account the shape of the component and how it is loaded.

This geometry factor is dimensionless containing only ratios of dimensions. The stress term, σ, refers to the applied stress, which as we have seen is maintained simply by scaling the applied load by a factor of λ^2. The only remaining dimension in Eq. (3.12) is therefore the crack length term, $\sqrt{a}$, and so introduces a $\sqrt{\lambda}$. By introducing the scale factors in the load and the crack length terms and combining them, the equation can then be rearranged to give the relationship necessary for the same K_{I} in the full size and scaled models:

$$P_{\mathrm{m}} = \lambda^{1.5}P_{\mathrm{p}} \tag{3.13}$$

An alternative approach is to consider the effect of scaling the load so as to introduce the same stress field, i.e. keeping σ unchanged by scaling P_m by λ^2. The result would be:

$$K_{\mathrm{I\,m}} = K_{\mathrm{I\,p}}\lambda^{0.5}. \tag{3.14}$$

Some examples follow demonstrating this scaling law.

3.2.1 Centre cracked plate

This first small case study consists of the well documented example of a centre cracked plate under uniaxial tension, shown in Fig. 3.6, where $2a$ and $2b$ represent the crack and plate widths respectively. The generic expression for stress intensity factor given by Eq. (3.12) is still applicable here, and the geometry function, Y, is in this case a function of the ratio of crack length to plate width. Work by Tada et al. (2000) showed that in this case $f(a/b)$ could be approximated by Eq. (3.15), as follows:

$$f\left(a/b\right) = \left\{1 - 0.025\left(a/b\right)^2 + 0.06\left(a/b\right)^4\right\}\sqrt{\sec\left(\frac{\pi a}{2b}\right)}. \tag{3.15}$$

It should be noted that Eq. (3.15) is a function of a/b, and as such geometric scaling produces no change in its value due to the ratio being maintained. The only remaining dimension is the crack length, a, in Eq. (3.12), and therefore it can be deduced that uniform scaling of dimensions by λ whilst maintaining the same applied stress would result in a scaling of K_{I} by $\sqrt{\lambda}$. Alternatively one could say that to maintain the same stress intensity factor in a uniformly scaled model, the applied load would have to be

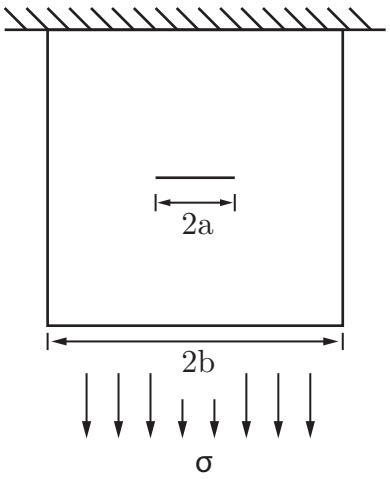

Figure 3.6: Diagram of centre cracked plate

scaled by $\lambda^{1.5}$. The function given in Eq. (3.15), $f\left(a/b\right)$, is specific to the case of the centre cracked plate under uniaxial far field loading, however it is always a dimensionless quantity defined as a function of crack size to characteristic length ratio (Broek, 1986), and therefore this scaling law will hold regardless of the specifics involved.

In the case of non-uniform scaling however, i.e. when the dimensions are scaled by different scale factors, it becomes clear that the solutions are very much dependent on geometry. This can be demonstrated using the previous example of the uniaxially loaded plate and specifying arbitrary dimensions. Equations (3.12) and (3.15) were used to calculate the necessary parameters for the scaled model to have the same K_{I} value as the original prototype, with $2b$ scaled by an arbitrary constant value of 4 for ease of plotting. The results are displayed in Fig. 3.7.

3.2.2 Circumferentially cracked pipe

The case of the centre crack in a plate is important as it is a very well understood example, however its applicability to real life scenarios is limited. A more relevant example is that of a circumferential crack in a uniaxially loaded pipe, which whilst still simplified bears more of a resemblance to a real component such as the CRDM nozzle described in Section 3.1.1. This solution to this example utilises a polar different coordinate system.

The stress intensity factor calculation for a circumferential crack in a pipe is similar to that of a cracked plate, albeit with a transformation of the coordinate system. A solution for K_{I} with a geometry factor derived by Takahashi (2002) is given by Eq. (3.16)

$$K_I = \sigma\sqrt{\pi R_{\mathrm{m}}\theta}F, \tag{3.16}$$

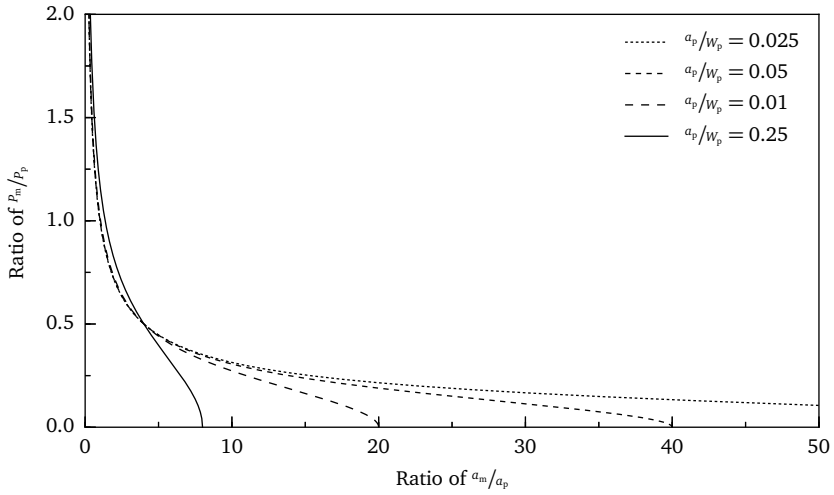

Figure 3.7: Required scale factors to obtain same value of K_I

$$F = \left[A + B\left(\frac{\theta}{\pi}\right) + C\left(\frac{\theta}{\pi}\right)^2 + D\left(\frac{\theta}{\pi}\right)^3 + E\left(\frac{\theta}{\pi}\right)^4 \right]$$
$$A = 1$$
$$B = -1.040 - 3.1831\xi - 4.83\xi^2 - 2.369\xi^3$$
$$C = 16.71 + 23.10\xi + 50.82\xi^2 + 18.02\xi^3$$
$$D = -25.85 - 12.05\xi - 87.24\xi^2 - 30.39\xi^3$$
$$E = 24.70 - 54.18\xi + 18.09\xi^2 + 6.745\xi^3$$
$$\xi = \log\left(\frac{t}{R_m}\right)$$

where R_m is the mean radius of the pipe, t is the thickness and θ is the half angle of the crack (as shown in Fig. 3.8). In this case $R_m\theta$ is equivalent to the crack length.

Similarly to the case of the centre cracked plate the geometry factor F is again a function of ratios of key dimensions, and as such when uniformly scaled will remain unchanged. As was mentioned previously, the geometry factors always contains ratios of characteristic dimensions and so will be unchanged by uniform scaling. This time the only remaining scaled dimension in Eq. (3.16) is R_m (θ does not scale, as angles are independent of length in this coordinate system), and so the same $\sqrt{\lambda}$ law applies.

3.3 J-integral scaling

Finally, the effect of scaling on the J-integral is examined. This has already been described in Chapter 2, and is an important parameter in structural

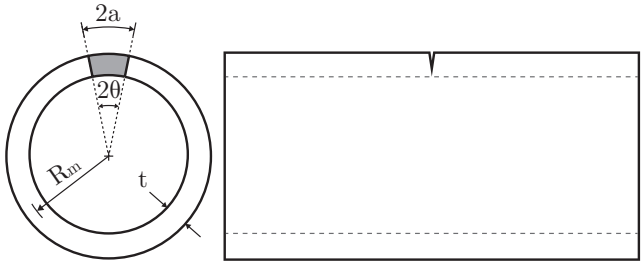

Figure 3.8: Diagram of circumferentially cracked pipe

integrity, describing the energy release rate during fracture. Its derivation is the most complex of the three parameters considered so far, and consequently the effect of scaling on the J-integral is also more complex.

To summarise the introduction to the J-integral from Chapter 2, J can be expressed as:

$$J = \int_{\Gamma} \left(W \, dy - \hat{T} \frac{\partial \hat{u}}{\partial x} \, ds \right), \tag{3.17}$$

for a body containing a two dimensional strain field, where Γ describes a contour completely enclosing the crack tip, W is the strain energy density, $\hat{T}$ is the traction vector and s is the distance across the contour Γ. The strain energy density, W, is a function of the stresses and strains in the body,

$$W = \frac{1}{2} \sigma_{ij} \varepsilon_{ij}. \tag{3.18}$$

If we consider the case of a scaled model which has also had its applied load scaled so as to maintain the same stress field (and corresponding strain field), we can see from the definition of the strain energy in Eq. (3.18) that it will remain constant with scaling. The total strain energy of the body is a function of the strain energy density and the volume, and so the strain energy of the specimen will scale with the volume, i.e. by λ^3. The traction vector, $\hat{T}$, can be rewritten as a function of stresses, $\hat{T} = \sigma_{ij} n_j$, where n_j is the normal vector along Γ (Bower, 2009). Again, if the load has been scaled accordingly so the stress field remains the same then σ_{ij} will remain unchanged, and consequently the traction vector will remain the same. Finally the partial derivative of the displacement vector $\hat{u}$ with respect to x; if the stress and strain fields remain the same in the scaled model then the displacements will have scaled by λ, meaning that the displacement gradient which this effectively describes will also stay unchanged. The result is that the function to be integrated is unaffected by scale, resulting in the scale factor only being introduced upon integration. Consequently, the resultant J-integral value for a scaled model will also be scaled by λ. Some simple case studies of this using Rice's original examples follow.

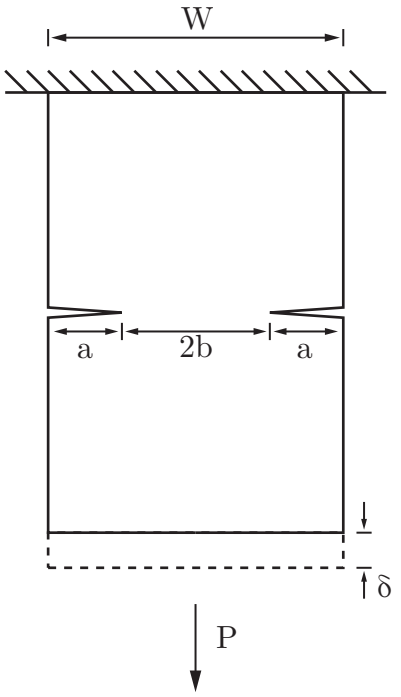

Figure 3.9: Double edge notched plate subject to tensions

3.3.1 Simple examples

Double edge notched plate in tension

This example described by Rice et al. (1973) utilises a plate of width W containing two coplanar edge cracks of length a and an uncracked ligament of length b, such that $2a + b = W$, as shown in Fig. 3.9, loaded by P per unit of thickness. It was assumed that the cracks are of sufficient size that any plasticity is confined to the uncracked ligament, b. For the evaluation of J Rice et al. used an alternate form which allowed them to relate J to the rate of change of the load against displacement curves, with respect to crack length, a, as opposed to time, and whereby

$$J = \int_0^{\delta} \left(-\frac{\partial P}{\partial a} \right) d\delta, \text{ or } J = \int_0^{P} \left(\frac{\partial \delta}{\partial a} \right) dP, \tag{3.19}$$

where δ is the displacement at point of applied load. This displacement is assumed to be the summation of elastic and plastic displacement, so that

$$\delta_{\text{total}} = \delta_{\text{elastic}} + \delta_{\text{plastic}}. \tag{3.20}$$

Rice et al showed using dimensional analysis that δ_{plastic} must be a function of material properties (which do not change with scale), the area over which the load acts (P/b) and a characteristic dimension, b, so that

$$\delta_{\text{plastic}} = bf\left(\frac{P}{b}\right). \tag{3.21}$$

This fits with the earlier analysis where it was demonstrated that a scaled model with scaled load will undergo deformation also scaled by λ. The analysis of J then takes the form:

$$J = J_{\text{elastic}} + \int_0^P \left(-\frac{\partial \delta_{\text{plastic}}}{\delta b} \right) dP. \tag{3.22}$$

The partial differential of Eq. (3.21) is equal to:

$$-\frac{\partial \delta_{\text{plastic}}}{\partial b} = \frac{P}{b} f' \left(\frac{P}{b} \right) - f \left(\frac{P}{b} \right), \tag{3.23}$$

which can then be substituted into Eq. (3.22) and integrated by parts to give:

$$J = J_{\text{elastic}} + \frac{1}{b} \left[2 \int_0^{\delta_{\text{plastic}}} P \, d\delta_{\text{plastic}} - P\delta_{\text{plastic}} \right]. \tag{3.24}$$

It should be noted that J_{elastic} is equal to the energy release rate and is therefore proportional to K_{I}^2. The right hand side of the equation describes the area under part of the load-displacement curve (noting that in this case the load is per unit of thickness), and consequently if the load is scaled by λ^2, so as to produce the same stress and displacement field, the result of the integral will be scaled by λ^2. Combining this result with J_{elastic} and remembering Eq. (3.14), it becomes clear that the resultant J integral value for a λ^2 scaled load will be scaled by λ.

In order to both verify and further demonstrate this two finite element models of the double edge notched plate were created. A scale factor of $\lambda = 0.5$ was used, with the resultant dimensions and material properties listed in Table 3.4. To save computation time, only the left side of the plates were modelled with a symmetrical boundary condition applied. The plates were modelled as two dimensional to further save computation time. A total of 7066 quadrilateral elements were used in each, with a focused mesh around the crack tips featuring collapsed node elements. The mesh layout is shown in Fig. 3.10. The force was applied as a force per unit length along the bottom surface; the models simulated this being ramped linearly from $0\,\text{N}\,\text{m}^{-1}$ to $100\,\text{MN}\,\text{m}^{-1}$, at which point the simulation ended.

	a (mm)	b (mm)	P (N/m)	E (GPa)	ν
Initial	200	300	100	200	0.3
Scaled	100	150	100	200	0.3

Table 3.4: Dimensions and material properties used in notched plate Abaqus model

Looking at Fig. 3.11a it is clear that the stress fields in both size plates are identical. Likewise, the strain energy densities shown in Fig. 3.11b, as

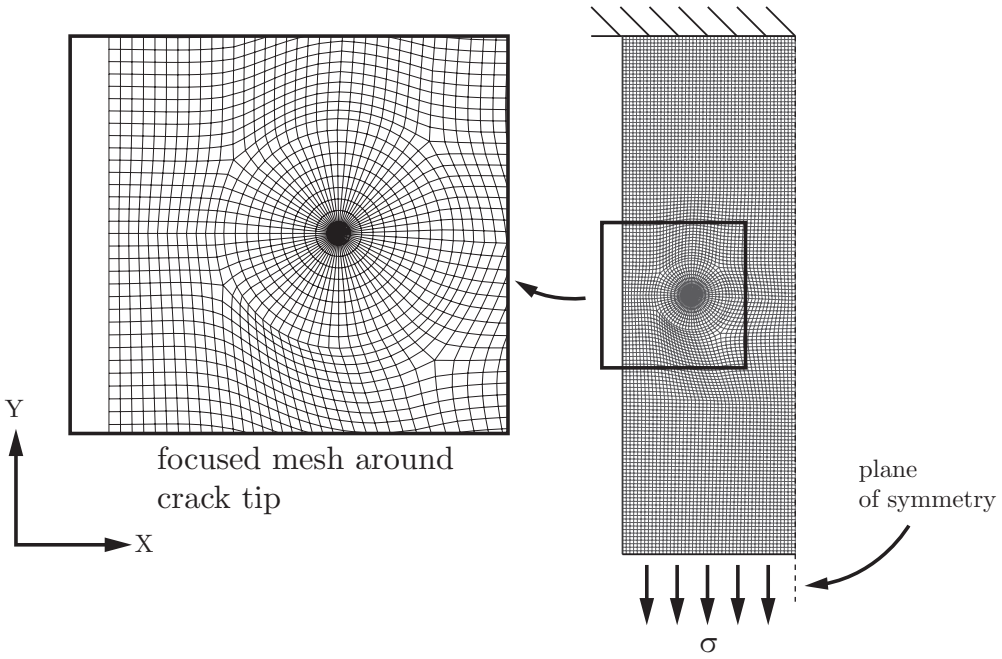

Figure 3.10: Schematic and mesh of double edge notch Abaqus model

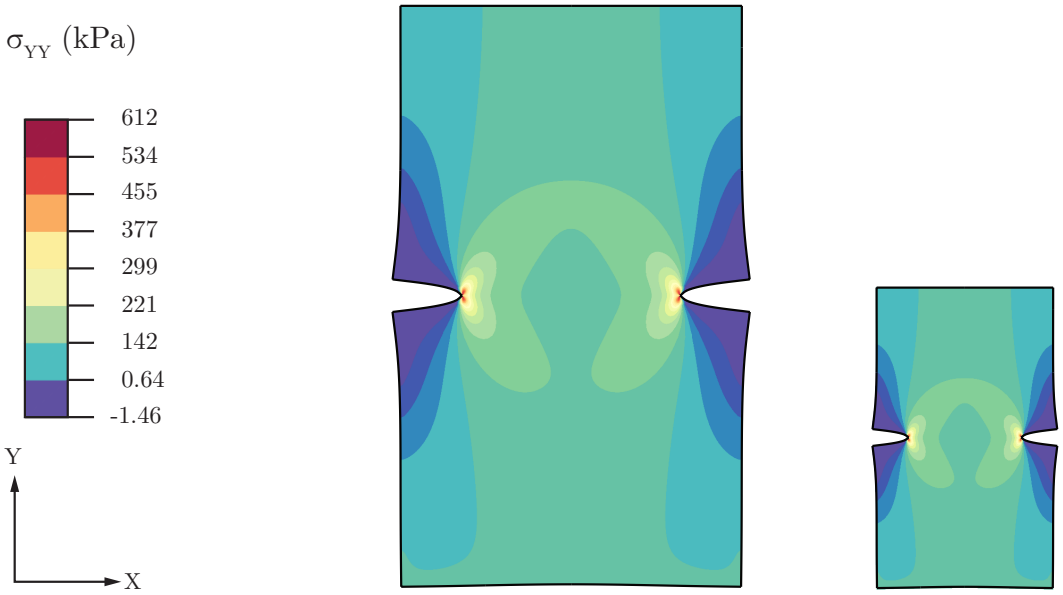

(a) Stresses in the two plates after loading

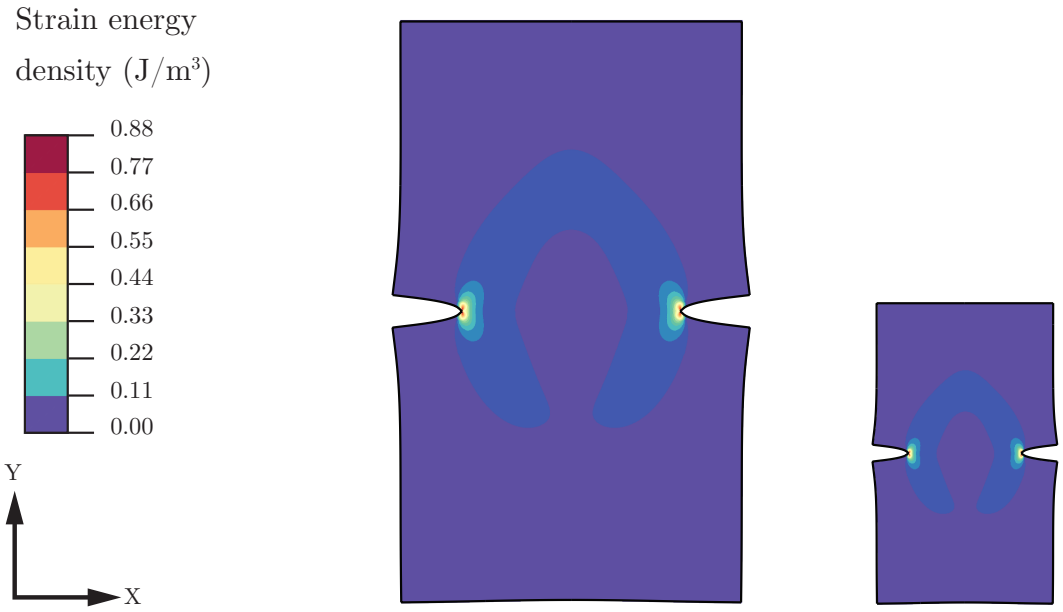

(b) Elastic strain energy densities in the plates after loading

Figure 3.11: Finite element results for stresses and strain energy densities in scaled double edge-notched plates

discussed previously, also remain the same. Finally, Fig. 3.12 shows the J-integral values calculated by Abaqus as the load is applied. It is clear from this that the above scaling law holds and that the smaller plate's J values

correspond to half those of the larger, i.e. scaled by λ.

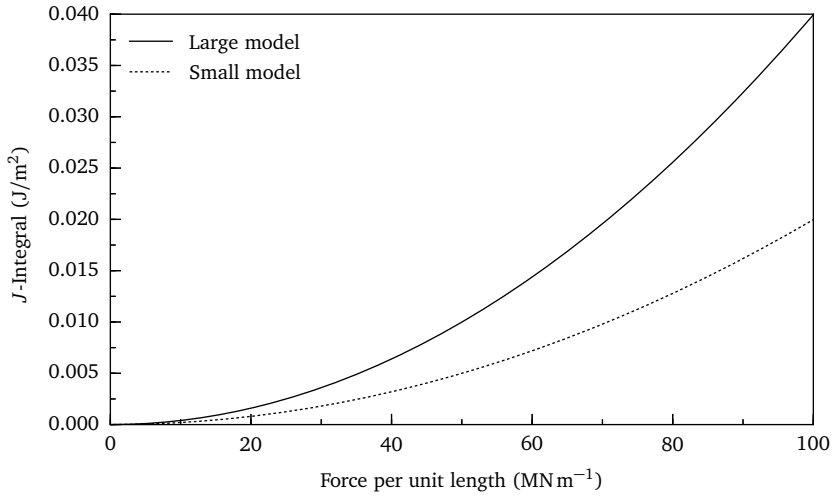

Figure 3.12: Elastic J-integral for both plates as load increases

3.4 Discussion

This chapter has looked at the way in which three important structural integrity concepts are affected by the scaling of dimensions.

When considering each of them independently, the stress intensity factor K_I is arguably the most straightforward to account for. Being an elastic parameter and linearly proportional to load, it is simple to calculate what effect maintaining the applied load will have on K_I, as well as how to scale the load to obtain the same K_I value at different scales.

The effects of scaling on stresses are also relatively straightforward. If the aim is to obtain the same stress field distribution and magnitudes at different scales, be they elastic or elastic-plastic, then as described by Eq. (3.2), the load simply has to be scaled by λ^2, i.e. the same applied stress must be maintained. The effect on the stress field of not scaling the load however is harder to predict. The evolution of the stress fields with increasing load, particularly in the case of non-linear materials, can be complex, and while analytical models may exist for some geometries the majority will require modelling or measurements to predict their behaviour.

The scaling of the J-integral, which as a parameter takes into account both fracture and plasticity, has its own scaling law. For an elastic material or when operating in the elastic regime, its value is proportional to that of K_I^2, and consequently the effect on it of scaling while maintaining the same stress field is simple to predict. Similarly, for an elastic material it is straightforward to scale the load so as to obtain the same J value in both.

This also holds true for an elastic-plastic material, provided that the plastic zone is small compared to the sample dimensions (i.e. small scale yielding). Once material non-linearities have to be considered however this becomes harder to predict. If the loads are scaled appropriately such that the same stress fields develop, even in the plastic regime, then the J values scale with λ. However unlike with K_{I} they do not increase linearly with load, but rather are very dependent on the developing stress fields. This introduces an incompatability between scaling so as to maintain elastic J, and scaling so as to maintain plastic J, which further adds to the complication of scaling with the intent of maintaining paramters of interest.

These three parameters are used in the analysis of structural integrity and are vital to the understanding of different types of failure. The differences in the way in which they all scale demonstrates how their combined effects on failure may be difficult to predict. This is further examined in the remaining chapters.

A limitation to the approach considered here has been in the choice of load. While statically applied loads will be those of most concern in enough cases as to warrant consideration, there will be many others in which dynamic loads are equally, if not more, important. The effects of scaling in these scenarios has not been considered here, however they are examined in more detail in Chapter 6.

3.5 Summary

This chapter has introduced the idea of scaling laws, focusing on three parameters that are essentially when evaluating the structural integrity of a component, and key concepts in the solid mechanics community. The scaling laws themselves described how to scale applied loads so as to maintain each of the parameters in question. No attempt was made to discuss their potential interaction, and this will be discussed in more detail in Chapter 6.

The scaling laws themselves were:

- In order to obtain the same stress fields in scaled components, the loads must be scaled according to: $P_{\mathrm{m}} = \lambda^2 P_{\mathrm{p}}$.
- In order to obtain the same stress intensity factors in scaled components, the applied loads must be scaled according to: $P_{\mathrm{m}} = \lambda^{1.5} P_{\mathrm{p}}$. This assumes that the scale factor is such that small scale yielding conditions are maintained, which will not necessarily hold true at small scale factors. At small scale factors, global yielding may change the nature of the failure mechanism.
- In scaled models where the load has been scaled to as to maintain the same stress fields, i.e. where the load has been scaled by λ^2, the J values will be scaled by λ.

Non uniform scaling was also touched upon, and will also be discussed in further detail in Chapter 6.

Chapter 4

Design of experiments

4.1 Introduction

Building on the work from Chapter 3, experimental validation for the scaling of stress fields and stress intensity factors is now considered. This chapter focuses on the design of both the specimens and the experimental method, with the results then discussed in the following chapter. Work on the scaling of the J-integral is discussed in Chapter 6.

The experiments consisted of a series of fracture tests on notched beams, followed by plastically deforming scaled beams using four point bending, which were then measured using neutron diffraction. These were chosen to validate the scaling laws described in Chapter 3, as well as to highlight any issues that might arise in the process. Neutron diffraction is discussed in more detail in Section 4.4.3, and it was specifically chosen over other strain relief based methods of measuring residual stress, as it has the ability to measure stresses inside components of varying sizes, producing high resolution measurements for all three components of stress.

4.2 Material characterisation

The decision was made to use the same material for both sets of experiments (the fracture based experiments, and the residual stress based experiments), so as to ensure that comparisons and observations made could be compared without having to account for differences in material properties. A 7000 series aluminium alloy - 7449, was selected as it had the advantage of having a low toughness at room temperature, therefore simplifying the fracture experiments, and being readily available in sufficient quantities to perform multiple tests. This material had previously been used as part of a collaborative project known as COMPACT, which had looked at residual stresses in forgings made from this 7449 alloy Robinson et al. (2010). The material had been supplied by Alcan, Issoire, France, as a cast slab, however any sub-

Table 4.1: Composition by weight for Al-7449 (%) (Aluminum Association, 2000)

Al	Cu	Fe	Mg	Mn	Si	Zn	Zr+Ti	Other
85.6 - 89.3	1.4 - 2.1	0.15	1.8 - 2.7	0.2	0.12	7.5 - 8.7	0.25	0.15

sequent heat treatment it may have been subjected to post casting was not known. The composition specifications of the material are listed in Table 4.1 (Aluminum Association, 2000).

In order to design the experiments detailed in this chapter reliable finite element models were needed, which in turn demanded accurate material properties. The profile of a uniaxial tensile specimen was machined out of the aluminium plate using electrical discharge machining (EDM), with the extracted profile then "sliced" into individual specimens (see Fig. 4.1). This allowed for specimens to be extracted from a range of depths throughout the plate, highlighting any obvious material property variations that may have resulted from the casting process.

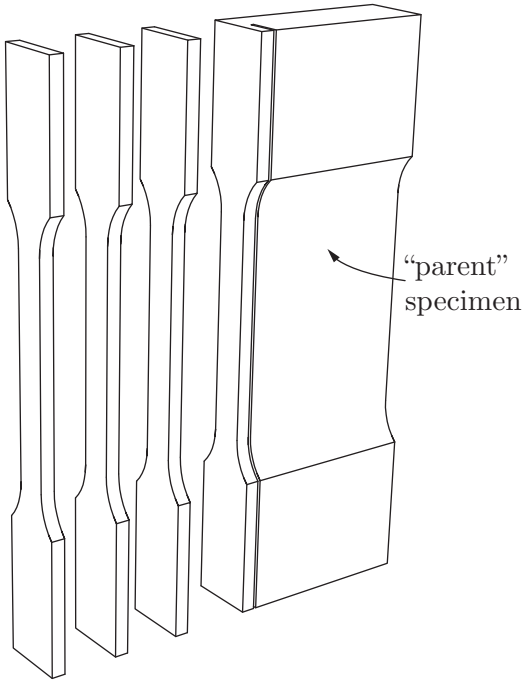

Figure 4.1: Schematic showing how tensile specimens were extracted from the plate

The specimens conformed to BSI 6892 (BS EN ISO 6892-1, 2016) and featured a rectangular cross section for use with a 50 mm clip gauge. The dimensions are shown in Fig. 4.2. The profiles of all the specimens were expected to be virtually identical due to having been sliced from the same

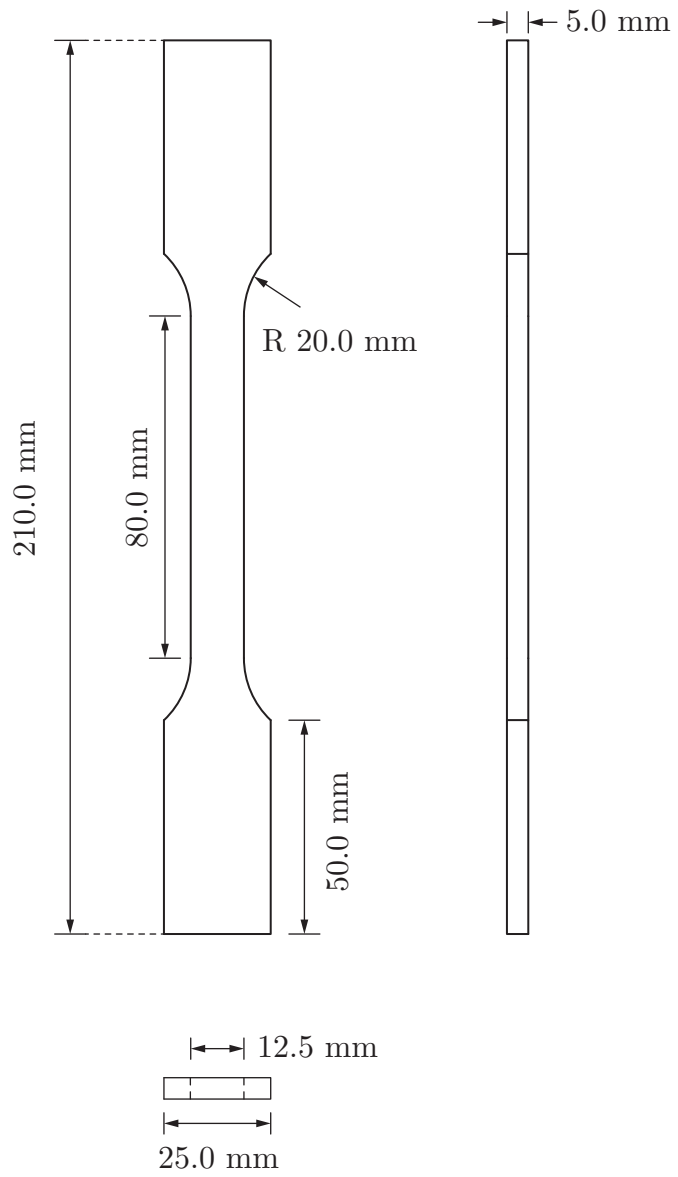

Figure 4.2: Schematic of tensile specimens, with all dimensions in mm

"parent" specimen, however EDM inherently produces some variability attributable to various parameters involved in the spark erosion process (Ho and Newman, 2003); it was important to characterise this to ensure that the subsequent material property calculations were based on the correct tensile specimen dimensions. The measured specimen dimensions are shown in Table 4.2 and were found to have a mean cross sectional area of 62.20 mm^2 (compared with the design value of 62.5 mm^2) with a standard deviation of 0.75 mm^2. The cross sectional area is important here, as it bears the load of the uniaxial tensile test.

The tensile tests were carried out using an Instron 1342 250 kN uniaxial fatigue machine, fitted with flat grips. The load output from the test rig

Table 4.2: Tensile specimen dimensions

Specimen no.		1	2	3	4	5	6	7	8	9
Width	mm	12.46	12.43	12.40	12.52	12.51	12.54	12.53	12.53	12.52
Height	mm	4.93	4.90	4.95	5.01	5.00	5.01	5.02	5.00	4.99
Area	mm^2	61.43	60.91	61.38	62.73	62.55	62.83	62.90	62.65	62.47

and the clip gauge were recorded throughout the tests using the Bluehill v2.9 software (Instron, 2017). An extension rate of $0.5\,\mathrm{mm\,min^{-1}}$ was used and the specimens were loaded until failure occurred. The data was then converted from load and extension to true stress and strain using Eqs. (4.1) and (4.2),

$$\varepsilon = \ln(e+1) \tag{4.1}$$

$$\sigma = \frac{P}{A_0}(e+1), \tag{4.2}$$

where

$$e+1 = \left(\frac{L}{L_0}\right),$$

and where ε is true strain, σ is true stress, P is applied load, L_0 is original length (i.e. the gauge length) and L is the measured deformed length (Dieter and Bacon, 1986).

A Python script was written to process the results, converting them from displacement and load to true stress and strain, then calculating the material properties. This script smoothed the data, calculated the gradients, and found the curve peaks, so as to enable the calculation of these material properties. This could of course have been done manually, however automating it allowed the process to be completed quickly for all nine specimens, and provided a ready to run script that could be used again, should more tensile tests be required at a later date. These produced a Young's modulus of 65.7 GPa, a 0.2% proof stress of 557 MPa and an ultimate tensile stress (UTS) of 567 MPa. This material data was then used to inform the subsequent models in this chapter.

4.3 Fracture of SENB specimens

4.3.1 Introduction

An experiment was then devised to verify the scaling law for stress intensity factors whilst also highlighting any experimental issues associated with scaling. In order to accomplish this, two sets of different size, but geometrically similar specimens, were to be produced which would be loaded until failure. If the aluminium proved to be relatively brittle, then it would fail when the stress intensity factor at the crack tip reached a critical value; namely the fracture toughness.

4.3.2 Specimen design

The specimens had to meet certain criteria:

- They size difference must be such that differences in failure loads between the two sizes must be clearly visible.
- The larger specimens must not be so big as to require an impractically large load. Likewise the smaller specimens must not require an impractically small load. These constraints would be dependent on the available test machines.
- Due to the inherent scatter associated with fracture tests, specimens must be simple enough to produce in sufficient quantities to produce fracture load distributions.

Based on these criteria, single edge notched bend (SENB) specimens were chosen for use in a four point bend rig configuration. SENB specimens would be simple enough to produce in sufficient quantities to produce a fracture distribution.

The equations governing the stress intensity factor for a SENB in a four point bend are given by Baratta and Fett (2000) as:

$$K_{\mathrm{I}} = \frac{P(S_{\mathrm{o}} - S_{\mathrm{i}})}{BW^{3/2}} f\left({}^{a}/_{W}\right), \tag{4.3}$$

where

$$\begin{aligned} f\left({}^{a}/_{W}\right) = \left[\frac{3\left({}^{a}/_{W}\right)^{1/2}}{2\left(1-{}^{a}/_{W}\right)^{3/2}}\right] \Bigg[& 1.9887 - 1.326\left({}^{a}/_{W}\right) \\ & - \Big\{3.49 - 0.68\left({}^{a}/_{W}\right) \\ & + 1.35\left({}^{a}/_{W}\right)^{2}\Big\}\left({}^{a}/_{W}\right)\frac{\left(1-{}^{a}/_{W}\right)}{\left(1+{}^{a}/_{W}\right)^{2}}\Bigg]. \end{aligned} \tag{4.4}$$

The crack length is denoted by a, the inner and outer pin spans by S_i and S_o respectively, the beam height by W and the beam thickness by b.

The schematic for the SENB bend configuration is shown in Fig. 4.3. The treatment of the material, and consequently its fracture toughness, were unknown, but research carried out on various heat treatments of the same alloy by Kamp et al. (2002) suggested that it would lie in the region of $25\,\mathrm{MPa}\sqrt{\mathrm{m}}$ to $45\,\mathrm{MPa}\sqrt{\mathrm{m}}$. By taking the upper bound value for fracture toughness and using it in conjunction with Eqs. (4.3) and (4.4), the dimensions in Fig. 4.3 were decided on for the specimens. The scale factor of $1/3$ was decided upon as it meant that failure loads of up to 5 kN and 47 kN could be expected for the small and large specimens respectively, allowing for the tests to be carried out on a 250 kN test machine.

A sensitivity analysis was carried out to ascertain the level of impact that each of the geometrical specimen parameters would have on the stress intensity factor, and so which factors needed to be most carefully controlled.

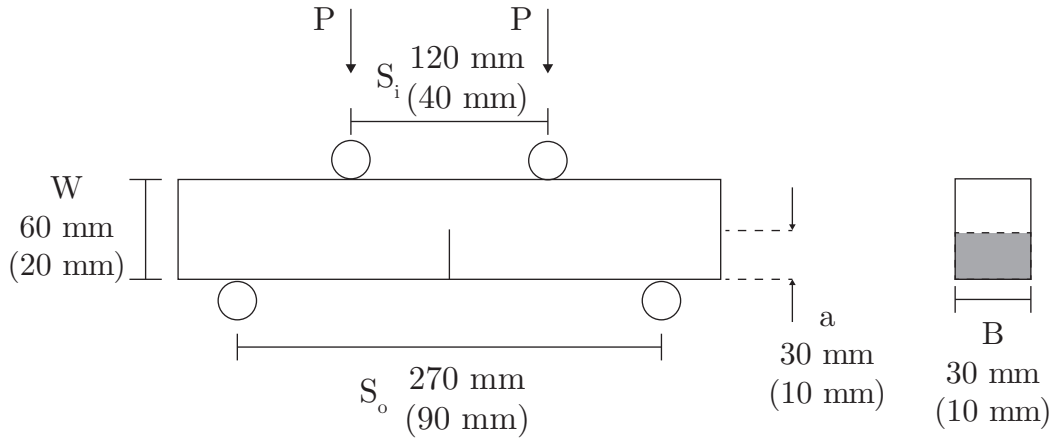

Figure 4.3: Schematic of SENB in four point bend configuration. Dimensions given for both specimens, with the smaller ones in brackets

A sensitivity analysis takes the expected variance for each of the parameters and assesses their contribution to the overall variance (Booker et al., 2001). For a function y containing multiple parameters, such that

$$y = \phi(x_1, x_2, \ldots, x_n), \tag{4.5}$$

the variance can be approximated using the first order partial derivatives:

$$\begin{aligned}\sigma_y &\approx \left(\sum_{i=1}^{n} \left(\frac{\partial y}{\partial x_i} \right)^2 \cdot \sigma_{x_i}^2 \right) \\ &= \left[\left(\frac{\partial y}{\partial x_1} \right)^2 \cdot \sigma_{x_1}^2 + \left(\frac{\partial y}{\partial x_2} \right)^2 \cdot \sigma_{x_2}^2 + \ldots + \left(\frac{\partial y}{\partial x_n} \right)^2 \cdot \sigma_{x_n}^2 \right].\end{aligned} \tag{4.6}$$

The partial derivatives can then be approximated using the finite difference method, so that

$$\left(\frac{\partial y}{\partial x_i} \right)_k \approx \frac{(y_{k+1} - y_{k-1})_i}{2\Delta x_i}, \tag{4.7}$$

where the subscripts $k+1$ and $k-1$ denote the evaluation of the function using upper and lower bounds respectively, spaced apart from y_k by Δx.

For this sensitivity analysis, Eqs. (4.3) and (4.4) were rearranged to make y a function of only the geometry, as these were the parameters that were of interest in controlling throughout the specimen manufacture, so that $y = K_I/P$. Process capability maps by Booker et al. (2001) for milling, which was to be used for machining the specimens down to their final shape after being cut from the main block, and EDM, which was to be used for creating the cracks, were used to estimate the tolerances (and therefore upper and lower bound values) for each of machined parameters, along with an estimated ± 1 mm variance in pin spans due to alignment errors. The partial derivatives

	a	B	W	S_i	S_o
x_{k-1}	29.95	29.81	59.74	119.00	269.00
x_k	30.00	30.00	60.00	120.00	270.00
x_{k+1}	30.05	30.19	60.26	121.00	271.00
Δx_i	0.05	0.19	0.26	1.00	1.00
y_{k-1}	2.95E-02	3.05E-02	3.07E-02	3.05E-02	3.01E-02
y_k	3.03E-02	3.03E-02	3.03E-02	3.03E-02	3.03E-02
y_{k+1}	3.11E-02	3.01E-02	2.99E-02	3.01E-02	3.05E-02
$\left(\frac{\partial y}{\partial x_i}\right)_k$	-1.54E-03	1.01E-03	1.53E-03	2.02E-04	2.02E-04
s^2	2.19E-09	9.34E-10	2.14E-09	3.74E-11	3.74E-11

Table 4.3: table showing upper and lower bound values and partial derivative approximations for large specimens $(\lambda = 1)$

were then approximated using Eq. (4.7). The upper and lower bounds and the approximated finite differences are given Tables 4.3 and 4.4, with the relative contributions to the overall variance shown in the pareto chart in Fig. 4.4.

It is clear from Fig. 4.4 that despite the tolerances not scaling with geometry, the relative contributions of each of the geometrical parameters remains virtually unchanged regardless of the size. The most important geometrical factors are the crack length and the beam height, with each of these contributing approximately 40% of total variance.

Given the importance of the beam height, this was to be manually measured for each specimen after having been milled. The decision was also made to keep the notches as purely EDM slits. Strictly following standards, fracture tests will typically use a sharp crack, introduced using "fatigue pre-cracking", to introduce a real crack ahead of the notch (Towers and Dawes, 1985). Fatigue pre-cracking involves cyclically loading and unloading the specimen at a load well below that expected to cause failure, until a crack develops ahead of the notch or stress concentrator, and is visually monitored until it reaches the desired length.

The decision was made to settle for a simple EDM notch rather than an additional fatigue pre-crack for a number of reasons:

- The sensitivity analysis suggested that the crack length was critical to the stress intensity factor and so it was important to be certain of its exact dimensions. The cracks grown using this method would be significantly harder to measure than those inserted using purely EDM.

- The thinnest available EDM wire available was of a 0.1 mm diameter. The exact width of the final cut would be dependent on the material

	a	B	W	S_i	S_o
x_{k-1}	9.95	9.81	19.74	39.00	89.00
x_k	10.00	10.00	20.00	40.00	90.00
x_{k+1}	10.05	10.19	20.26	41.00	91.00
Δx_i	0.05	0.19	0.26	1.00	1.00
y_{k-1}	1.46E-01	1.60E-01	1.64E-01	1.60E-01	1.54E-01
y_k	1.57E-01	1.57E-01	1.57E-01	1.57E-01	1.57E-01
y_{k+1}	1.70E-01	1.54E-01	1.51E-01	1.54E-01	1.60E-01
$\left(\frac{\partial y}{\partial x_i}\right)_k$	-2.41E-02	1.57E-02	2.39E-02	3.15E-03	-3.15E-03
s^2	1.75E+01	6.13E-06	2.14E-09	3.74E-11	3.74E-11

Table 4.4: table showing upper and lower bound values and partial derivative approximations for small specimens ($\lambda = 1/3$)

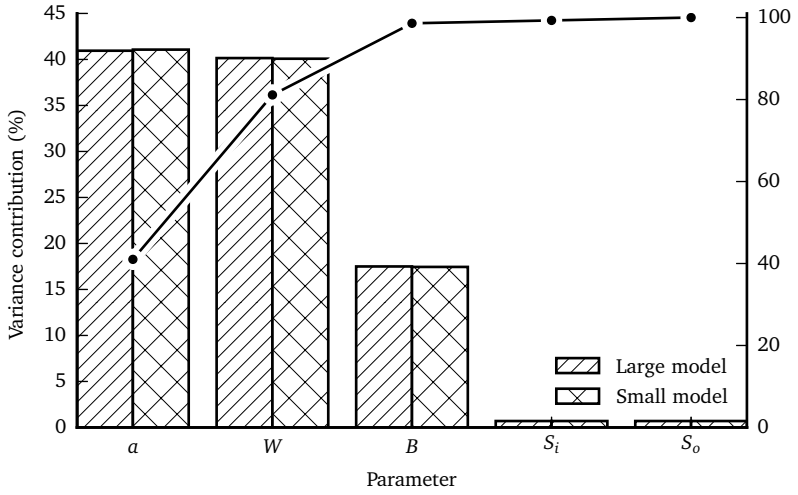

Figure 4.4: Pareto chart showing the relative contributions to overall variance

and dielectric fluid properties, as well as the EDM machine settings, but based on prior work using the same machine on aluminium it was estimated that the notch width and diameter would be approximately 0.15 mm. Previous research (Kamat, 1991) on the effect of the notch radius in an 8000 series aluminium alloy suggested that there was a critical radius, 140 µm, below which the notch could approximate a crack. This was almost double the predicted radius for the EDM notches, and so was deemed to be sufficient.

- Fatigue precracking requires additional specimen preparation, such as polishing, before the cracks can be inserted (Ávila et al., 2016). The additional time it would take to fatigue pre-crack and then measure the crack length for every specimen would be significant, when the above suggested that an EDM notch would suffice.

To add further confidence to this decision, a simulation was carried out modelling the beams featuring a sharp crack, loaded up to the approximate expected failure load. A refined mesh was included around the crack tip so as to observe the distortions occurring during loading. It was observed that crack tip blunting was predicted by the finite element model, as shown in Fig. 4.5, of the same order of magnitude as the radius of the EDM notch. Consequently it was expected that EDM notches would behave similarly to sharp crack.

The EDM crack lengths and radii were to be measured using a shadowgraph profile projector, to ensure the correct stress intensity fractures were calculated.

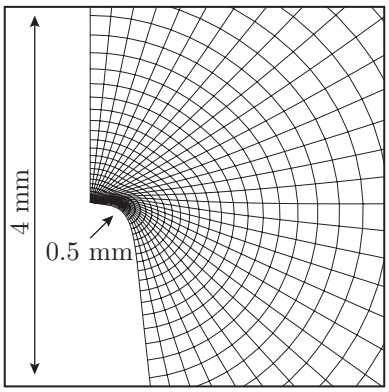

Figure 4.5: A finite element model showing the mesh around the crack tip, and an exaggerated deformation highlighting the blunting that was expected from a sharp crack in the aluminium

4.3.3 Experimental method

Two testing machines were used for the experiment. The same Instron 1342 250 kN machine as used in the tensile testing was used with the larger specimens. For the smaller beams, a 25 kN Roell Amsler HCT test machine was used, as it was capable of supporting the smaller mount for the bending rig.

Each specimen was manually aligned, before being monotonically loaded, at a rate of $1\,\mathrm{mm\,min^{-1}}$ and $0.5\,\mathrm{mm\,min^{-1}}$ for the large and small specimens respectively. Loading continued until fracture occurred. The load and displacement data was again recorded using the Bluehill software. The results obtained from this experiment are discussed in Section 5.2.

4.4 Scaling specimens containing residual stress field

4.4.1 Introduction

An experiment was then devised to investigate the scaling of stress fields in the presence of stress concentrators, and to explore difficulties associated in the measurement of these stress fields when scaling dimensions using neutron diffraction. The focus of the experiment was on the effects of generalised scaling, rather than of a specific material, and so for continuity the same aluminium 7449 alloy was used.

The aim of this experiment was to introduce the same residual stress field into two different sized specimens using the scaling law described by Eq. (3.2) in Chapter 3, where the applied loads have to be scaled according to:

$$P_{\mathrm{m}} = \lambda^2 P_{\mathrm{p}}.$$

An area of initial concern in this experiment was the plastic zone (discussed in Chapter 2) that would form ahead of the crack tip as a result of the stress singularity, and its effect on the resultant stress field. The shape that this plastic zone takes is dependent on the material and loading, and there have been many approximations that attempt to calculate it for both plane stress and plane strain boundary conditions. Regardless of the assumptions made however, these approximations take the form of:

$$r_p = \frac{K_{\mathrm{I}}^2}{\sigma_{ys}}\gamma, \tag{4.8}$$

where r_p is the radius of the plastic zone, σ_{ys} is the yield stress and γ is a function containing material properties and constants, which is dependent on the approximation being used.

As discussed previously in Chapter 3, Section 3.2, the relationship between the stress intensity factors in two different sized models containing the same stress fields is given by $K_{\mathrm{I\,m}} = K_{\mathrm{I\,p}}\lambda^{0.5}$. Consequently it follows that if $r_p \propto K_{\mathrm{I}}^2$, then $r_p \propto \lambda$, and so the stress fields should still scale even close to the crack tip.

4.4.2 Specimen design

Specimen criteria

The specimens again had to meet certain criteria:

- The experiment was to focus on residual stress fields in scaled specimens in the presence of stress concentrators, and so once again all dimensions needed to be geometrically scaled by a chosen scale factor.

- The resultant residual stress field in the plane perpendicular to the crack front should act to open the crack i.e. be tensile. They also needed to be of sufficient magnitudes to be reliably measured using neutron diffraction. Errors associated with neutron diffraction are discussed further in Section 5.3.3, and their magnitudes are dependent on count times, gauge volume sizes, material absorption, etc. Having larger stresses in the material typically makes the results easier to measure however.

- Once again the maximum and minimum size of the specimens was constrained by the loading test machines available.

- In addition to the loading rigs, the neutron diffraction facility presented additional constraints. The neutron diffraction measurement method is discussed in more detail in Section 4.4.3, but the smallest

specimen had to be large enough to allow for sufficient points to be measured given the potential gauge volumes, and the largest specimen had to be small enough to allow for practical measurement times given the distance the neutron beam would have to travel through. Gauge volumes can typically be as a large as required, however the lower limit is defined by the collimators, and is typically in the order of $1\,mm^3$. Measurement times depend on the absorption rate of the material, the beam intensity, the gauge volume size, and consequently can range from minutes to hours.

Methods of introducing a residual stress field

Bearing these points in mind, the decision was made to once again use SENB specimens as they were easily loaded and scaled. The exact dimensions of the SENB specimens would depend on the loading method, but an estimated minimum uncracked ligament length of 12 mm would provide enough material for at least 6 points, using an estimated gauge volume size of $2\,mm \times 2\,mm \times 2\,mm$. The relatively low toughness of the aluminium presented a problem however, as it meant the specimens were likely to fracture before a substantial residual stress field could be introduced. A number of methods for introducing known residual stress fields were considered, including *in-plane compression* and *side punching*, both of which were commonly used in the research community for introducing stress fields (Mahmoudi et al., 2006).

In-plane compression consists of overloading the specimen in the plane perpendicular to the crack face, so as to close it during loading and the result being a tensile residual stress field upon unloading. An additional stress concentrator such as a blunt notch before the crack is often used. An ABAQUS finite element model was run, using the material properties from Section 4.2, to assess the feasibility of using this method to generate a stress field ahead of the crack tip. The results showed that the required load was impractical however, and so this method was not used.

Side punching uses two hard punching tools (one on either side of the specimen) to compress the specimen ahead of the crack tip and in the axis of the crack front. The result is a residual stress field that can be either compressive or tensile ahead of the crack, depending on the magnitude and location of the punch. Finite element analysis of this method again suggested that the loads required would be very large, and that even then the resultant stress field might not act to open the crack and focus the stress around the tip.

Quenching is often used to introduce stresses, as the rapid change in temperature, combined with the varying rates of thermal expansion result in highly triaxial residual stresses (Hossain et al., 2006; Hosseinzadeh et al., 2009). The quenching process is highly dependent on the physical proper-

ties of the water and experimental setup, however, which would be difficult to control so as to ensure consistency across both specimens. Furthermore, quenching would introduce new scaling laws, based on temperature and the physical phenomena associated with quenching, that would require further research before being used in this context.

Instead, a method for generating a residual stress field was proposed which consisted of a reversed four point bend loading configuration. By loading the specimens in reverse ,the cracked side of the specimen would be in compression throughout the loading phase. Provided the crack length was short enough that it did not extend beyond the neutral axis, then the crack front should not encounter any strong tensile residual stresses at this point, meaning bending could occur without fracture. Upon unloading, the redistribution of stresses should result in a large tensile residual stress ahead of the crack front.

A similar method of generating residual stresses was used by Towers and Dawes (1985) with reverse loaded fracture toughness specimens, however no analytical solution was proposed for the resultant stresses. As nothing could be found in the literature for the stresses produced using this method, finite element analysis had to be relied upon.

Determining optimum crack length

The same geometry SENB specimens were chosen for this experiment, but as mentioned with a modified crack length so as to keep the crack in the compressive zone during bending. A series of finite element simulations were carried out with varying crack lengths, with the aim of finding an a/W ratio that produced a large residual stress field whilst not requiring an impractically large load, which are described below.

A "template" was first devised for the experiment, and a python script then written to produce a series of models based on this with varying crack lengths, which then outputted the stress field in the uncracked ligament ahead of the crack. During the simulations it became apparent that whilst the smallest specimen used in the previous experiment provided approximate suitable dimensions, the large specimens would require too large a force to produce any measurable stress field using this method. Consequently the scale factor λ was changed to 0.5. The inner roller spacings were decreased so as to reduce the force required to plastically deform the beam, however the outer rollers were kept in the previous position, with the final configurations shown in Fig. 4.8. The simulations utilised the dimensions of this larger specimen, which were loaded to 100 kN (the maximum load the available bending rigs were rated for), before being unloaded, with a series of cracks up to $a/W = 0.5$ simulated.

Previous models similar to this had been carried out by modelling the crack as a face lacking the symmetrical boundary conditions that the rest of

the model used. Due to the crack in this model closing rather than opening however, it was deemed that this approach may not have been sufficient, and so the crack was modelled more accurately as a notch with a radius of 0.075 mm. This required a significantly finer mesh around the crack tip than in previous models, and so in order to improve the runtimes, submodels were used. First a course mesh of approximately 3500 quad elements was used to calculate the global stress field; this was then applied to a submodel of approximately 40 000 quad and wedge elements that focussed on the crack area. This is shown in Fig. 4.6. The mesh shown is for an a/W ratio $1/3$, however each mesh varied slightly and was dependent on the crack length.

The quality of these meshes was checked by switching the top and bottom support pins, such that the crack opened in a normal four point bend configuration. This four point bend was then simulated using elastic material properties for an arbitrary load, and the resultant stress intensity factor compared to that calculated using Eqs. (4.3) and (4.4). The results suggested that this mesh was appropriate for use with a notch.

Figure 4.7a shows the residual stresses across the uncracked ligament predicted by the simulations. All crack lengths show similar stress distributions, featuring a large tensile stress directly ahead of the crack tip, followed immediately by a similar magnitude compressive stress, which is then followed again by tension. One of the criteria for the specimen designs was to allow for large magnitude residual stresses to be introduced, and Fig. 4.7a suggests that the larger the crack length, the larger the residual stresses close to the crack. This also reduces the available material for the stresses to be measured over. However, as neutron diffraction measures over discrete areas, the results will be of lower resolution. Figure 4.7b shows the stresses ahead of the crack tip, un-normalised. Based on these results an a/W ratio of 0.35 was chosen, corresponding to 7 mm and 14 mm for the small and large beams respectively, on the basis that it would allow for both a large residual stress to be introduced, as well as enough space for measurements to be made afterwards.

Determining the importance of crack width

Finally, the method of inserting the crack had to be decided. In the previous fracture experiments described in Section 4.3, the thinnest available wire had been used to approximate a crack. With the specimens being loaded in reverse for this experiment, however, a large proportion of the applied force would be transferred across this closed crack face. The width of the crack was predicted to play a large part in this initial loading and the resultant residual stress field. Consequently, not scaling the crack widths for this experiment was predicted to have a much larger effect. To verify this, two additional models, based on Fig. 4.6, were run of the large and small beams,

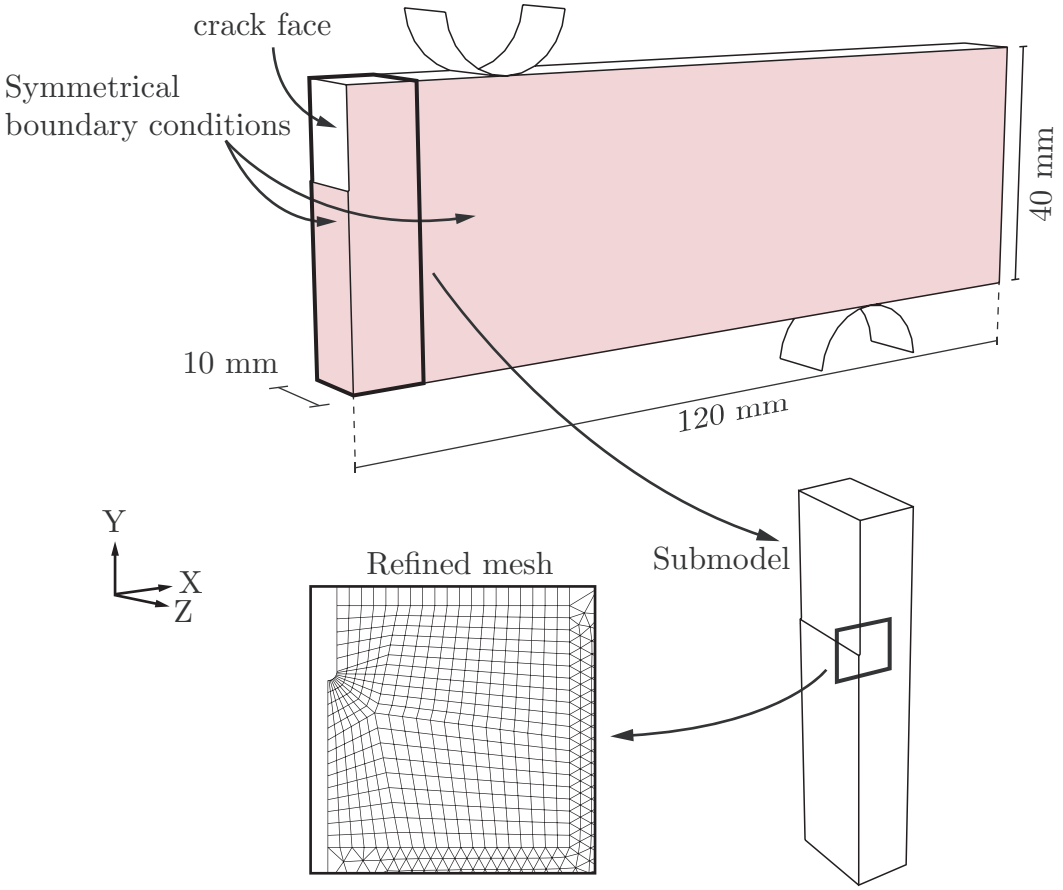

Figure 4.6: Schematic for finite element models used in assessing effect of crack width on residual stress field

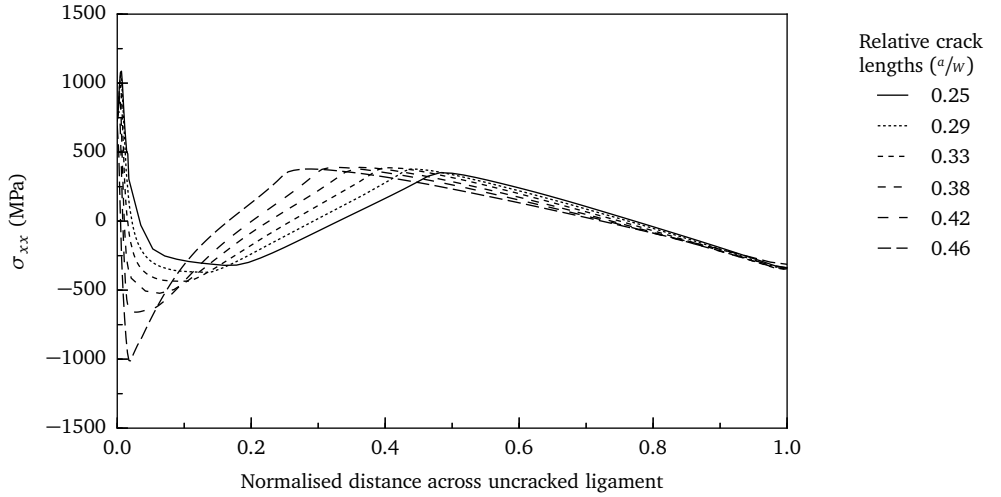

(a) Residual stresses after unloading for varying crack lengths, normalised against ligament size

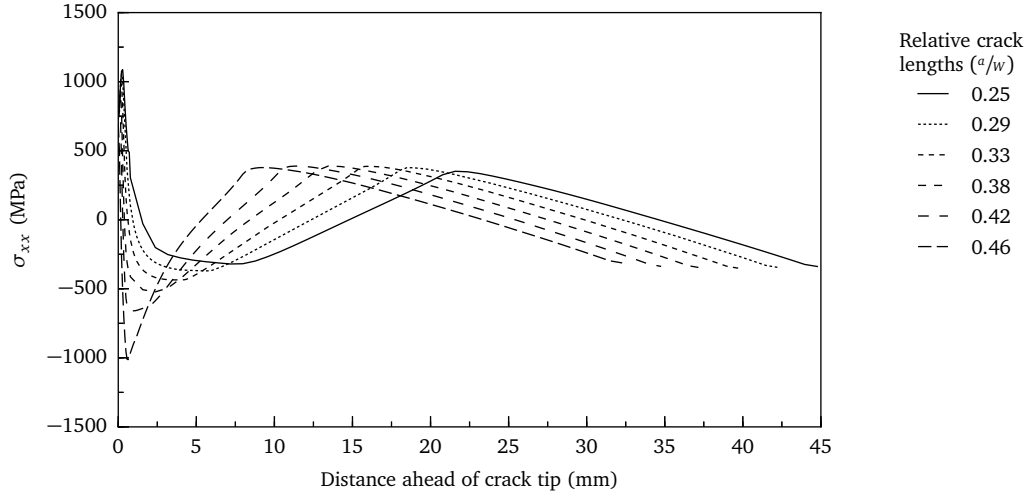

(b) Residual stresses after unloading ahead of the crack tip for varying crack lengths

Figure 4.7: Residual stresses ahead of the crack tip, shown normalised against ligament length, and un-normalised

both using 0.075 mm radius cracks. The predicted load displacement curve, and resultant residual stress field across the uncracked ligament, are shown in Figs. 4.10 and 4.11.

The models clearly predict a different loading response and measurable effect on the residual stress field, and consequently it was decided that for this experiment it made more sense to accurately scale the crack radii, rather than treating them as singularities. The final dimensions of the specimens, and the loading setup used, are shown in Fig. 4.8

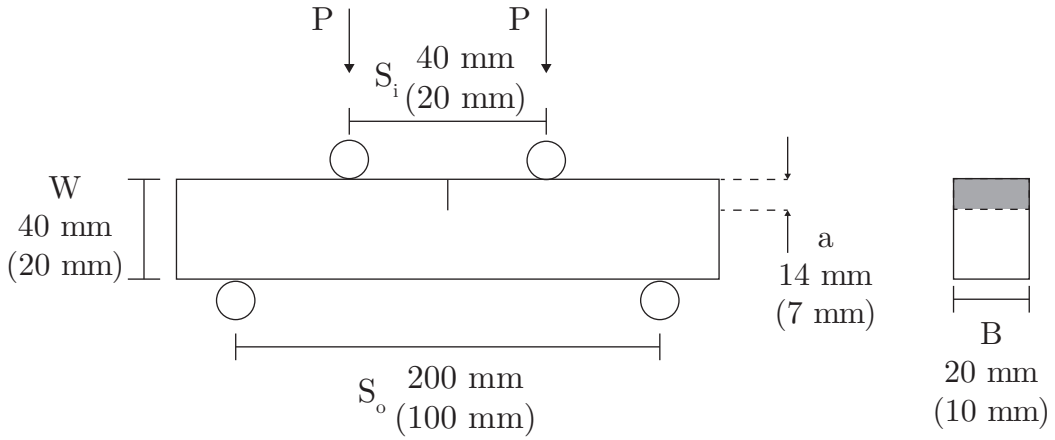

Figure 4.8: Schematic showing final dimensions of scaled residual stress specimens

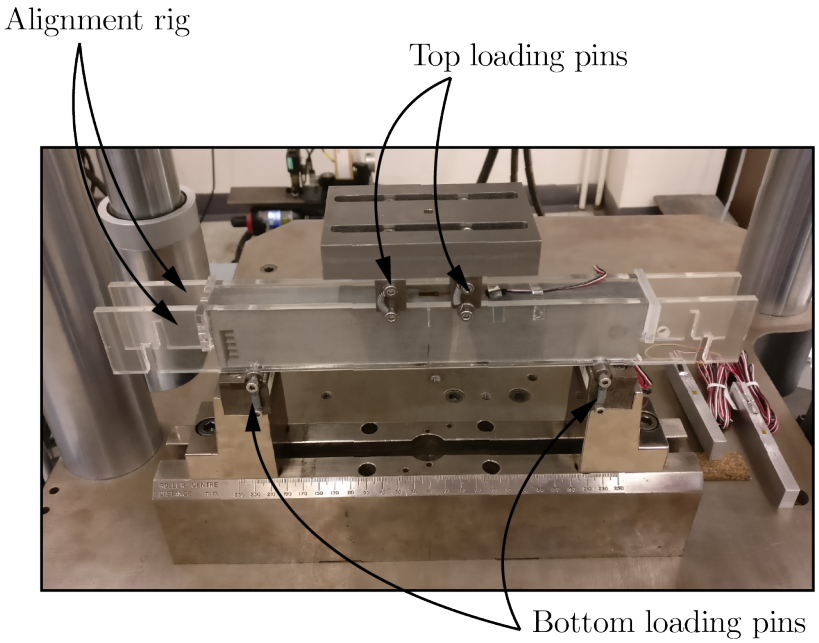

Figure 4.9: Photo of alignment rig used for generating residual stress field. The specimen was placed inside the alignment rig, which then allowed for pins to be aligned relative to the beam using using cut outs, ensuring the pin spacings were accurate and correctly positioned

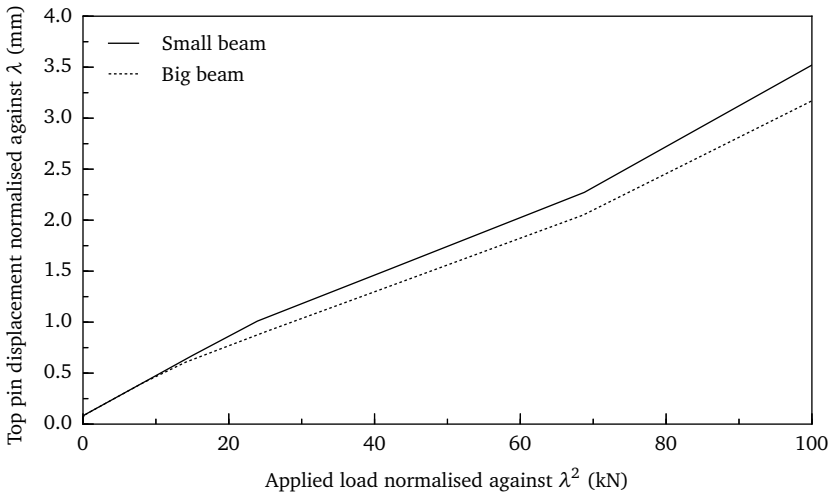

Figure 4.10: Normalised load displacement graph showing effect of unscaled crack width

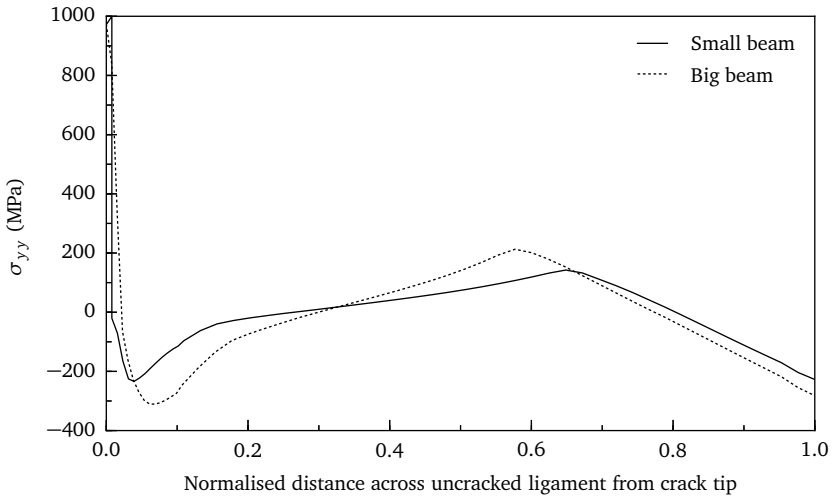

Figure 4.11: Residual stresses across uncracked ligament if cracks are not scaled

4.4.3 Experimental method

Generating residual stress field

In order to introduce the residual stress field into the specimens an Instron 500 kN compressive loading rig was used. This testing machine presented a number of benefits over the Instron 1342, namely rather than placing the loading rigs in hydraulic grips (which are difficult to align), they are simply placed on the specimen and loaded directly via the crosshead. In order to

aid with the alignment of the specimens and the loading pins, two frames were laser-cut out of acrylic; the frames had cut-outs at the appropriate locations for the top and bottom loading pins, so as to ensure the spacing was correct and that they were aligned symmetrically, and side inserts that made sure the specimen was aligned correctly in the centre. The rig was designed such that it could be disassembled, leaving the aligned specimen in place, ready to be loaded. This is shown in Fig. 4.9

The small and large specimens were loaded up to 25 kN and 100 kN at a rate of 0.5 mm min^{-1} and 1 mm min^{-1} respectively. Strain gauges were initially attached to each of the specimens for comparison with the finite element models, however due to errors in their application these were unusable.

Neutron diffraction measurements

As previously mentioned, the residual stress fields in the beam were to be measured using neutron diffraction in the uncracked ligament along the line shown in Fig. 5.13. Traditional destructive stress measurement techniques were initially considered before opting for this technique, however, the two measurement lines meant that multiple specimens would have been required, and they would have had difficulty in producing triaxial stress measurements.

Neutron diffraction measurements use Bragg's law, which describes the diffraction of radiation by a crystal lattice structure and is given by:

$$n\lambda = 2d \sin\theta, \tag{4.9}$$

where λ is the radiation wavelength, θ is the scattering angle and d is the lattice plane spacing (Fitzpatrick and Lodini, 2003), as shown in Fig. 4.12.

Measurements are typically carried out on an additional stress free sample to produce its lattice spacing, d_0, from which the strains can then be calculated using:

$$\varepsilon = \frac{d - d_0}{d_0}. \tag{4.10}$$

The measurements were carried out using the E3 diffractometer at the Helmholtz Centre in Berlin, using neutrons of wavelength 1.47 Å and gauge volumes of 2 mm $\times$ 0.5 mm $\times$ 2 mm for the small beam, and 2 mm $\times$ 1 mm $\times$ 2 mm for the large beam. The E3 diffractometer is a reactor source (as opposed to a spallation source), and so particularly suited to this single phase material due to the high intensity monochromatic beam (Fitzpatrick and Lodini, 2003). Ideally the gauge volumes would have been completely scaled, however, instrument constraints meant this was not possible. The gauge volumes themselves are defined using a slit of variable width, which

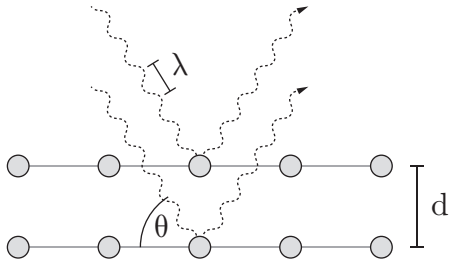

Figure 4.12: Diagram showing key parameters used in Bragg's law equations

controls the width of the incoming neutron beam, and then either by a secondary slit or a radial collimator, which defines the cross section of the outgoing neutron beam. This is illustrated in Fig. 4.13. The results are discussed in the following chapter, in Section 5.3.

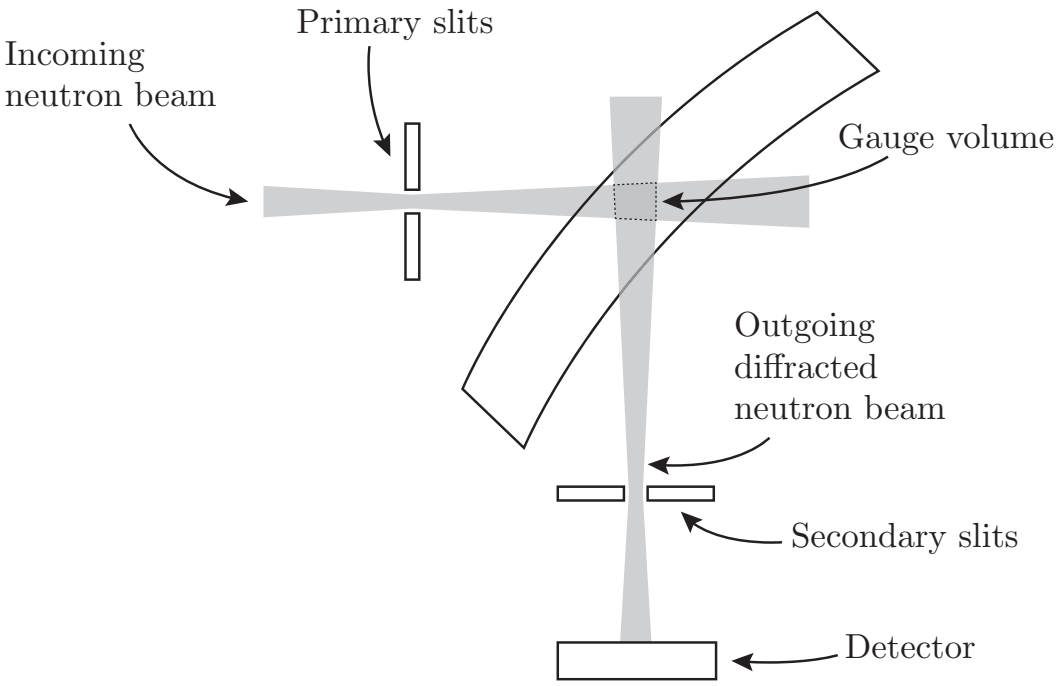

(a) Definition of the gauge volume using secondary slits

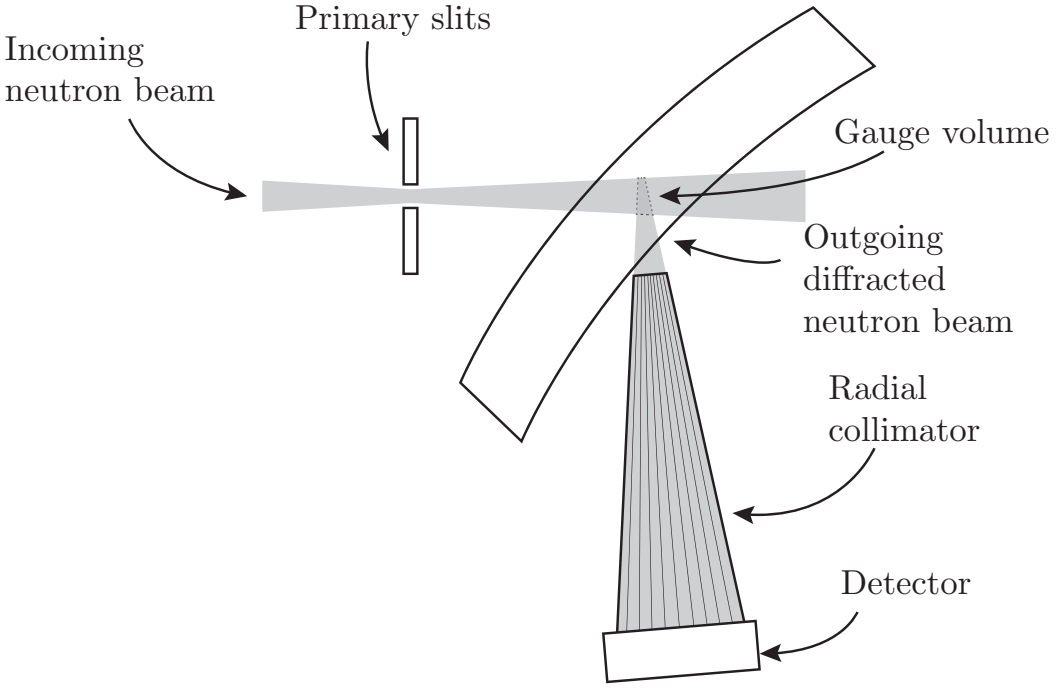

(b) Definition of the gauge volume using radial collimator

Figure 4.13: Illustration showing the definition of the gauge volumes using slits and radial collimators

Chapter 5

Experimental results

5.1 Introduction

This chapter presents the results from the fracture and residual stress experiments described in Chapter 4, as well as discussing the challenges encountered while carrying them out. Modifications to the original experiment design will also be described. The methods used to process the results are then explained, and the final results discussed.

The fracture experiments were relatively straightforward to plan for in terms of time, with the largest unknowns going into them being how long it would take to apply the failure loads. These were relatively short in comparison to the amount of time required to set up and align each specimen, and so did not have a great impact on the overall experiment. The neutron measurements were dependent on the beam, however, which went down at various points throughout the experiment with no warning. The count times for neutron diffraction measurements are often difficult to predict, when using previously untested material (Withers, 2004). The measurement times are dictated by the absorption of the material, the grain structure, and the consequent scattering of the beam, the background noise, etc. Based on previous research conducted using this material, provisional count times of an hour per measurement point, were allocated.

5.2 Scaled fracture tests

5.2.1 Results

The unprocessed data recorded during the scaled fracture experiment consisted of the applied load and the displacement of the crosshead. Figure 5.1 shows the final loads and displacements up to the point of fracture. The data has not been normalised and the difference between the failure loads for the large specimens and small specimens is clear. All specimens exhib-

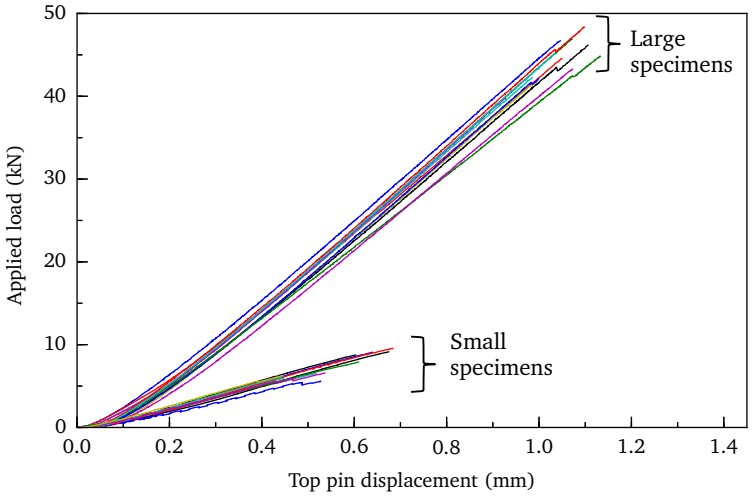

Figure 5.1: Experimental data showing top displacement against load data, captured during fracture tests, for the specimens described in Section 4.3, and shown in Fig. 4.3

ited a clear point of failure, where the load immediately dropped to almost 0 kN, as shown and highlighted in Fig. 5.2 for one of the large specimens. The data was recorded at a rate of 10 data points per second, and this drop from peak load to 0 kN was registered over the course of a single data data point for the majority of the specimens.

Invalid results

The bending of the large specimens was undertaken with no problems, however, when bending a number of the smaller specimens, the rollers slipped due to not being fastened securely enough to the test machine. It is not immediately obvious from Fig. 5.1 that this happened, however when viewed separately, the jagged lines as a result of the slipping are much clearer, as shown in Fig. 5.3. In total, the results from six specimens were invalidated in this manner.

Crack propagation

An unexpected observation made when conducting the experiments was that the cracks all initiated perpendicularly to the original EDM notch, as shown in Fig. 5.4. In measuring the crack radii, as described in Section 4.3 using a magnification of 100 $\times$, no additional visible stress concentrating features were found around the perimeter of the crack that might have lead to the cracks growing in this manner. This crack initiation behaviour was consistent for all specimens, and appeared to be unaffected by size.

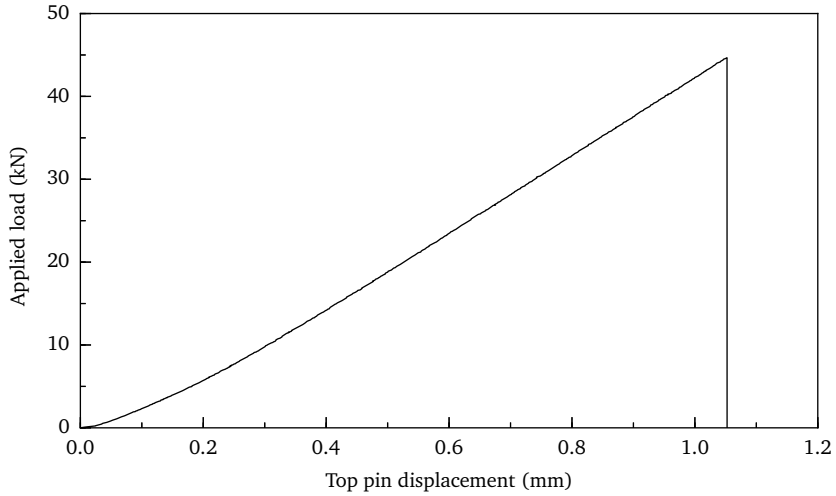

Figure 5.2: Results for a large specimen showing sudden failure

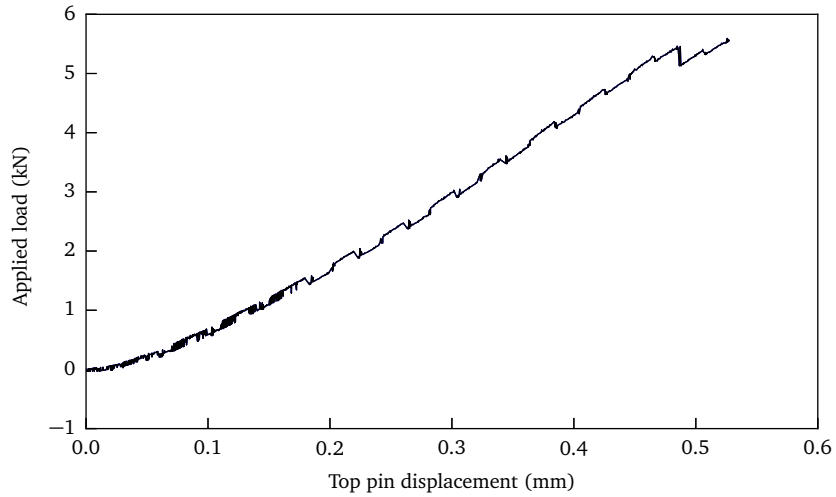

Figure 5.3: An example of one of the results that was invalidated due to slipping of the components

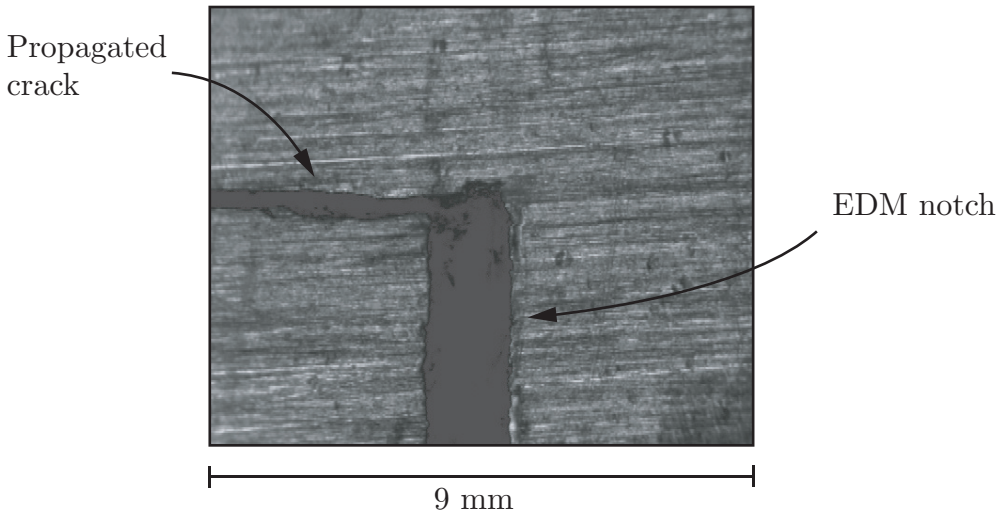

Figure 5.4: Magnified photo ($\times$100) of a fractured specimen showing initial perpendicular crack growth

Stress intensity factors

Examining the displacement-load curves in Fig. 5.1, the straightness of each of the lines suggests that the bending had resulted in very little plasticity at the point that failure occurred, and therefore that these failures would have been almost entirely a consequence of brittle fracture.

As discussed in Section 2.3, failures occurring as a consequence of brittle fracture are governed by the fracture toughness, and so the stress intensity factors were expected to be approximately equal for both sizes. Equations (4.3) and (4.4) were used to calculate the K_{I} values at failure for these configurations, and the results are plotted in Fig. 5.5 against top pin displacement again.

At first glance the results appear to show broadly similar values of K_{I} for both size beams, however the failures for the smaller beams display much more scatter than the larger beams, meaning the results require further analysis than simply looking at the graph.

The results from the experiment were thought to have occurred as a result of cleavage fracture (as opposed to ductile fracture), where the fracture occurs rapidly along the crystallographic plane, as no plasticity was detected in any of the load displacement curves.

The three parameter Weibull distribution is given by:

$$p_f = 1 - \exp\left[-\left(\frac{K_{\mathrm{I}} - K_{\mathrm{min}}}{K_0 - K_{\mathrm{min}}}\right)^{m_1}\right], \tag{5.1}$$

where p_f is the probability of fracture, K_0 is a normalisation factor that encompasses 62% of the data, m_1 describes the scatter of the data and K_{min} is a minimum K_{I} below which cleavage fracture becomes impossible.

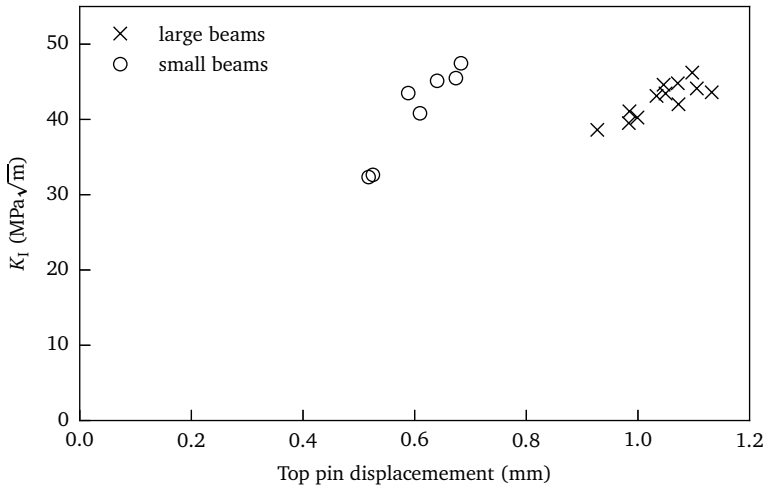

Figure 5.5: K_I at failure against displacement

In order to fit a distribution to the data, a Python script was then written which iterated through a range of possible K_{min} values, allowing for the values of K_0 and m_1 to be found for each iteration that produced the best fit, eventually identifying the parameters from this range. This method is sometimes called the "least squares" method, and is a common computational method of estimating the Weibull parameters (Kao, 1958; Hossain and Zimmer, 2003). Python was chosen rather than calculating and verifying the parameters by hand, as this would have been a very labour intensive process, which would then have had to be repeated for the second set of data. A more detailed description of the script now follows:

5.2.2 Calculation of the Weibull parameters

Equation (5.1) was to be rearranged so that a line of best fit could be fitted of the form $y = mx + c$, so that

$$1 - p_f = \exp\left[-\left(\frac{K_I - K_{min}}{K_0 - K_{min}}\right)^{m_1}\right].$$

The natural logarithm of both sides was then taken, to give

$$\ln\left(1 - p_f\right) = -\left(\frac{K_I - K_{min}}{K_0 - K_{min}}\right)^{m_1},$$

after which both sides are subtracted from each other,

$$-\ln\left(1 - p_f\right) = \left(\frac{K_I - K_{min}}{K_0 - K_{min}}\right)^{m_1},$$

and the natural logarithms taken again to give

$$\ln\left(-\ln\left(1-p_f\right)\right) = \ln\left(\frac{1}{\ln\left(1-p_f\right)}\right)$$

$$\ln\left(\frac{1}{\ln\left(1-p_f\right)}\right) = m_1 \ln\left(\frac{K_\mathrm{I}-K_\mathrm{min}}{K_0-K_\mathrm{min}}\right)$$

$$= m_1 \ln\left(K_\mathrm{I}-K_\mathrm{min}\right) - m_1 \ln\left(K_0-K_\mathrm{min}\right),$$

resulting in the final form of the equation,

$$\ln\left(\frac{1}{\ln\left(1-p_f\right)}\right) = m_1 \ln\left(K_\mathrm{I}-K_\mathrm{min}\right) - m_1 \ln\left(K_0-K_\mathrm{min}\right). \tag{5.2}$$

The data was then ranked using the median ranking method, as this is the typically used method for use with a Weibull distribution (Booker et al., 2001), and which is given by:

$$F_i = \frac{i-0.3}{N+0.4}, \tag{5.3}$$

where F_i is the ranked value for ith variable, i is the cumulative frequency of the variable, and N is the population size.

An array of possible K_min values was then generated; the physical meaning of K_min is to provide a value below which, despite the scatter, fracture will not occur, and so it made sense to constrain this between 0 MPa$\sqrt{\mathrm{m}}$, and maximum value it could take, which was the lowest experimental result.

For each value of K_min in the array, a line of best fit was calculated for

$$\ln\left(\frac{1}{\ln\left(1-p_f\right)}\right) = \ln\left(K_\mathrm{I}-K_\mathrm{min}\right). \tag{5.4}$$

The slope of the line was then calculated, which was equal to m_1, and finally the intercept, c, which was equal to:

$$c = -m_1 \ln\left(K_0-K_\mathrm{min}\right), \tag{5.5}$$

leading to a K_0 value of:

$$K_0 = \exp\left(-\frac{c}{m}\right) + K_\mathrm{min}. \tag{5.6}$$

The coefficient of determination, R^2, was then calculated, so as to determine how well the data fit the model, where a value of 0 indicates no correlation,

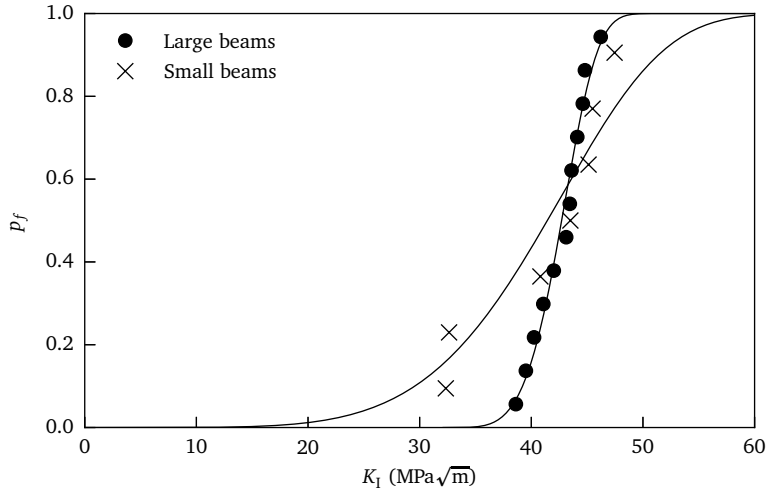

Figure 5.6: Data from fracture tests with fitted Weibull curves

and a value of 1 meaning the model fits the data perfectly (Walpole et al., 2002). The coefficient of determination is given by

$$R^2 = 1 - \frac{\text{SSE}}{\text{SST}}, \tag{5.7}$$

where SSE and SSE refer to the residual sum of squares, and the total sum of squares. The residual sum of squares is given by

$$\text{SSE} = \sum_{i=1}^{n} (y_i - \hat{y}_i)^2, \tag{5.8}$$

where y_i is the measured data points, and $\hat{y}_i$ is the value predicted by the line of best fit, and so describes the total differences between the measured data and the predicted values according to the model. The total sum of squares is given by

$$\text{SST} = \sum_{i=1}^{n} (y_i - \bar{y})^2, \tag{5.9}$$

where $\bar{y}$ describes the mean of the measured data, and consequently the SST describes the spread of the data around the mean.

The script then repeated the process, iterating through every value of K_{min} in the array, then selecting the parameters that produced the closest fitting Weibull distribution. The results from this process are shown in Fig. 5.6, with the final Weibull parameters given in Table 5.1

The results show that despite the scatter, the K_0 value for both sizes is virtually identical, differing by less than 1 MPa$\sqrt{\text{m}}$. Given the brittle nature of the failures and the material, this makes sense, however had the specimens differed significantly more in size then this may not have been the case.

Table 5.1: Calculated Weibull parameters from fracture tests

	K_0 (MPa$\sqrt{\text{m}}$)	K_{min} (MPa$\sqrt{\text{m}}$)	m_1
Large beams	43.58	32.08	4.71
Small beams	44.25	0.00	5.58

5.2.3 Failure assessment diagram

As discussed in Section 2.4, failure assessment diagrams allow for the comparison of failure loads and the type of failure, independent of size, provided the geometry and method of loading are identical.

An option 3 FAD was generated using the material data gathered in Section 4.2 and ABAQUS models. The models consisted of two separate analyses calculating the J-integral around the crack tip, one using elastic-plastic material data, and the other using only elastic, to obtain the necessary J and J_e values required to plot the FAD. Both models used identical meshes consisting of approximately 12 400 quadrilateral elements, which as usual were focused around the crack tip to produce a refined mesh around the area of interest, as shown in Fig. 5.7. As the specimens were symmetrical only quarters were modelled, taking advantage of the planes of symmetry to reduce the computation time.

The models were both simulated being loaded up to P_L^{max}, just beyond their respective limit loads, P_L, which were in turn calculated using Eqs. (5.10) and (5.11),

$$P_L = \sigma_y B W^2 \left(1 - {}^{a}/_{W}\right)^2 \left(\frac{1.2606}{S_o - S_i}\right), \tag{5.10}$$

$$P_L^{\text{max}} = P_L \left(\frac{\sigma_y + \sigma_{\text{UTS}}}{2\sigma_y}\right), \tag{5.11}$$

where S_o and S_i are the outer and inner roller spacings, respectively, and σ_{UTS} is the ultimate tensile stress.

The failure curve obtained using from these models is plotted in Fig. 5.8, along with two points showing where the two sets of specimens would be expected to fail according to the diagram. A K_{mat} value of 43.92 MPa$\sqrt{\text{m}}$ was used, which was the mean value of the two calculated K_0 parameters. By looking at the FAD we can see that for these size specimens, both would be expected to fail almost completely via brittle fracture with no measurable plasticity.

In this relatively simple case, K_r values are linearly proportional to applied load, and so any additional points plotted would lie on the dotted lines. The slope of these lines therefore scales with $\lambda^{1.5}$, and so we can deduce that as the size of the specimens decreases, the further along the FAD curve the failures will occur, meaning increasing plasticity at failure.

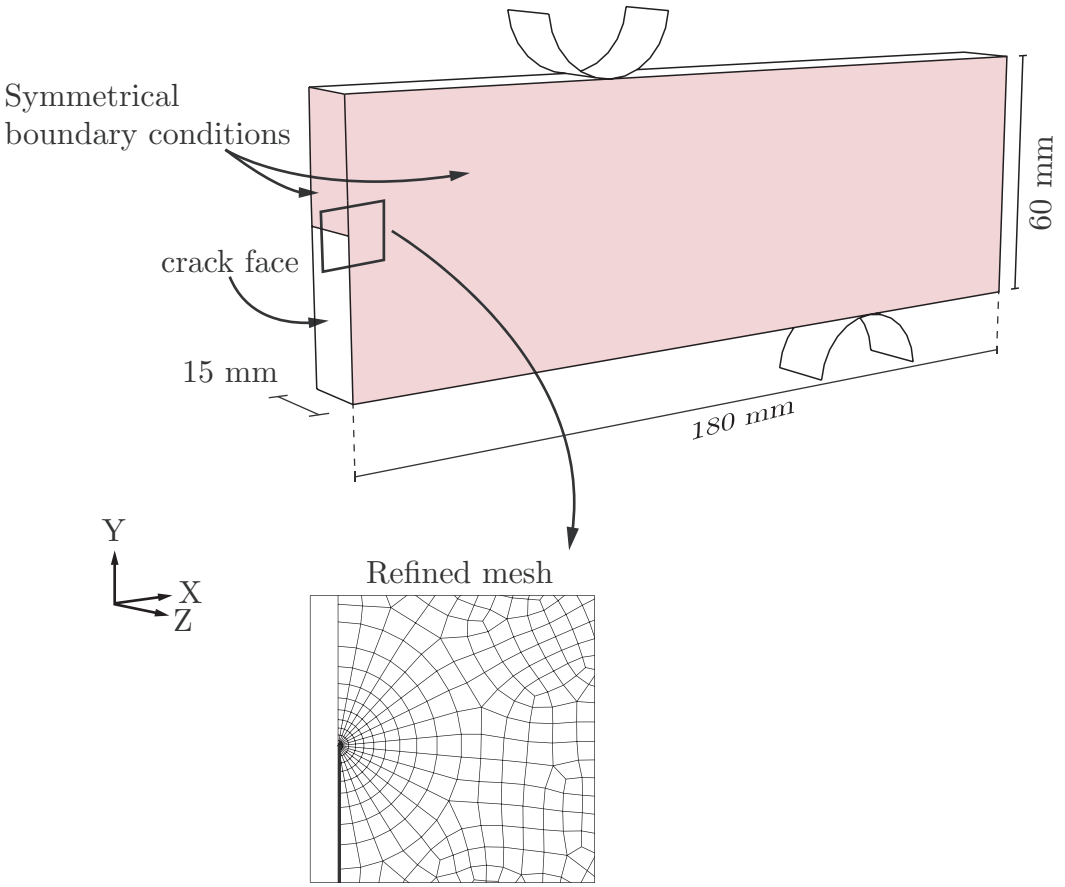

Figure 5.7: Schematic showing the refined mesh used in the failure assessment diagram calculations

Alternatively, the curve can be redrawn, as in Fig. 5.9, showing the K_r value that specimens would be expected to fail at, as a function of the scale factor, and consequently the level of plasticity they would be expected to undergo. It is quite clear that whilst the scale factor is larger than $\lambda = 0.2$, the failures remain almost entirely brittle. When the scale factor falls below 0.2, however, the failures enter the realm of plastic collapse.

5.3 Scaled residual stress specimens

This section describes the results from the bending experiments described in Section 4.4. These experiments involved results from two stages, as unlike the fracture tests which produced results immediately upon completion (albeit requiring further processing), these experiments required a second final measurements stage. Despite this however, measurements were still taken throughout the first stage in the form of load displacement data, which were compared with the finite element models for numerical validation.

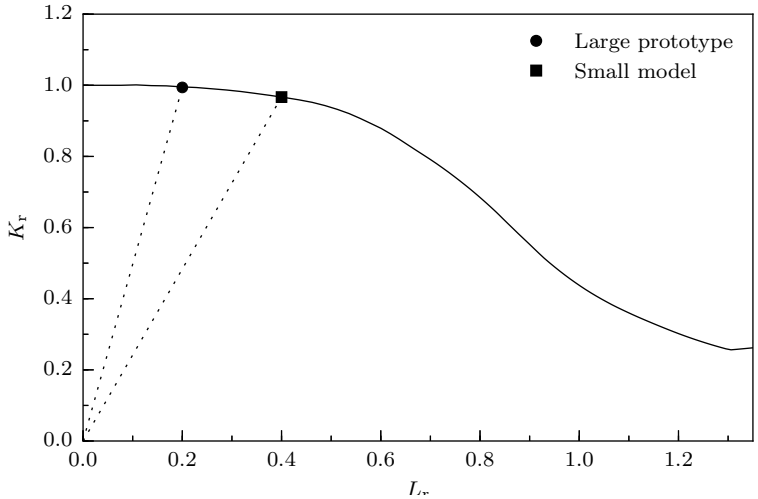

Figure 5.8: Failure assessment diagram showing where both size specimens would theoretically fail

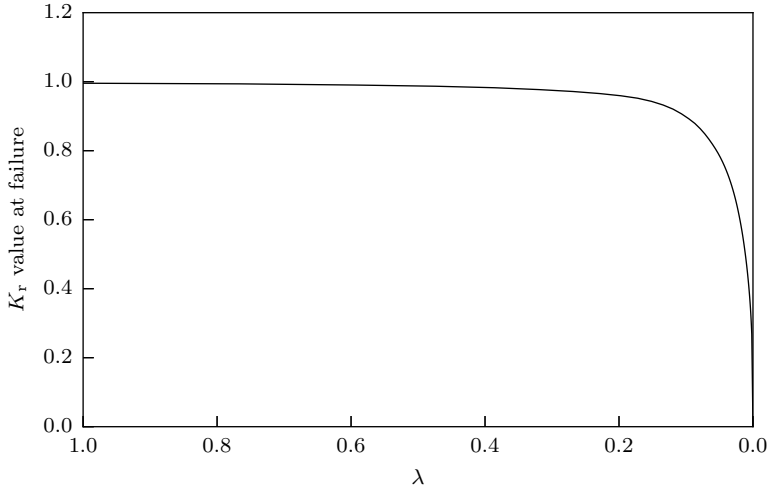

Figure 5.9: Showing the K_r value that specimens would be expected to fail at when scaled with respect to the original large scale four point bend

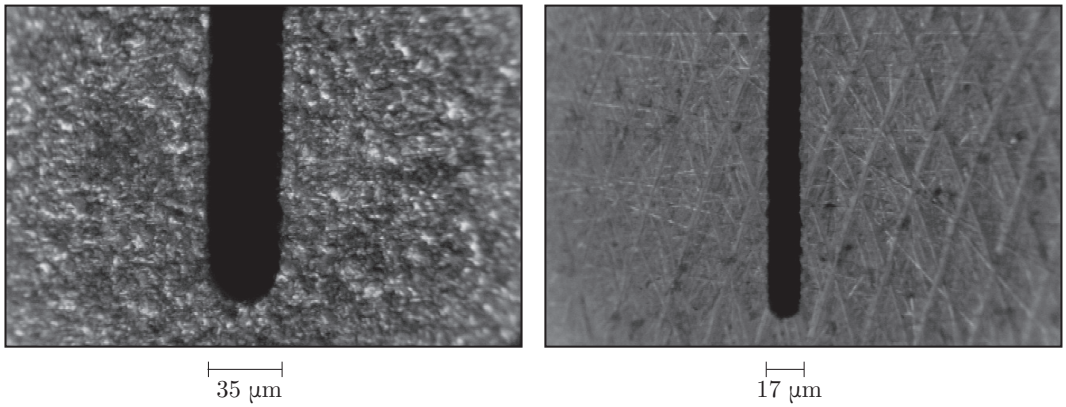

(a) Magnified photo of large beam (b) Magnified photo of small beam

Figure 5.10: Magnified photos showing cracks in small and large beams

5.3.1 Plastic bending and comparison to FEA

The purpose of this experiment was to examine the effect of scaling on the residual stress fields introduced into notched specimens around the crack tip, and so it was important to make sure that the specimens were carefully loaded.

The alignment rig used to ensure that the load was applied symmetrically has already been described, but as well as being aligned correctly, the specimens were also required to be of the expected dimensions; if the specimens were perfectly aligned but the cracks were of different relative lengths, then the results would not match.To ensure this was not the case, the crack radii and lengths were again measured, this time using an Optimax video microscope, which allowed to measurements to be carried out directly using the provided interface. Feeler gauges were also used to ensure the crack width did not reduce on the inside of the specimen. Images of the magnified crack tips from both size specimens are shown in Fig. 5.10. The cracks were found to be 7.02 mm and 14.04 mm in length, with diameters of 0.17 mm and 0.35 mm, and therefore suitably scaled.

The specimens were loaded, as described in Section 4.4, and the applied loads and crosshead displacements recorded, so as to then be compared both with each other, and the finite element predictions. It was clearly important for the load displacement curves to agree between sizes, when normalised, so as to have confidence in the stress fields introduced.

The finite element model has already been described in Section 4.4.2, and the results from the updated model with all the final parameters were ready for direct comparison with the experimental data. The experimental load displacement curves are shown in Fig. 5.11, along with the finite element prediction.

The finite element results showed good agreement with the measure-

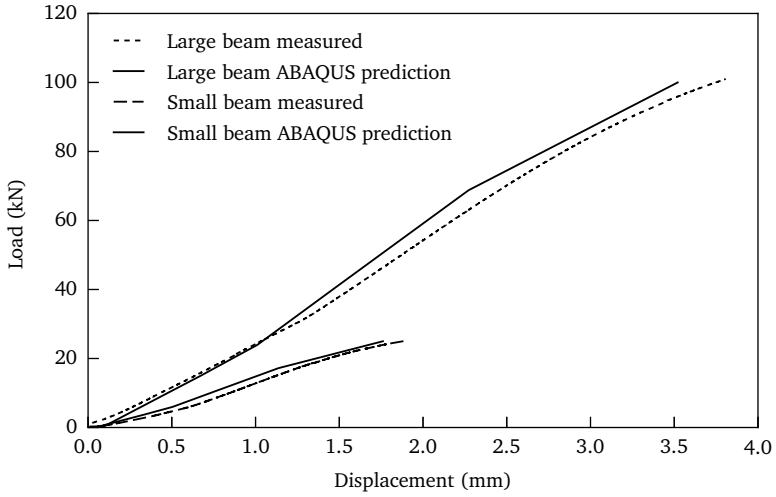

Figure 5.11: The load displacement curves for the plastically deformed specimens, with their respective finite element simulations

ments obtained during the bending, adding confidence to the predicted residual stress fields.

5.3.2 Neutron measurements

Having completed the first stage of the experiment, namely introducing the residual stresses, and having confidence in the similitude between the two applied loads, the next step was to validate the residual stress fields using neutron diffraction. A schematic, showing the sample setup at E3, is shown in Fig. 5.12

Before commencing the actual measurements, the specimens were carefully aligned by first lowering the translation table until completely out of the path of the incoming neutron beam, then gradually raising it until diffracted neutrons were detected. The detector was positioned such that only diffracted neutrons would enter it, with the beam simply hitting the beam stop otherwise, and so precise reference points were able to be obtained with respect to the neutron beam. By repeating this process for various parts of the beams' geometries, reference points were able to be obtained which allowed for the definition of the measurement lines. This alignment method is commonly used when carrying out neutron measurements, as it is both quick and effective (Fitzpatrick and Lodini, 2003).

The results produced from the neutron diffraction measurements were first analysed by the beamline scientist, Dr. Robert Wimpory. This consisted of the peak analysis, converting the scattering angles into the strains, and corresponding stresses, that were of interest in this experiment. His peak analysis also produced the errors, which are discussed further in Sec-

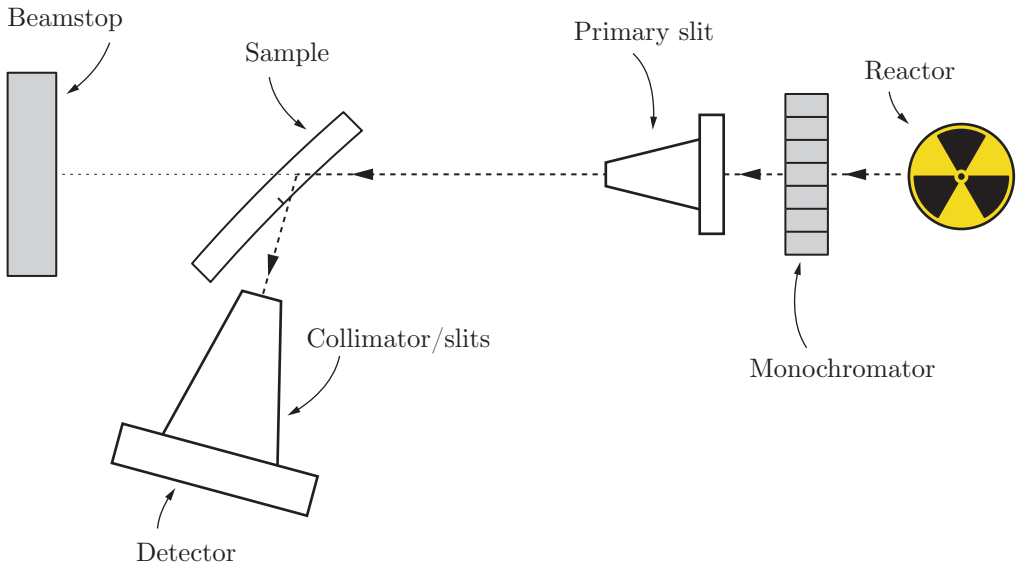

Figure 5.12: Schematic showing the layout of the sample and detector setup at E3

tion 5.3.3.

The two sets of measurements

The first set of measurements were carried out as described in Section 4.4.2, using the planned gauge volumes of 1 mm × 1 mm × 1 mm for the small beam, and 2 mm × 2 mm × 2 mm for the large beam. These initial measurements were carried out using slits to define the gauge volumes rather than the alternative radial collimator, both on the outgoing beam from the reactor, and the incoming beam before the detector. The slits were chosen as they were able to produce the small gauge volumes required to be able to scale exactly, however it also transpired that the slit system let in more background radiation than expected, and consequently resulted in significantly longer measurement times than planned.

In addition to the time constraints imposed by the slow measurement times, an extra hindrance caused by a build up of xenon gas in the reactor resulted in the reactor having to be shut down for 48 hours, meaning that time was extremely limited when carrying out the measurements. Consequently, fewer points were able to be measured than had been planned, resulting in lower resolution stress distributions. Figure 5.13 shows a schematic of the measurement line the points were measured along, as well as the coordinate system used, with Figs. 5.14a, 5.15a and 5.16a showing the measured data, as well as the FEA predictions.

An opportunity arose some time after the initial experiment to carry out repeat measurements on the specimens, however this time using a ra-

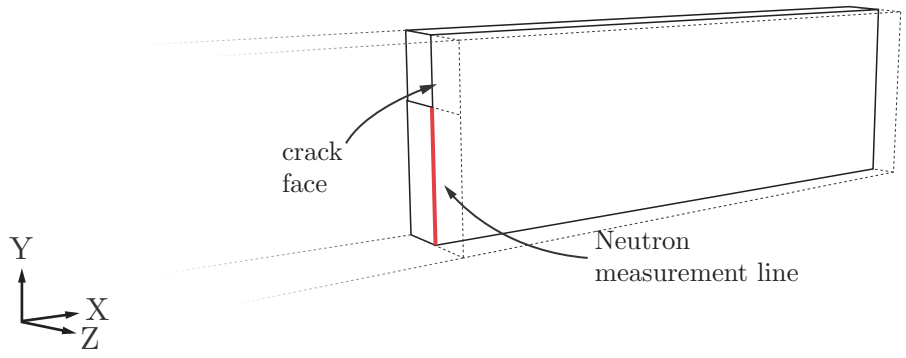

Figure 5.13: Schematic showing measurement lines

dial collimator. This radial collimator required the use of larger gauge volumes, this time 2 mm × 0.5 mm × 2 mm for the small beam, and 2 mm × 1 mm × 2 mm for the large beam, which combined with better shielding meant that significantly more measurement points would be possible, and which would supplement the initial measurements. This data is shown in Figs. 5.14a, 5.15a and 5.16a, also with FEA results for comparison.

As multiple measurements are presented here for the same specimens, the discussion of these results has been split into a number of sections. Each component of stress, namely σ_{xx}, σ_{yy} and σ_{zz} is considered separately:

- For each component of stress, the measurements from the slit and radial collimators are compared with each other, highlighting any differences between the two systems.
- Finally the neutron diffraction measurements are compared to the finite element predictions, with discrepancies between the measurements and the predictions discussed.

5.3.3 Managing inherent neutron diffraction measurement errors

An important point to consider before evaluating the data, is how to take into account the errors associated with neutron diffraction. As explained briefly in Section 4.4.3, the data obtained from neutron diffraction is initially in the form of scattering angles, which are then converted into lattice spacings using Bragg's law. These do not manifest themselves as single values however, but rather as distributions of diffraction angles, which then have Gaussian curves fitted and the peaks identified. These peaks are fitted using software developed at E3, SteCa, which was specifically designed for

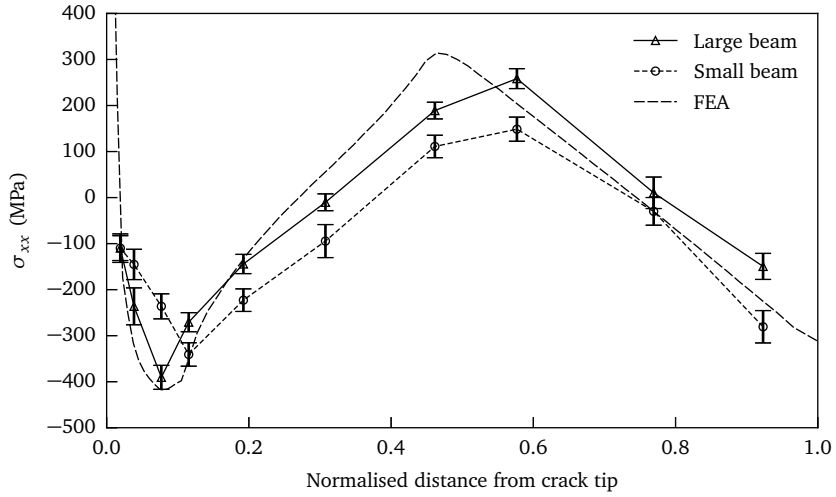

(a) σ_{xx} neutron diffraction measurements using slit system

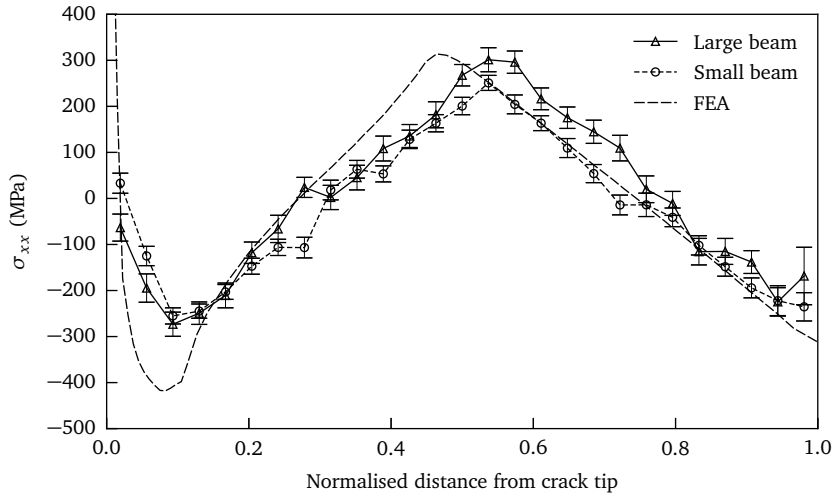

(b) σ_{xx} neutron diffraction measurements using radial collimator

Figure 5.14: Neutron diffraction σ_{xx} stress measurements and a comparison with the finite element predictions

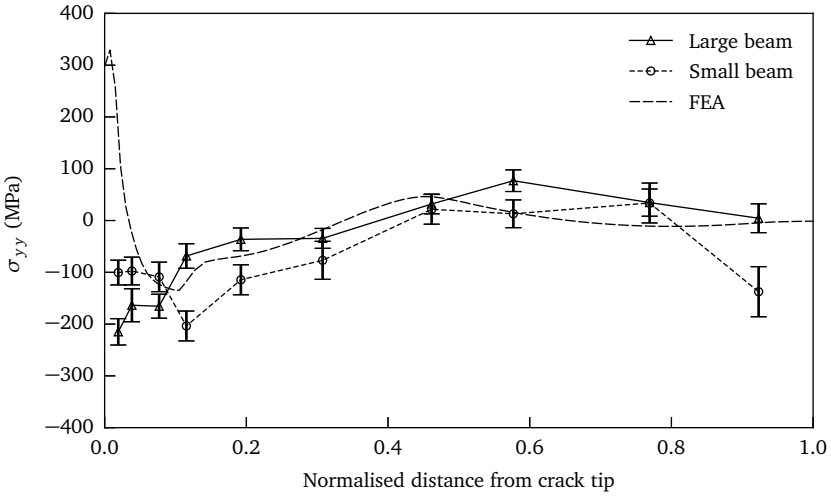

(a) σ_{yy} neutron diffraction measurements using slit system

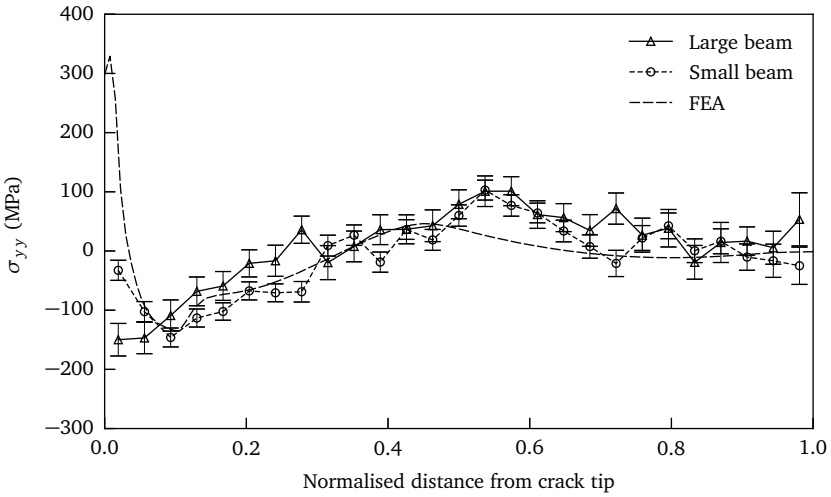

(b) σ_{yy} neutron diffraction measurements using radial collimator

Figure 5.15: Neutron diffraction σ_{yy} stress measurements and a comparison with the finite element predictions

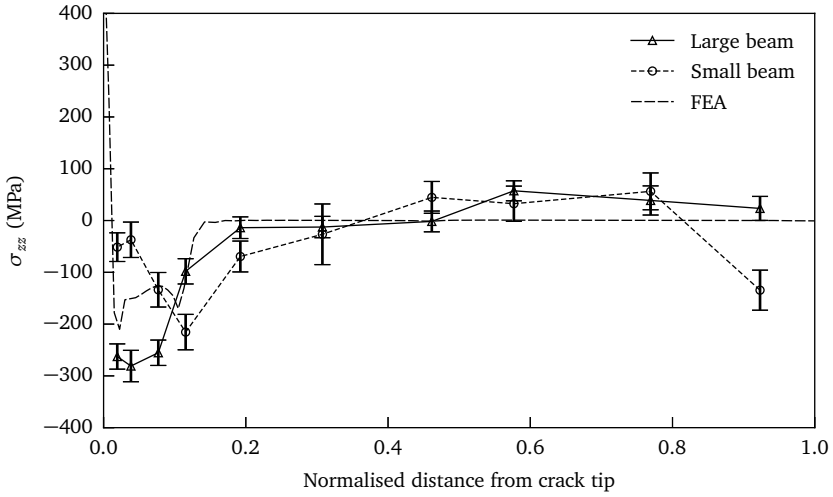

(a) σ_{zz} neutron diffraction measurements using slit system

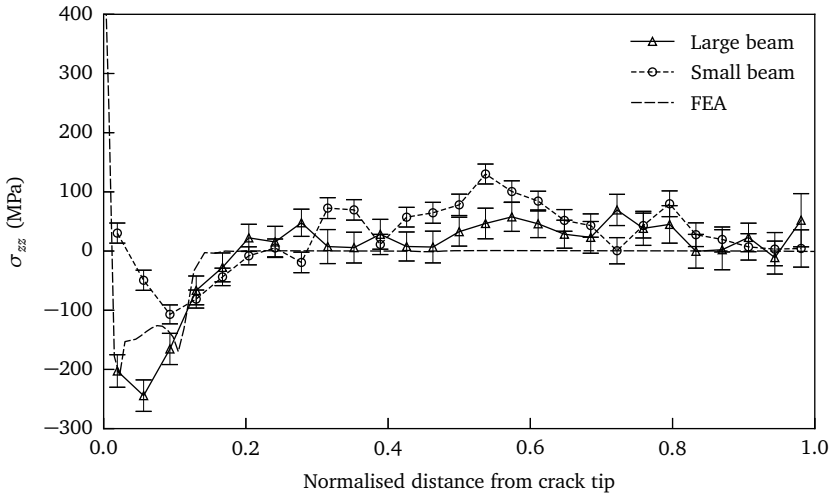

(b) σ_{zz} neutron diffraction measurements using radial collimator

Figure 5.16: Neutron diffraction σ_{zz} stress measurements and a comparison with the finite element predictions

the purpose of peak profile analysis, background correction and peak fitting (Randau et al., 2011). Fitting these curves results in an associated error for the scattering angles, given by $\delta\theta$, which can then be used to estimate the total error using Eq. (4.10)(Wimpory et al., 2009). If we start by rewriting the equation for strain using the scattering angles, we get

$$\varepsilon = \frac{\sin(\theta_0)}{\sin(\theta)} - 1 \tag{5.12}$$

By then taking the partial derivative, and then the root mean square, an estimate for the uncertainty is then given by:

$$e_\varepsilon = \sqrt{\left(\frac{\cos\theta_0}{\sin\theta}\delta\theta_0\right)^2 + \left(\frac{\cos\theta\sin\theta_0}{\sin^2\theta}\delta\theta\right)^2}. \tag{5.13}$$

This can then be further simplified by using the approximation that $\theta \approx \theta_0$, and so reducing the equation to:

$$e_\varepsilon = \cot(\theta_0)\sqrt{(\delta\theta_0)^2 + (\delta\theta)^2}, \tag{5.14}$$

which can then be used to estimate the peak fitting strain errors.

In addition to the peak fitting errors, there are other sources of random error (e.g. electrical noise in the detector, temperature fluctuations and counting statistics), and systematic error (beam misalignment, gauge volume shape and absorption effects) that will also contribute to the overall error, however these are harder to quantify. As mentioned early on, in Section 2.2, as well as the global macro stress field, which has so far been the focus, there also exist more localised type II and III stresses, which occur at the granular and molecular level, and which also have an effect on the measured stress field (Daymond and Priesmeyer, 2002). It is generally assumed that the size of the gauge volume and magnitude of the macro stresses negate these effects, however for specimens containing large grains, or non uniformly distributed grains, these effects must also be considered. The error bars included in Fig. 5.14a to Fig. 5.16b take into account the peak fitting errors and were calculated using Eq. (5.14).

The effect of gauge volume size and shape

Another point worth considering before analysing the data is the effect that the different shaped gauge volumes used in these measurements may have had. When carrying out neutron diffraction measurements, the results produced are not for a single point, but rather for the entire gauge volume, and so the results are approximately an average of the stresses in that volume (Price et al., 2008). For this reason, it is important to consider the effect of

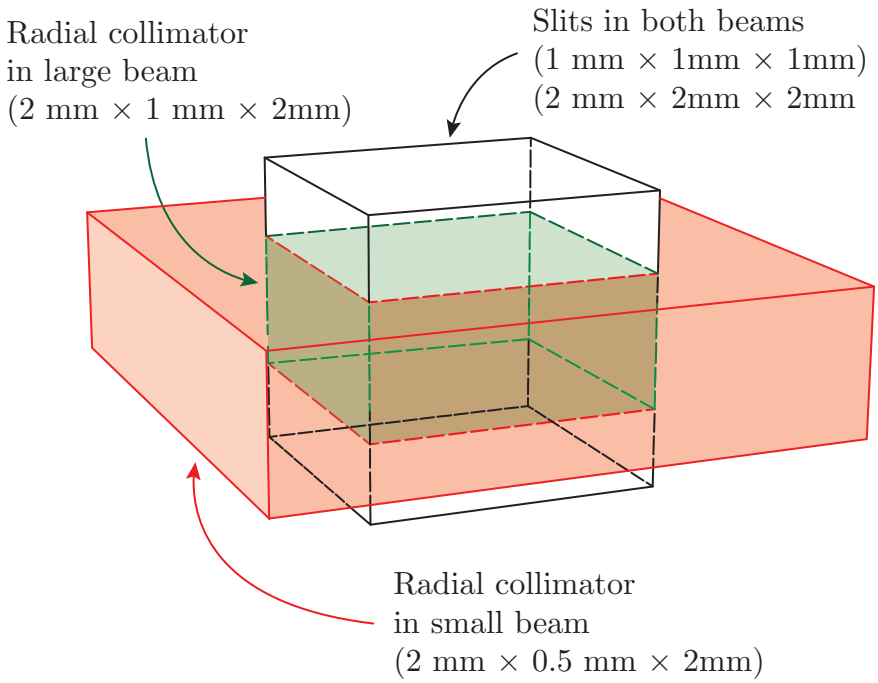

Figure 5.17: Comparing the relative size of the gauge volumes, when normalised using the scale factor λ

the relative size of the gauge volumes with respect to the beams, and ultimately the stress fields. Figure 5.17 shows the relative size of the gauge volumes, when normalised using the scale factor λ, highlighting the differences in size and shape between some of the measurements, and whose differences should be taken into account when considering the data.

The effect of the finite size of the gauge volume is particularly important immediately ahead of the crack tip; this is discussed in more detail in the individual examinations of the results, however in brief, this is the area typically associated with the highest strain gradients, and consequently the effect of averaging over a finite area becomes more pronounced.

5.3.4 An examination of the σ_{xx} measurements

Comparing the measurements from the slit and radial collimators

The first thing of note when comparing the data in Figs. 5.14a and 5.14b is that both sets of measured results agreed very well, showing virtually the same stress distribution.

One of the main features of the stress distribution, the peak tensile stress in the centre, matched both in terms of the location of the peaks, and approximately similar magnitudes. The smaller beam did show slightly lower magnitude stresses using the slits than when measured with the radial collimator (in the order of 100 MPa lower), however the error bars were also

larger. Measuring peaks in stresses using large gauge volumes can cause averaging errors that may not be present when measuring a simple stress gradient, and could have accounted for this discrepancy, however the gauge volumes when using the slit collimators were scaled proportionally, and so an error of this nature would be expected to be expected to be found in both large and small beams using the slits.

Another slight difference between the two type of collimators was in the stresses predicted directly ahead of the crack tip, where they both predicted a peak in compressive stresses, but of different magnitudes. The slit measurements predicted a peak of between approximately 350 MPa and 400 MPa, whereas the radial collimator measurements predicted between 250 MPa and 280 MPa. The difference is relatively small, especially when the error margins are taken into account, however this discrepancy in particular may be attributable the differences in gauge volume size and shape. Figure 5.18a shows the stresses directly ahead of the crack tip, and we can see that as you move away from the tip, the stresses in the Y direction become more uniform, but that close to the crack tip there are large stress gradients in both directions. Whilst this should not cause there to be any difference between the large and small beam slit measurements, as their gauge volumes were proportionally the same, this could explain their discrepancies with the radial measurements, as the gauge volumes would have been averaging over a different area of large stress gradients.

Comparing the neutron diffraction measurements with the finite element analyses

As well as both sets of measurements agreeing well with each other, both sets of measurements also showed excellent agreement with the finite element predictions, for both stress distributions and magnitudes.

As previously mentioned, there was some variation in the magnitude predicted for the peak tensile stresses; the radial collimator measurements agreed with the finite element prediction very well, however the slit measurement for the small beam disagreed with the finite element prediction by approximately 200 MPa.

Another notable difference between the measurements and the predictions is the location of the peak stresses, with the finite element analysis placing the peak at approximately 0.45 of the way along the normalised uncracked ligament, and the measurements all agreeing that it is approximately 0.55 of the way along. A potential cause for this could have been an error in the transformation of the coordinate systems used in the initial measurements, however given how the rest of the distribution lines up so well, this seems unlikely.

Finally, the stresses ahead of the crack tip do not quite agree between the measurements and the prediction. As discussed earlier, classical frac-

ture mechanics theory predicts infinite stresses at the tip, characterised here in the finite element analysis by extremely large magnitude stresses directly ahead of the tip, with a steep stress gradient, becoming compressive immediately after. The measurements were able to detect this compressive peak, but not the tensile stress. As discussed however, the measurements are an average of the stresses over the whole of the gauge volume, and the stress gradients at this point are so large, not just in the Y direction, but also the X direction (as shown in Fig. 5.18a), that these would have been very difficult to measure.

5.3.5 An examination of the σ_{yy} measurements

Comparing the measurements from the slit and radial collimators

As with the σ_{xx} measurements, the two different collimator measurements matched quite closely both in terms of stress distribution, and stress magnitudes. An exception to this however was in the slit measurement for the small beam, which predicted a compressive stress of approximately -150 MPa at the beam surface. The error margins here were quite large, in the order of 60 MPa, however even taking that into account, the slits still measured a compressive stress not visible using the radial collimator.

One explanation considered was the possibility that the milling processed using in the manufacture of the specimens may have introduced compressive surface stresses, which were being picked up in the measurement. By assuming that these stresses would be present in both size specimens up to an absolute depth, rather than a proportional one based on the scale factor, then this could explain why only the smaller gauge volume used in the smaller beam was able to detect it. An experiment carried out by Denkena and De Leon (2008) on the same aluminium alloy used for these experiments (though not necessarily the same heat treatment) found that compressive stresses of the same order of magnitude were introduced when milled, however they peaked at approximately 50 µm to 100 µm below the surface, and had reduced to 0 MPa by 250 µm, making it unlikely that they would be visible to this degree in these measurements.

Comparing the neutron diffraction measurements with the finite element analyses

Similarly to with the σ_{xx} stresses, the neutron diffraction measurements both matched the finite element prediction closely, with the exception of at the crack tip, the previously mentioned compressive surface stress in the small beam, and again a slight shift in the location of the peak tensile stress in the centre of the beam.

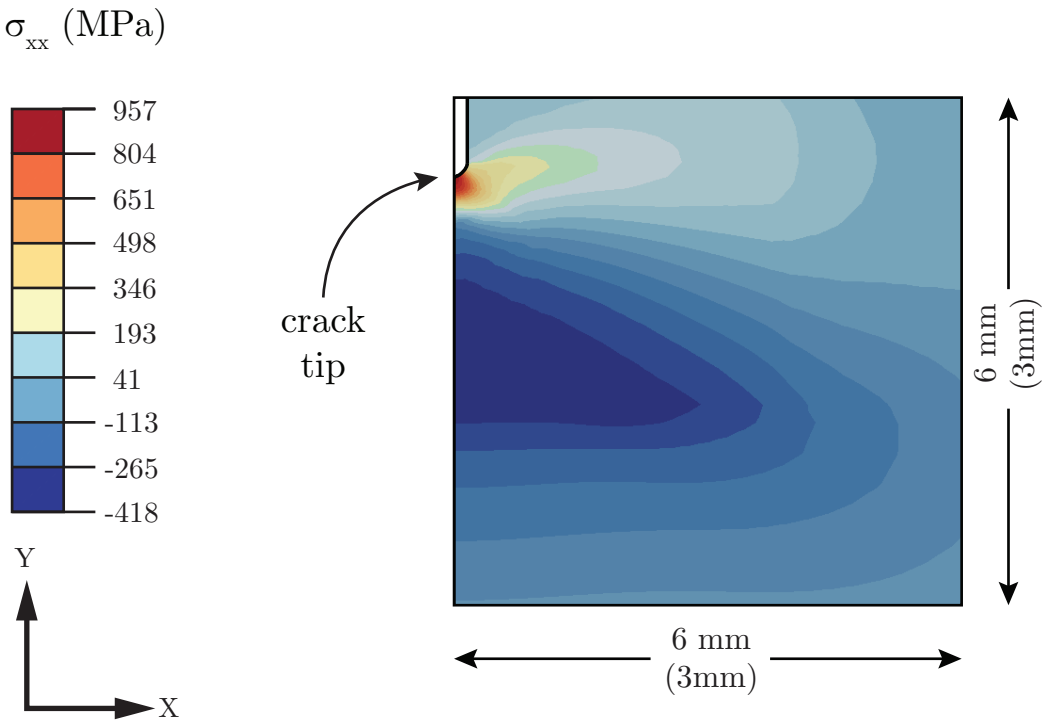

(a) σ_{xx} in the area close to the crack tip

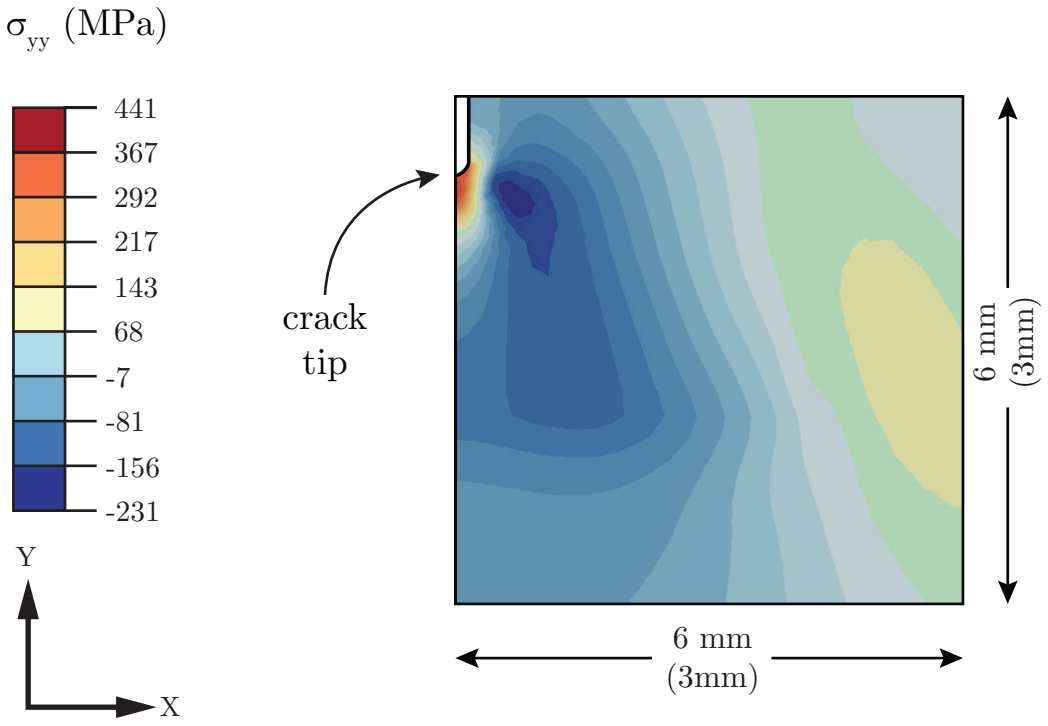

(b) σ_{yy} in the area close to the crack tip

Figure 5.18: Showing how the stress varies in the XY Plane for the σ_{xx} and σ_{yy} components near the crack tip

Again, a very large stress gradient is predicted by the finite element analysis directly ahead of the crack tip, which the measurements did not pick up. As discussed for the σ_{xx} measurements however, such a large stress gradient would be very difficult to pick up using the size gauge volumes that were possible with this instrument.

The discrepancy between the predicted location of the tensile peak and the measured peak was similar to that in the previous measurement, with the prediction and measurements occurring at approximately 0.45 and 0.55 of the way across the normalised uncracked section respectively. This is particularly clear for the radial collimator measurements where the error bars are smaller and the larger number of measurement points means the peak is better defined.

5.3.6 An examination of the σ_{zz} measurements

Comparing the measurements from the slit and radial collimators

The measurements for the final stress component once again very much agreed with each other, with the notable exception again of a large compressive stress measured on the small beam using the slit system, which was not present at all using the radial collimator. These different measurements consist of a series of 2-3 points, rather than a single measurement point, which instils more confidence in them being correct.

Aside from this discrepancy, the two collimator systems produced very similar measurements, even around the crack tip where significantly larger compressive stresses are detected for the large beam, using both systems.

Comparing the neutron diffraction measurements with the finite element analyses

Finally, when comparing these neutron diffraction measurements to the predictions we see a relatively good agreement, with the exception again of the compressive surface stress in the small beam. Apart from at the tip, the majority of the uncracked ligament is essentially predicted to be stress free, and while the measurements predict some tensile stresses across this section, they are in the order of only 50 MPa, with error bars across a similar range.

5.4 Summary

This chapter has described the results obtained from the two sets of experiments carried out, highlighting and discussing points of interest. The main conclusions that can be drawn are discussed in Chapter 7, however a brief

summary of the points of interest and questions the experiments brought up are presented here.

- The loads to failure for the two different sized specimens, when fitted to a Weibull distribution, produced the scaled failure loads predicted in Chapter 3, and ultimately the same value of K_0, though the scatter in the results for the smaller specimens was significantly higher than for the large specimens however.

- Using a failure assessment diagram, which is simply a visual representation of the ratios of elastic and elastic-plastic J-integral, it was shown that while this scaling was expected to apply using this scale factor, there would come a realistic point at which would stop being the case.

- Two scaled aluminium beams, similar in geometry to the previous fracture tests, were plastically deformed so as to theoretically introduce the same residual stress distribution into both beams, using the scaling law again found in Chapter 3. The load-displacement responses matched the finite element predictions, and importantly, each other, indicating that the same residual stress fields had been introduced.

- The residual stress fields in both beams were then measured using neutron diffraction, twice, once using a slit collimator, and once using a radial collimator. The slit collimator utilised scaled gauge volumes, whereas the radial collimator was unable to accommodate this and so the gauge volumes were not geometrically similar. The measurements mostly agreed very well with the finite element predictions, with the exception of a compressive stress stress detected in the small beam in the σ_{yy} and σzz components, in the order of -150 MPa. This was only detected using the slit collimator, and was not predicted in the simulations, leading to the conclusion that they were erroneous results, or a result of machining processes, with the different gauge volume shapes being the reason for only detecting them in one of the measurements.

- Finally, a discrepancy between the small and large beams was noted at the crack tip, with the σ_{zz} stresses being in the order of 200 MPa larger for the large beam than the small beam. This was neither predicted by model, nor explainable using the different gauge volume geometries, as it was consistent across both measurement systems.

Chapter 6

Complex case study

6.1 Introduction

Prior to going into a more detailed discussion in Chapter 7 about the results and findings from the work already described, this chapter first considers a theoretical case study, the aim of which was to provide context and grounding for the work described so far in this thesis. This case study provides a more complex example than the simple specimens and loading regimes described thus far, and extends the concept of scaling to a genuine problem. The case study focuses on an experiment that was carried out using a real component, and aims to design a scaled down version that reproduces the features and results of the original, potentially allowing for a more practical and cost effective version of the experiment. The complex nature of the geometry and loading, as well as the desired outcome which was to replicate failure, meant that non geometric scaling is examined here in order to produce the desired results (Coules et al., 2017a,b).

This project, which will be described in more detail in Section 6.2, was run by the Health and Safety Executive and the European Commission Joint Research Centre, and was carried out by a collaboration of organisations, collectively known as the Network for Evaluation of Structural Components, with the project consequently known as the NESC-I project. Its aim was to investigate the effects of pressurised thermal shock on fracture (Bass et al., 2001).

The case study considered the experiment carried out in the NESC-I project, which consisted of a heated 6800 kg cylinder rotated at high speed before being quenched, and looked at whether it was possible to replicate the fracture conditions using a much smaller geometry. The potential for scaling down here is obvious, as the 6800 kg specimen was both cumbersome, and expensive, and so the potential to carry out similar experiments in the future at a smaller scale is an attractive one.

This chapter is structured as follows:

- First, the original work carried out during the NESC-I project is described in Section 6.2.
- The initial finite element models that were generated for the case study are then described in Section 6.3, with a comparison to the original NESC-I project and explanation of the calibration used.
- A description of the types of scaling and the imposed constraints that were used is then given in Section 6.4, with an explanation of how the models were then generated. Following this, the results from the parametric models are then explained.
- Finally, a brief discussion about the results then follows in Section 6.5.

The work described in this chapter was carried out in collaboration with Dr. Harry Coules. The division of work was such that the majority of the mechanical modelling was carried out by Dr. Coules, and the thermal modelling by the author. The choice of parameters was a joint effort, along with the scripting required to ensure the results from the thermal models could be applied to mechanical models, using the uncoupled approach. The conclusions drawn from the work and discussed here are the author's own.

6.2 NESC-I overview

The original NESC-I project was deigned to investigate the effect of pressured thermal shock (PTS), which might occur in a nuclear rector pressure vessel (RPV) due a rapid decrease in temperature resulting from a coolant leak, and which would result in rapidly changing thermal gradients. The combination of loading from the internal pressurisation and the thermally induced stresses as a result of the thermal shock are not trivial to calculate, yet it is important to know the effects these stresses will have on the flaws that are an unavoidable feature of reactors (Maddox, 1974). These defects of the result of a multitude of different mechanisms at work during welding, which involve large temperature gradients, varied cooling rates, different coefficients of thermal expansion, and complex fluid dynamics (Mendez and Eagar, 2003).

Due to being subjected to a large amount of neutron bombardment, the inner surface of the RPV also suffers from radiation embrittlement, characterised by a substantial reduction in the fracture toughness of a material (Odette and Lucas, 2001), meaning that the stress intensity factors produced in the RPV as a result of the thermal gradients can be sufficient to result in catastrophic failure of the reactor. It is therefore important to be able to assess the effect that that the combined loads will have on the materials and flaws involved, which was the purpose of the NESC-I project.

Rather than producing an actual pressurised vessel, it was deemed more practical to create a mock-up, consisting of a 6800 kg hollow cylinder, which was heated to 290 °C and rotated at 2100 rpm, in order to simulate the internal pressure temperature conditions of an RPV. The cylinder was made from an ASTM A 508 Class 3 steel, and clad with an austenitic steel, which along with its dimensions were designed to replicate the features of a typical pressurised water reactor (PWR). Figure 6.1, reproduced from Bass et al. (2001), shows the dimensions and main features of the original experiment, reproduced from a figure in the original NESC-I report (Bass et al., 2001).

A number of defects were manually introduced into the cylinder, representing the type of flaws typically found and which were of interest under these conditions. The cylinder was then quenched by spraying 5 °C water on the inner surface, with strain gauges and thermocouples used to monitor its response throughout. Finally, the fracture sites were investigated using a number of destructive techniques to assess the effects of the PTS, with the results analysed in a round-robin study.

The experiment was very well characterised, with the amount of data captured before, and during the experiment, meaning that detailed finite element models were able to be produced in order to understand the dynamically observed events. The data also meant that subsequent studies, such as this one, were able to be undertaken using well defined material and physical properties, and operate with a high degree of confidence in their models due to the experimental validation available.

6.3 The initial models

The aim of this case study was to produce the same crack loading conditions in a scaled down model as in the original size used in the NESC-I project. A total of 18 cracks and notches were manually introduced into the original component and subsequently studied, however for the purposes of this case study only one was required; a notch known as “defect R” was used, which consisted of a 208 mm long and 74 mm deep, semi circular EDM notch which was then fatigue sharpened. Upon completion of the experiment, it was destructively evaluated, and found to have grown by a further 16.5 mm during the quench, initially by a small amount of ductile tearing before undergoing cleavage fracture.

All the simulations carried out in this section utilised an uncoupled thermal-mechanical approach, meaning that a thermal model was first run, the results of which were then used to inform a mechanical model. Early on in the NESC-I project, a material characterisation project had been carried out, and so the temperature dependent thermal and mechanical material properties were all readily available for use in subsequent models, and are shown in Table 6.1. This table contains two sets of material properties, one

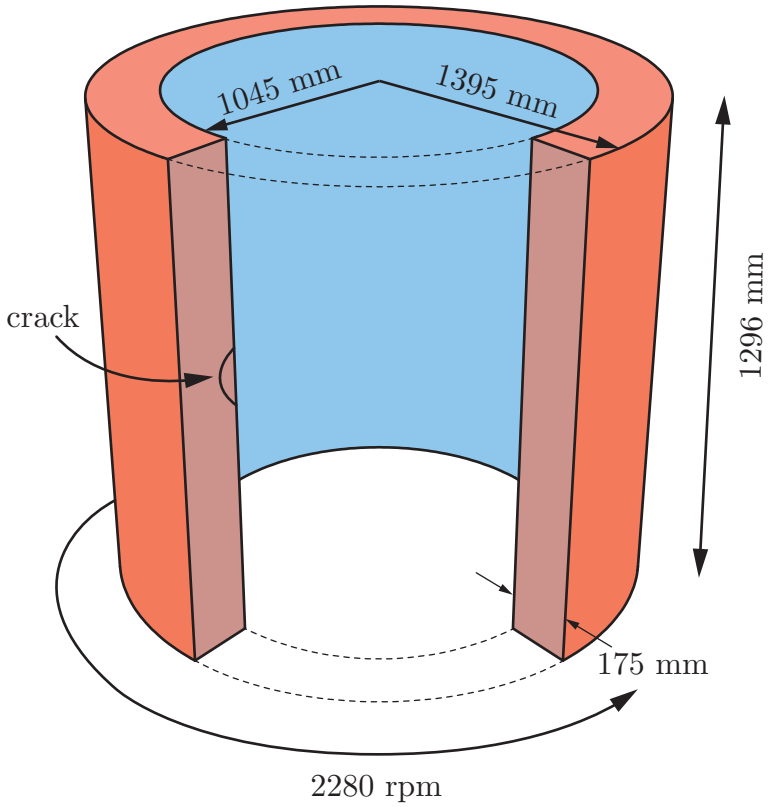

Figure 6.1: Schematic showing a cutaway of the original NESC-I experimental set-up, reproduced from Bass et al. (2001)

for the base material and heat affected zone (HAZ), and another for the inner cladding layer.

The material properties in Table 6.1 are mostly temperature dependent, and so it was expected that the mechanical model would be heavily dependent on the results of the thermal model. It was assumed however that the thermal properties of the material, and consequently the results of the thermal model, whilst themselves also temperature dependent, would be entirely independent of stress, and therefore that the dependence relationship would only go one way. There are certainly cases where this assumption does not hold true (Silva et al., 2004), however in this example the temperatures were kept relatively low and there were no phase transformations to consider, justifying the use of this assumption.

Table 6.1: Material properties as a function of temperature, where T denotes the temperature in °C, reproduced from Bass et al. (2001)

Property			Base/HAZ	Cladding
Young's modulus,	(GPa)	E	$211.7 - 0.0628T$	$150.2 - 0.0862T$
Poison's ratio,		ν	0.28	0.28
Thermal conductivity,	(W/m°C)	κ	$40.6 - 0.0097T$	$13.9 + 0.018T$
Specific heat capacity,	(kJ/kg°C)	c_p	$0.432 + 4.1 \times 10^{-4}T$	$0.432 + 4.1 \times 10^{-4}T$
Coefficient of thermal expansion,	(µm/m°C)	α	$11.6 + 0.014T$	$15.7 + 0.0096T$
Density,	(kg/m^3)	ρ	7800 (20 °C)	7720 (20 °C)
			7720 (290 °C)	7610 (290 °C)

6.3.1 NESCI-I specimen geometry

6.3.2 Thermal model

The first step in modelling the initial experiment was producing a thermal model that accurately predicted the temperature response of the cylinder. The period of interest was the quench of the cylinder; the heating up of the cylinder was not modelled, as this was carried out gradually, three days prior to the quench, so as to cause minimal thermal gradients. Consequently, the simulations began with the model at a uniform 290 °C.

The quench was simulated by applying a surface film condition, specifying the sink temperature (5 °C) and the heat transfer coefficient between the water and the inner surface. A range of heat transfer coefficients, 9 kW/m^2°C to 15 kW/m^2°C, were provided in the NESC-I report, and so a series of models were run in order to select the most appropriate value. The outer surface of the cylinder was insulated during the experiment to prevent any major heat loss, and so no heat transfer was specified for this surface, and likewise for the top and bottom surfaces of the cylinder.

The crack itself was not modelled in the thermal simulations, as it was assumed that it would not have any bearing on the temperature field due to using the same material properties as the bulk of the cylinder. With this in mind, along with the described boundary conditions, the thermal transfer was expected to be an axisymmetric problem, however the need to later apply the results to the mechanical model containing the crack, meant it could not be modelled as such. The final simulations instead took advantage of the cylinder's symmetry, only modelling a quarter of the specimen to save on computation time. Although the entire temperature field was needed for the subsequent mechanical models, in order to compare the results with the experimental NESC-I values, temperatures at the locations where thermocouples had been present were needed. These thermocouple locations are shown in Fig. 6.2, and used in the comparison that follows.

Figure 6.3a shows the initial mesh and boundary conditions for this simulation. The model was split into base/HAZ material, and cladding mate-

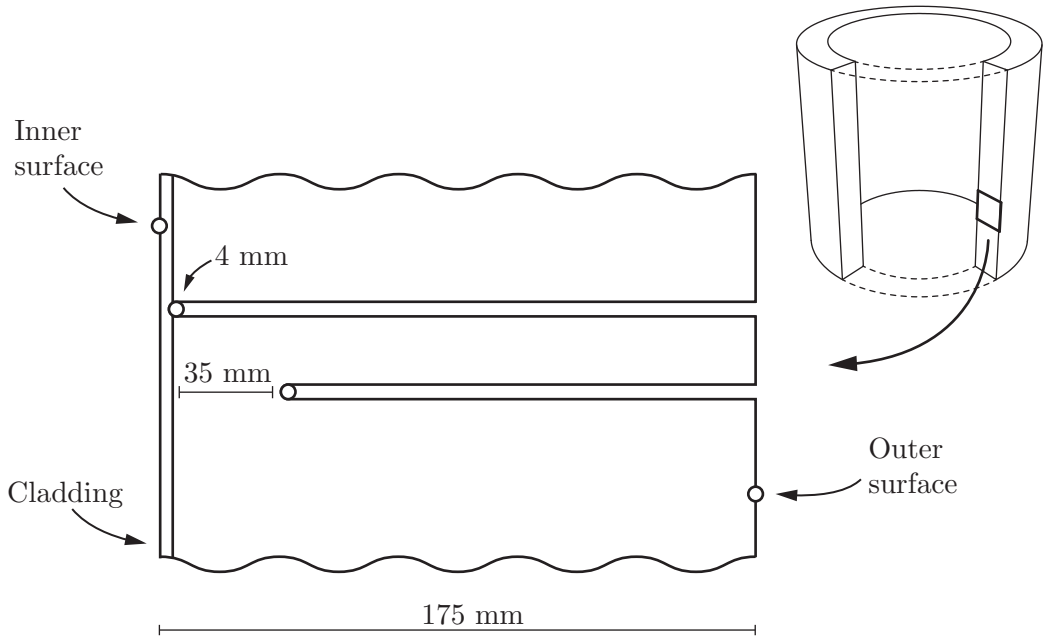

Figure 6.2: Schematic showing the location of the thermocouple measurements, with respect to the inner surface

rial, with a total of approximately 63 000 8-noded DC3D8 linear hexahedral heat transfer elements used. The simulations were then run using the range of heat transfer coefficients, and the results compared with temperatures at the thermocouple location. It transpired that varying the heat transfer coefficient did not significantly alter the temperature distributions. There was good agreement between the both sets of simulations, and the experimentally measured temperatures, as can be seen in Fig. 6.4. The results using $9\,kW/m^2{}^\circ C$ as the heat transfer coefficient produced the closest fit overall, however, and so were used for all subsequent analyses.

The temperature distribution using this value for the various thermocouple locations is shown in Fig. 6.5, along with the through thickness temperature distribution at the centre of the cylinder after 300 s. The results from the finite element simulations show a very good agreement with those obtained in the original NESC-I project, providing confidence in the model for use in the mechanical simulations, and in the modelling approach as a whole for use in further scaled models.

Given the number of models that were to be run in the later parametric study, and the length of time the mechanical models would have to run for, it was important to minimise the runtime of the thermal models, with an obvious method of achieving this being a reduction in the number of elements used in the mesh. A convergence study was carried out to ascertain the dependence of the temperature field on the mesh coarseness, with the number of elements being reduced in the radial and axial directions; The simula-

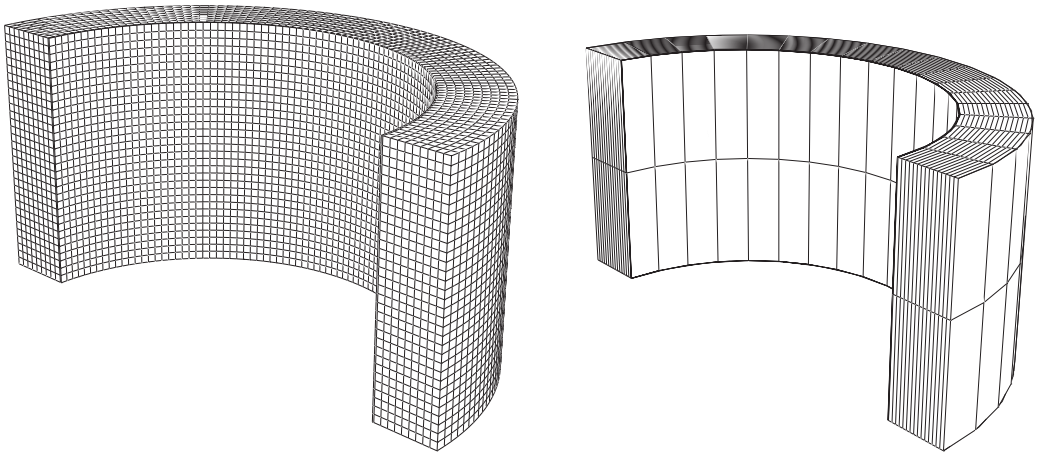

(a) Fine thermal model mesh (b) Coarse thermal model mesh

Figure 6.3: The meshes used in the initial temperature models

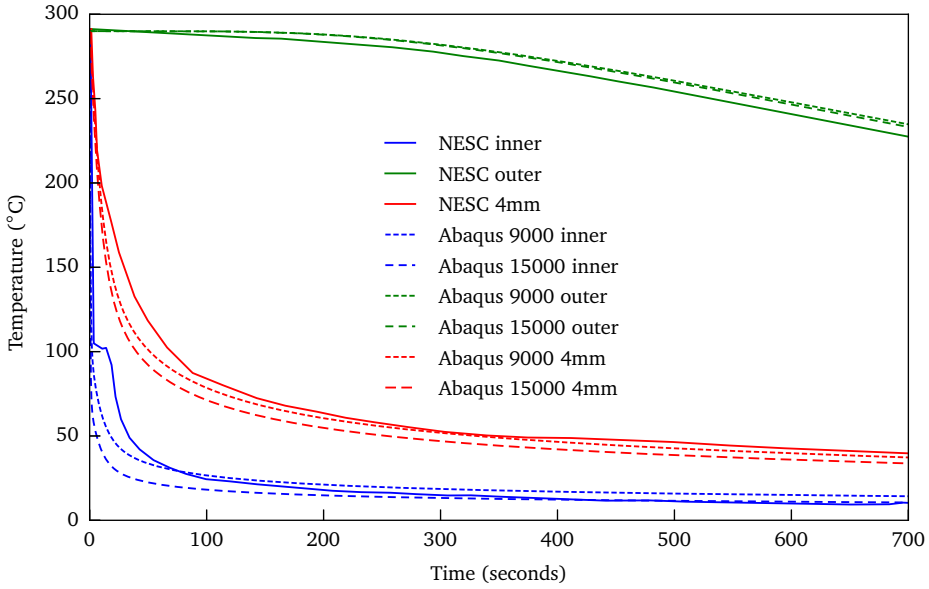

Figure 6.4: Comparison of the finite element thermal models with the NESC-I values, using the full range of heat transfer coefficients

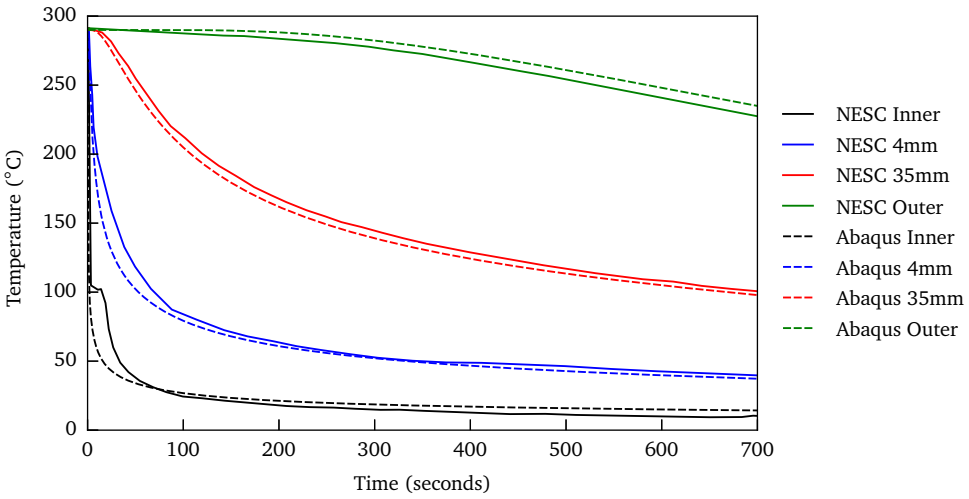

Figure 6.5: A comparison of the finite element predictions and measured temperature profiles in the original NESC-I quench test at various depths

tion did not use an axisymmetric model, however, the applied boundary conditions meant that the results did not vary circumferentially, and so no sensitivity study was carried out on the effect of the number of elements in the circumferential direction. The results showed that using fewer than six elements in the radial direction produced a discernable difference in the temperature field, and that as expected, the number of elements in the axial direction had no discernable effect on the results, as the temperature distributions were almost one-dimensional. The final mesh used for this initial thermal study, consisting of approximately 700 DC3D8 elements, and whose results were then used in the mechanical model, is shown in Fig. 6.3b.

6.3.3 Mechanical centrifugal loading models

Validation of mechanical modelling techniques

A more complex mesh was needed to account for the crack used in the mechanical model, and so simulations were first carried out to validate this new mesh, along with the boundary conditions and applied load, by comparing the model results to existing analytical solutions for both the stress field and stress intensity factors. The new mesh consisted, for the most part, of 8-noded C3D8R quadratic tetrahedral elements, however as the area around the crack was the focus of the investigation, a refined mesh consisting of 10-noded quadratic C3D10 elements were used so as to produce a more detailed stress field in this area, along with more accurate J-integral results, giving a total of approximately 24 000 elements. The global mesh and the refined crack tip mesh are shown in Fig. 6.6.

The results of the thermal model were to be overlaid on top of the mechanical model, and so the question of arose of whether the two meshes were required to be similar. This may have been the case, or at the very least have required a more refined mesh in the thermal model, if the temperature field had been a complex one. Looking at Fig. 6.5, however, we can see that it is a relatively simple temperature field, and so acceptable to allow ABAQUS to interpolate the results to fit the new mesh.

The 2100 rpm rotation was simulated using a rotational body force, defined as a rotation of 219.91 rad s^{-1} which was ramped up linearly from rest over the course of the step. The crack itself was defined by not including the symmetry boundary conditions that constrained the remaining faces.

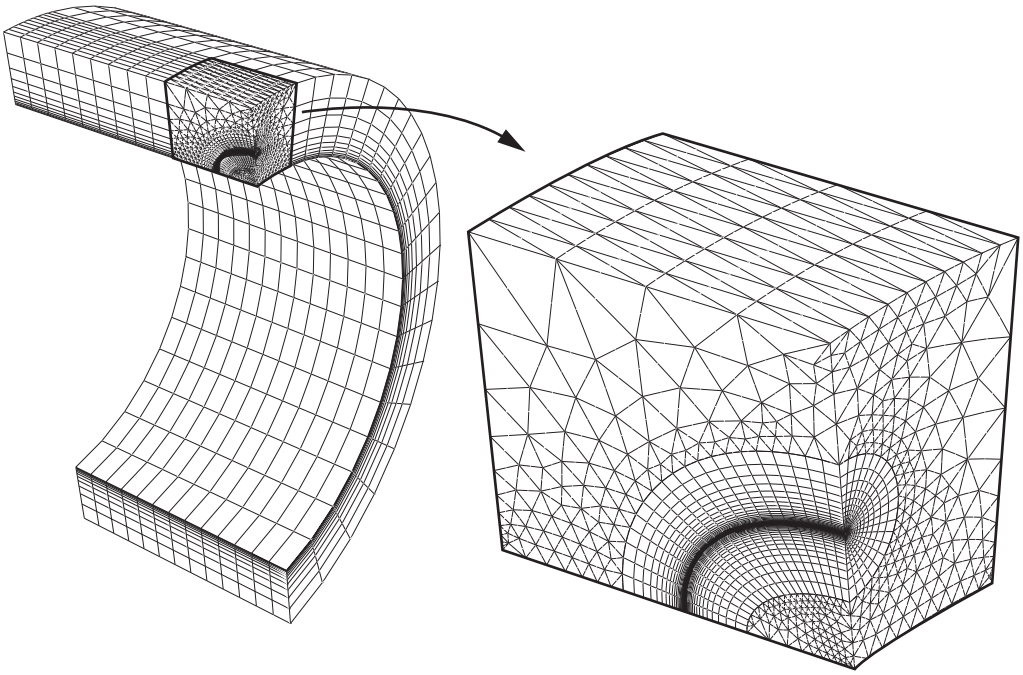

Figure 6.6: The mesh used in the initial elastic and elastic-plastic analyses, showing the refined mesh around the crack tip

The stresses produced by the model were first compared to the analytical solutions using an uncracked elastic analysis, where the same mesh was used, but the effect of the crack removed by applying the appropriate boundary conditions, so as to simulate an uncracked spinning cylinder. The results were then compared to the radial and hoop stresses, σ_{rr} and $\sigma_{\theta\theta}$,

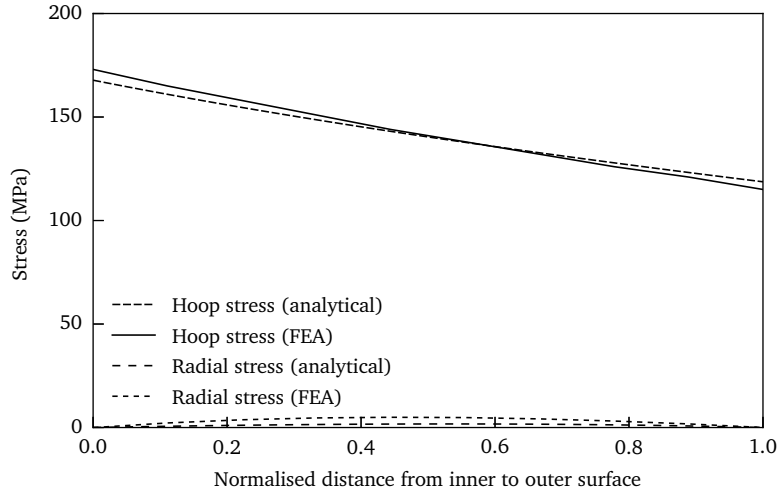

Figure 6.7: Analytical and finite element predictions of the elastic through wall stresses for the spinning cylinder

calculated using Eqs. (6.1) and (6.2) (Hearn, 1997)

$$\sigma_{rr} = \left(3 + \frac{\nu}{1+\nu}\right) \frac{\rho\omega^2}{8} \left[R_i^2 + R_o^2 - \frac{R_i^2 R_o^2}{r^2} - r^2\right] \tag{6.1}$$

$$\sigma_{\theta\theta} = \frac{\rho\omega^2}{8} \left[\left(3 + \frac{\nu}{1+\nu}\right)\left(R_i^2 + R_o^2 - \frac{R_i^2 R_o^2}{r^2} - r^2\right) - \left(1 + \frac{3\nu}{1+\nu}\right) r^2\right], \tag{6.2}$$

where ν is the Poisson's ratio, ρ the material density, ω the angular velocity, R_i and R_o the inner and outer radii, and r the radial position through the wall.

A constant value of $7800\,\mathrm{kg/m^3}$ was used for the density in Eqs. (6.1) and (6.2), despite the cladding being slightly less dense, for ease of calculation. The cladding density only differed by 1% and made up a very small part of the overall mass, so was considered an appropriate approximation for these verification calculations. The models themselves used the relevant densities and material properties.

A comparison of the through wall stresses is shown in Fig. 6.7, which shows good agreement between the two methods. The largest discrepancy between the analytical and finite element stress predictions is only of 4 MPa, which can be explained by the fact that the analytical solutions do not consider the height of the cylinder, whereas the finite element solution does. This gave confidence in the meshing and modelling methods, allowing them to be used in the subsequent cracked body analyses, which were tested next.

The cracked body models were identical to the previous uncracked elastic models, with the addition of the crack via the removal of the appropriate boundary conditions, allowed the crack face to separate and for the stress intensity factors along this crack front to be calculated. The material properties, mesh, remaining boundary conditions, applied loads and steps were all kept the same as before.

The examples considered so far in this work have consisted of a straight crack front, and so the stress intensity factors at the crack tips were relatively independent of position along the crack. In this example, however, the crack front was elliptical, and did not follow the geometry of the specimen, and consequently the stress intensity factor was dependent on position along the crack. In order to compare the results from the finite element models to the analytical solutions, two comparison points were chosen: the deepest point in the crack, and at the inner surface. The analytical solution for the the stress intensity factors for this geometry crack were given in the form of a weight function, calculated by Chapuliot (2000) for a number of different crack and cylinder geometries and orientations (given below in Eq. (6.3)).

Unlike the previous equations used for stress intensity factors, where the equations were dependent on how the geometries were loaded, the weight function method, developed by Bueckner (1970) and Rice (1972), instead relies on having the stress field already defined. While using weight functions involves this additional step of computing the stress field, this particular case would have been difficult to solve using the type of stress intensity factor equations discussed in Chapters 3 and 4 due to the more complex geometry and loading. As just shown however, calculating the stress field across the component due to the rotation and combination of materials was relatively straightforward, making the use of the weight function in this case a suitable alternative.

The stress intensity factors in this case were calculated using the generalised equation given by:

$$K_{\mathrm{I}} = \sqrt{\pi a}\left[\sigma_0 i_0 + \sigma_1 i_1\left(\frac{a}{t}\right) + \sigma_2 i_2\left(\frac{a}{t}\right)^2 + \sigma_3 i_3\left(\frac{a}{t}\right)^3\right], \tag{6.3}$$

where $\sigma_{0\ldots3}$ refer to coefficients of a third degree polynomial fitted to the hoop stress field, and $i_{0\ldots3}$ the weight function coefficients obtained from Chapuliot (2000). The polynomial coefficients were calculated using the stress distribution generated using Eq. (6.2) and shown in Fig. 6.7, which was first normalised against wall thickness, with the resulting coefficients being:

$$\begin{aligned}
\sigma_0 &= 6.6973 \times 10^8 \text{ Pa} \\
\sigma_1 &= -1.8308 \times 10^9 \text{ Pa} \\
\sigma_2 &= 2.1819 \times 10^9 \text{ Pa} \\
\sigma_3 &= -9.8896 \times 10^8 \text{ Pa}
\end{aligned}$$

The weight function coefficients, $i_{0\ldots3}$, were given in tables for a range of set ratios, (t/R_i), (a/c) and (a/t), however, none of them corresponded to the geometry of the NESC-I specimen. The author of the weight function accounted for this by recommending that barycentric interpolation[1] be carried out to find the desired values, using the generalised formula expressed by:

$$i^n(\alpha,\beta,\gamma) = \frac{1}{(\alpha_{x+1}-\alpha_x)(\beta_{y+1}-\beta_y)(\gamma_{z+1}-\gamma_z)} \begin{Bmatrix} (\alpha_{x+1}-\alpha)(\beta_{y+1}-\beta)(\gamma_{z+1}-\gamma)\, i^n_{x,y,z} + \\ (\alpha-\alpha_x)(\beta_{y+1}-\beta)(\gamma_{z+1}-\gamma)\, i^n_{x+1,y,z} + \\ \cdots \\ (\alpha-\alpha_x)(\beta-\beta_y)(\gamma-\gamma_z)\, i^n_{x+1,y+1,z+1} \end{Bmatrix}, \tag{6.4}$$

where α, β and γ refer to the ratios (t/R_i), (a/c) and (a/t), and the subscripts x, y, z and $x+1, y+1, z+1$ refer to the tabulated values directly below and above the required value. Using this method, the weight function values listed in Table 6.2 were calculated for the surface and deepest points.

Table 6.2: Interpolated weight function function values, calculated for use in Eq. (6.3)

Deepest point		Surface point	
$i_0 =$	0.8203	$i_0 =$	0.8263
$i_1 =$	0.5325	$i_1 =$	0.1535
$i_2 =$	0.4237	$i_2 =$	0.0608
$i_3 =$	0.3632	$i_3 =$	0.0326

The results of Eq. (6.3) using the calculated $\sigma_{0\ldots3}$ and $i_{0\ldots3}$ values produced stress intensity factors of 58.15 MPa$\sqrt{\text{m}}$ and 60.92 MPa$\sqrt{\text{m}}$ for the deepest point and surface point respectively, compared with 59.16 MPa$\sqrt{\text{m}}$ and 59.61 MPa$\sqrt{\text{m}}$ from the finite element analysis. The good agreement between the two sets of values, especially considering that the analytical values involved interpolated coefficients, added confidence to the modelling method used here to simulate the angular rotation of the specimen and the corresponding effect on the stress field and crack interaction.

Further confidence was added by plotting the K_J value against temperature at the failure point, along with the temperature dependent fracture toughness, shown in Fig. 6.8a, and seeing that they cross at approximately 70 °C, and at a K_J value of 280 MPa$\sqrt{\text{m}}$. Plotting the temperature at that point against time, shown in Fig. 6.8b, shows that it reaches 70 °C at approximately 204 s, corresponding with the time of failure in the original experiment.

[1] Barycentric interpolation is a form of Lagrange interpolation, essentially fitting a poly-

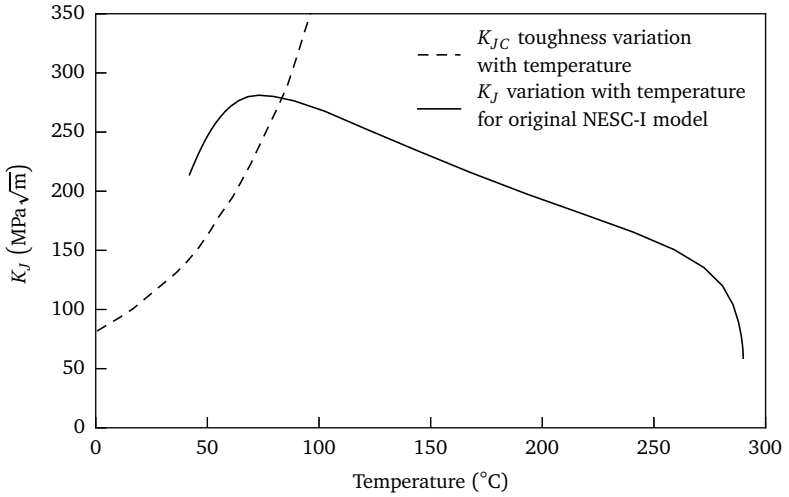

(a) The K_J value at the failure point, plotted against temperature at that point. Also showing the fracture toughness against temperature, and where they cross

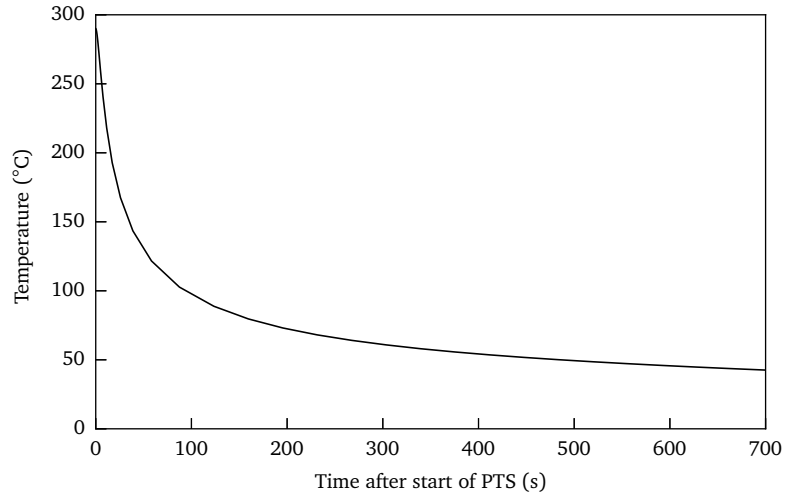

(b) The temperature value at the failure point, plotted against time from PTS

Figure 6.8: Finite element analysis of the original NESC-I experiment, predicting temperature and K_J values over the course of the PTS

6.4 Parametric study

6.4.1 The models

With the modelling methods validated, the focus of the case study shifted to producing a scaled model. The practical rationale behind this was that at 6800 kg, and rotating at 2100 rpm, the original NESC-I project was an extremely cumbersome and costly experiment to carry out, and so it would be advantageous to be able to carry out a scaled down version of the test, while still extracting the desired information.

As discussed in Chapter 3, and shown in Chapters 4 and 5, the results obtained from scaled specimens, even with appropriately scaled loads, are not simple to reproduce. The problem here was compounded with additional loading mechanisms, which though more representative of a real example, introduced further potential scaling laws.

In order to simply the problem, the results of interest from the original NESC-I project were first decided on, with the focus of the parametric study then being to reproduce these results in a scaled model, while applying certain restrictions on the scaling parameters to maintain a degree of practicality. The ultimate concern, and the main reason for the original NESC-I project, was the idea of the cylinder fracturing during the PTS, and so the conditions around the crack were chosen as the main scaling focus. The original NESC experiment found that there was a significant amount of plasticity at the crack tips, and therefore it was not appropriate to use K_{I}, which is only applicable during elastic fracture. In order to fully account for plasticity in these simulations, an elastic-plastic equivalent stress intensity factor, K_J, was used, describing the elastic-plastic crack driving force, and given by (Begley and Landes, 1972):

$$K_J = \sqrt{\frac{JE}{1-\nu^2}}. \tag{6.5}$$

The aim was therefore to achieve the same K_J value at a point along the crack front, thereby matching the failure criterion. Section 3.3 described how the J values vary as geometries are uniformly scaled, which combined with the complicated and interacting loading methods used here, meant it would be very difficult, if not impossible, to design a linearly scaled model that produced the same failure criterion. Instead, a range of parameters were chosen to be scaled and modelled, to investigate whether a similar method of failure was achievable in this way.

As the number of models was expected to be large, along with the number of points along the crack front, two specific points for investigation were chosen so as to make the results more manageable: the deepest point along

nomial to the available data.

the crack, and a point 14 mm in from the inner surface, which in reality corresponded to the approximate heat affected zone boundary, and the point at which fracture had been observed upon destructive testing at the end of the NESC-I project.

In order to decide what range of parameters should be used for the scaled models, a number of constraints were decided on and imposed:

- A minimum and maximum were decided upon for the inner and outer radii of the cylinder, so as to balance what seemed practical to produce the necessary crack driving force, with being sufficiently smaller than the original cylinder that it could be considered suitably scaled.

- A maximum angular velocity was set, beyond which the setup was considered to start becoming impractical.

- The starting temperature of the cylinder was capped as the available material data above this temperature was limited, but also because above this temperature the effects of microstructure change would come into play, further affecting the results and complicating the experiment.

The final set of parameters used is shown in Table 6.3, with every combination of parameters used for a total of 324 sets of models. Some of the parameters were used as ratios, rather than individual dimensions, so as to ensure the resultant parameter sets did not include impossible combinations, such as a case where $a > R_i > R_o$.

Early testing on the original NESC-I model indicated that the difference in mechanical material properties between the clad layer and the rest of the cylinder, had little effect on the resultant stress field and consequent crack driving forces, and so for the sake of simplicity, the different clad mechanical properties were omitted in subsequent models. The thermal properties did significantly affect the temperature field during the PTS however, so the clad layer was maintained in the thermal models. Rather than attempting to scale this however, it was simply kept as being 4 mm thick, as it was reasoned that this layer would be harder to change the dimensions of in a practical scenario, due to it being applied via welding.

For each of the 324 sets of parameters, three models were run: a thermal model, an elastic mechanical model and an elastic-plastic mechanical model. Due to the large total number of models, and the length of time required to run each one, the process of producing the models was automated and ultimately run on a dedicated Abaqus server capable of running multiple jobs in parallel. The modelling consisted of a number of steps:

1. Template python scripts (the language Abaqus uses in the generation of its models) were written to generate the thermal and mechanical

Table 6.3: The sets of parameters varied in the parametric scaling models

Parameter	NESC-I value	Parametric set
$\frac{R_i}{R_o}$	0.7491	0.3, 0.5 and 0.7491
R_o	697.5 mm	150, 200 and 250 mm
$\frac{a}{t}$	0.4229	0.4229, 0.6 and 0.7
ω	2100 rpm	2100, 6300, 8400 and 10 500 rpm
T_0	290 °C	290, 350 and 400 °C

models. All dimensions and parameters in these scripts were written so as to be modifiable. These scripts were then called using all the combinations of parameters listed in Table 6.3 to generate the 972 individual input files for every model. This process was performed locally as it was not particularly CPU or memory intensive.

2. The input files were then transferred to the server, which would run the thermal models, before applying the resultant temperature field output files as inputs to the mechanical models.

3. The resultant thermal and mechanical .odb output files were transferred to the local machines for processing.

The post processing of the results files used the Abaqus scripting interface to automatically extract the required values from the .odb results files, allowing for the examination of results as functions of time and temperature. This was particularly important, as it had been noted in the original NESC-I test that the fracture properties of the material were heavily temperature dependent. As a result of this, it was decided that in order to meet the fracture criterion, both the K_J value and temperature at that point would have to be the same, namely 290 MPa$\sqrt{\text{m}}$ and 70 °C.

The meshes used in these models were all based on those shown in Figs. 6.3 and 6.6, however they clearly had to vary given that the geometry of every model was different. The scripts used to generate the meshes relied on individual parameters such as the crack length, a, and the thickness of the cylinder, to generate meshes that provided sufficient detail around the areas of interest while maintaining a reasonable element ratio. As a result of the different meshes, the total number of elements used in the models varied from approximately 21 400 to 27 100, depending on which of the 27 different geometry combinations it used. It is neither practical, nor useful, to show every mesh utilised in this study, as they were all based on that shown in Figs. 6.3 and 6.6, however for illustrative purposes Fig. 6.9 shows the different geometry combinations used.

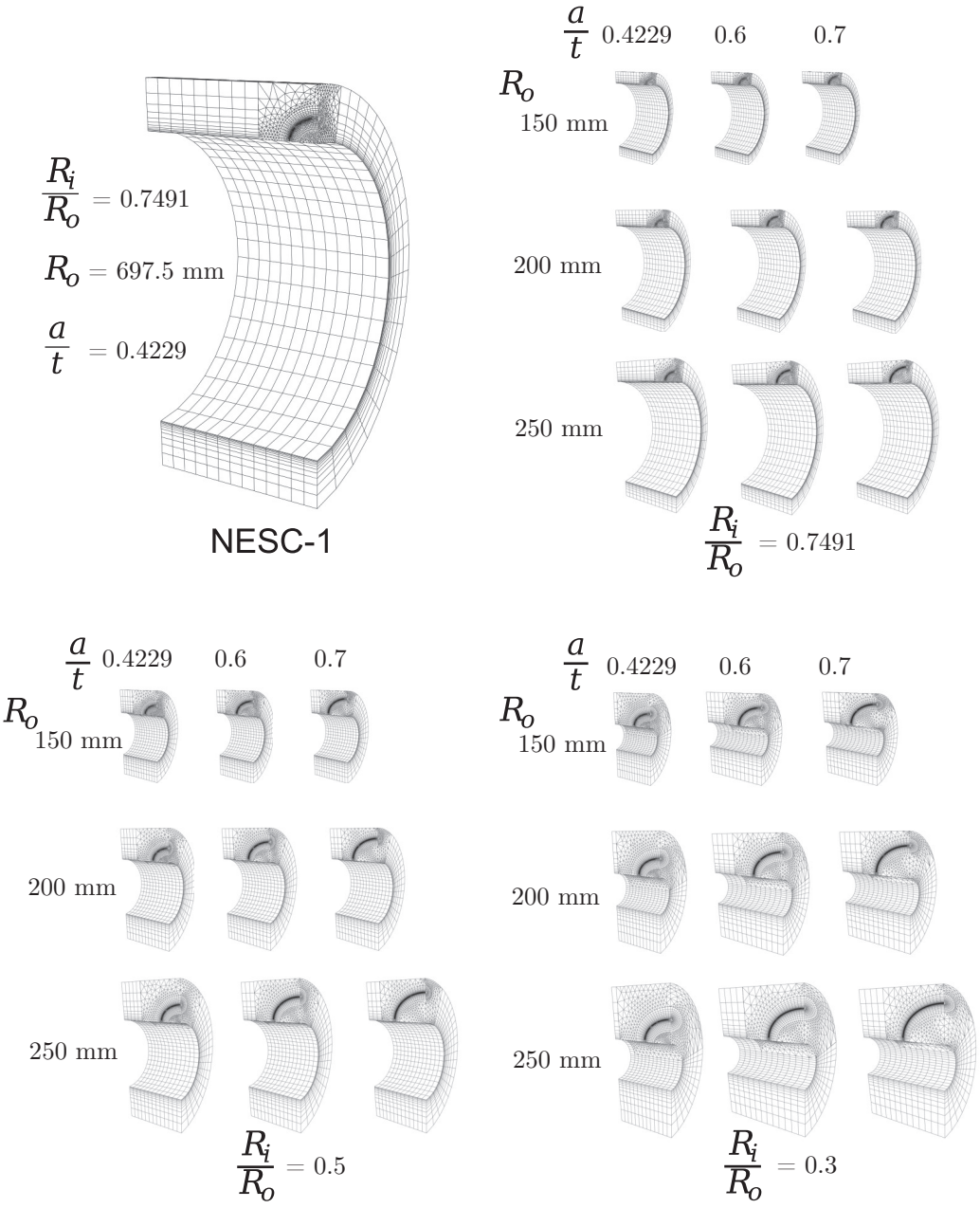

Figure 6.9: The 27 different geometry ratios used in the parametric study (Coules et al., 2017b)

6.4.2 Parametric modelling results

Upon completion of the simulations, the .odb files were retrieved from the Abaqus server and the scripts run to obtain the K_J and nodal temperature values for the points of interest along the crack, for all the simulations.

The 324 sets of models were comprised of 27 unique geometries, which then used 12 different combinations of starting temperature and angular velocity. The results of each of these sets were examined, looking for models

Table 6.4: Parameters used in the models shown in Fig. 6.10a

R_i/R_o	a/t	R_o (mm)	$T_0(^\circ\mathrm{C})$	ω (rpm)
0.3	0.6	200	290, 350 and 400	10500

Table 6.5: Parameters used in the models shown in Fig. 6.11

R_i/R_o	a/t	R_o (mm)	$T_0(^\circ\mathrm{C})$	ω (rpm)
0.3	0.6	200	400	2100, 6300, 8400 and 10 500

where the K_J value and temperature matched that of the NESC-I experiment; there were no results that immediately satisfied this criteria, however, there were sets of geometries that came close, overshooting and undershooting the required values and temperatures.

An example is shown in Fig. 6.10a, where three different models, all utilising the same geometry, but different starting temperatures, with the parameters listed in Table 6.4, came close to meeting the failure criterion. By fitting a simple line of best fit to the peak K_J values and then interpolating between them, a model that met the requirements was produced, utilising a starting temperature of approximately 320 °C. Running the thermal and mechanical models again using this geometry and starting temperature resulted in the K_J values and temperature field shown in Fig. 6.10b. As can be seen, the peak K_J values for this new model, and the original NESC-I specimen, intersect at 70 °C, suggesting both would fail at at the same point on the crack and at the same temperature.

This method of interpolating between results was not possible for all the combinations, as the majority of the groups required extrapolation beyond the imposed boundary conditions. Figure 6.11 shows one such example, displaying the results for a group of models using the same geometry as the successful models in Fig. 6.10, but with the temperature kept constant at 400 °C, and instead using the full set of angular velocities, as listed in Table 6.5. We can clearly see the effect that changing the angular velocity has on the K_J values, with a lower crack driving force produced as ω is decreased, which is to be expected given how it translates to applied pressure. The crack driving force as a result of the rotation is independent of temperature, and is simply added to the driving force caused by the temperature. The result of this is that ω cannot be used to change the temperature that the peak crack driving force occurs at, and consequently this geometry cannot be used to meet the criteria.

An additional point to note is that the focus here has been on achieving the same *peak* stresses at the right temperature, rather than anywhere else along the curve. For instance in the same example, shown in Fig. 6.11, the

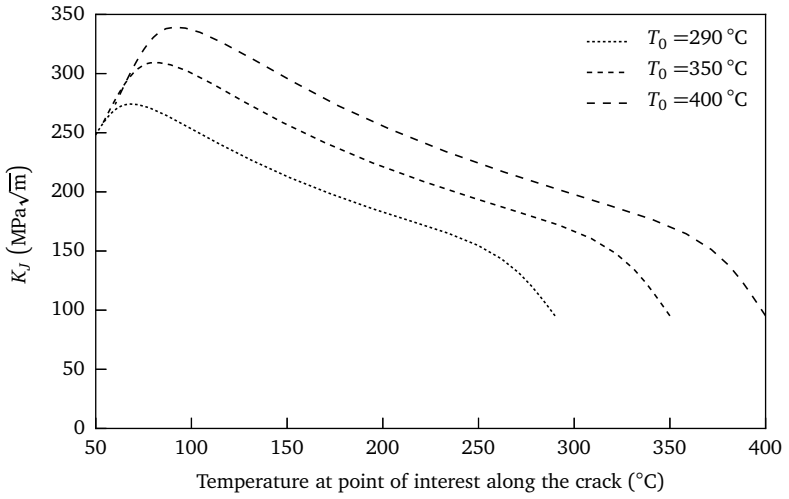

(a) The K_J values at the point of interest along the crack as its temperature changed during the PTS

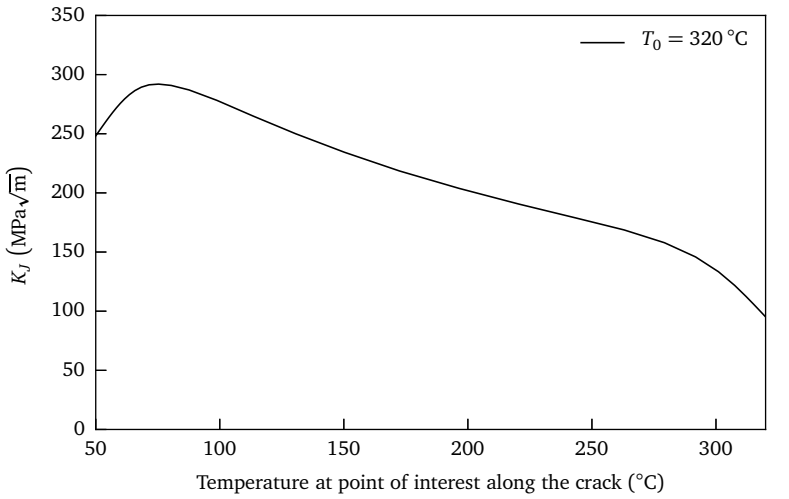

(b) The K_J values at the point of interest along the crack as its temperature changed during the PTS for the optimised model

Figure 6.10: The models with K_J values near that of the original NESC experiment and near the correct temperature (a), used to generate the optimised model (b). All used $R_i/R_o = 0.3$, $a/t = 0.6$ and $R_o = 200\,\text{mm}$

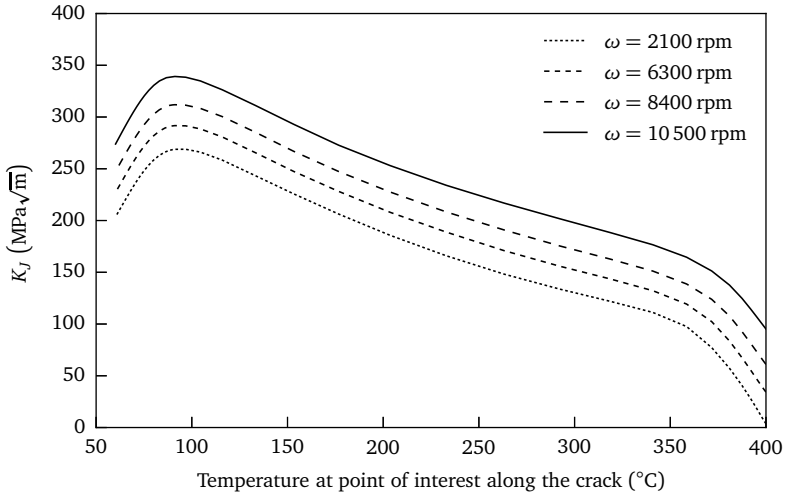

Figure 6.11: The effect of varying the angular rotation in an attempt to get the correct K_J value at the right temperature

model corresponding to the ω of 8400 rpm does actually reach the approximate K_J value of 290 MPa$\sqrt{\text{m}}$ at 70 °C, however it peaks at approximately 310 MPa$\sqrt{\text{m}}$ at 100 °C, meaning failure could have occurred earlier and at a different temperature.

6.5 Summary

The aim of the case study was to produce a scaled specimen that could reproduce the features of the original NESC-I experiment, while significantly reducing the size and adhering to imposed boundary conditions. The scaled down specimen described in Section 6.4.2, and whose dimensions are given in Table 6.4 at first glance appears to satisfy the objectives, with a reduction in weight of approximately 93% (from 6800 kg to 500 kg), making the specimen significantly more cost effective to produce, and the overall experiment simpler and safer to carry out.

The aim of the original NESC-I experiment had been to investigate the effect of pressurised thermal shock on the fracture behaviour of a specimen that included a multitude of well defined flaws. This case study only focused on one of these, and the resultant scaled specimen was designed with only that one flaw in mind. The scaling was such that the temperature and stress distributions across the component would be unlikely to cause any further flaws to behave in the same way.

Additionally, the type of scaling considered here was different to that carried out up until now, and used in the derivation of the scaling laws described in Chapter 3. These earlier examples considered simple scenarios in

which there was a relatively straightforward method of loading, and consequently the scaling laws could be used to produce the desired parameter in the scaled model. The complex combination of loads here meant this was harder to achieve, if not impossible; the temperature of the specimen was not just a load affecting the crack driving force, but also an output affecting the material properties, and consequently interlinked with the behaviour of the model. The results in Fig. 6.11, while not themselves able to produce a scaled model that satisfied the criteria, did show how in this complex case by changing the value of ω, (and therefore the applied pressure), resulted in the stress intensity factor changing proportionally.

The question also arises at this point of what constitutes a scaled model. Up until this chapter, the scaling considered had been geometric, i.e. where all dimensions had been scaled by one scale factor, λ; in this example, the scaling had been such that the dimensions could all be scaled by different amounts, essentially resulting in a different geometry, though still retaining all the important features. Using the earlier simple scaling laws, it suffices to know what loads the full size component will be placed under to be able to produce a scaled model with appropriately scaled loads and boundary conditions. With this method, however, while the outcome was also a smaller model with appropriately scaled loads, it required knowing the stress state, temperature field and crack driving forces beforehand, and then working back from them to produce the scaled model. Deriving a generalised scaling law from this, which would could then be applied to a similar cylinder but which different in some aspect, would be difficult.

On the other hand, the lack of a unifying simple scaling law does not mean that this process is not useful. If a sufficiently detailed finite element study were to be carried out for a large scale component, but without an experiment to back it up, the results from the finite element could still be used to inform a parametric analysis such as this to design a scaled down version, and which in turn could be validated experimentally.

Finally, to summarise:

- A case study was described, whose aim was to produce a scaled down version of a large pressurised thermal shock experiment.

- A parametric analysis was carried out, with the aim of producing a scaled down version of the experiment that was able to reproduce the crack driving forces for a specified crack, at a specific temperature. A range of parameters were used, with a total of 324 combinations.

- The exact driving forces and temperatures required were not produced using the range of tested parameters, however suitable candidates were found from which a final model was able to be interpolated. The result was a substantially smaller model, but which was

not uniformly scaled and which featured significantly different ratios of dimensions.

- This methodology used to create the scaled model required working backwards from a known stress field. This stress field could be the result of a detailed finite element study. The resultant scaled model produced using this methodology could then be validated experimentally. While not adding the degree of confidence that a full scale experimental validation would provide, it would serve to validate the small finite element model, and consequently the general finite element methods used.

Chapter 7

Discussion, conclusions and future work

7.1 Discussion

Table 7.1 lists the main analytical, finite element, and experimental work carried out in the course of this investigation, and which is discussed now.

Chapter 3 introduced some simple scaling laws for stress fields, stress intensity factors, and J-integral values. This related directly to the first objective, that of scaling the size of structural integrity assessments, by describing how loads needed to be scaled with respect to the geometry scale factor, so as to maintain the same value of the specified parameter.

For parameters that behave linearly, namely the stress intensity factor, the opposite also proved to be relatively straightforward, i.e. in a scenario where the applied load is scaled in proportion with the geometry (therefore keeping the applied stress constant), the values of K_{I} from the scaled model can be "converted" to those of the larger specimen.

This is clearly not the case for stress fields, which can depend on completely non-linear material properties, and result in vastly different outcomes if the loads are not scaled accordingly, The same is true for J values, which are also affected by non-linear behaviour, and the outcome is that it can be difficult to infer what the results of a larger specimen at a different relative load will be.

The scaling laws themselves only provide information on how to scale with respect to the parameter in question, however all of them are important in a structural integrity context. The fact that each parameter follows a different scaling law, tells us that it is not possible to scale so as to maintain all of them at the same time; a shrink fit, scaled so that the stress field is the same in both sizes, is not going to produce the same stress intensity factor if they were to both contain cracks. The fact that none of the parameters by themselves describes the complete state of a component, is what makes scaling a challenging problem.

Table 7.1: Summary of analytical, finite element and experimental studies carried out over the course of this investigation

	Analytical	Finite Element Analysis	Experimental
Stress fields	Analytical stress field examples focused on shrink fits, and a bar hanging under its own weight.	FEA models were carried out to predict the RS fields in the bend specimens.	Scaled beam specimens were bent, and the stress fields measured using neutron diffraction.
Stress intensity factors	Analytical solutions to scaled centre plates, cylinders, and beams were looked at.	FEA was carried on four point bends during the designing of the specimens for the fracture tests.	Scaled beams were loaded to failure in the fracture experiments.
J-integral		FEA of scaled side cracked plates were carried out to look at the effects of scaling on J.	
Complex case study		A parametric finite element study was carried out to produce a scaled complex component.	

7.1.1 The experiments

Reflecting on the design of the experiments

Chapter 4, which discussed the designing of the experiments, was again focused more on the first objective, which was to look at how scaling affected structural integrity assessments, rather than on the failure of a complex structure. The material used for these experiments, the Al-7449, was selected due to its low fracture toughness making it suitable for a both large and small fracture tests, while still being capable of being plastically deformed with relative ease. The same material was used for both sets of experiments, so as to demonstrate how both types of scaling phenomena could apply, while keeping the material properties the same.

Ideally, the geometry would have been kept the same for both sets of fracture and residual stress experiments, to maintain continuity. The lack of material data available when designing the experiments, however, and the time frame in which the experiments had to be carried out, meant that they had to be designed with a range of fracture toughnesses and the limitations of the fixtures in mind. Consequently, the a/W ratio of 0.5 was used for the fracture experiments, to ensure that even if the fracture toughness was at the extreme of what had been predicted, the loading rig and fixtures would still be capable of causing fracture.

When designing the experiments for the neutron diffraction experiments, the aim was to ensure that a sufficiently large residual stress field was introduced in both beams as to be clearly measurable, while also providing enough space for a sufficient number of points to be measured. These two requirements from the design objectives were at odds with each other, with the larger cracks introducing the largest residual stress fields, but providing the least space for measurements. The compromise that was reached, an a/W ratio of 0.35, would in hindsight have also been large enough to fracture the beams at a reasonable load, as well as introducing residual stresses in the reversed orientation.

The width of the crack in the residual stress specimens is also worth some further consideration. Examining the finite element analyses that were carried out to examine the effect of the width, the results clearly indicated that using the thinnest available wire for the insertion of the crack, in this case would not produce the same stress fields, and that the cracks in this case needed to be modelled as notches having a finite width as opposed to idealised cracks. Presumably as the width of the crack or notch was reduced, either by significantly finer EDM wires, or insertion of the crack using an alternative manufacturing method, then the difference in stress fields caused by having different relative crack thicknesses would also diminish.

The fracture experiment results

The results from the first set of experiments, where the objective was to validate the scaling law described in Section 3.2, appeared to achieve just that. By fitting a Weibull curve to both sets of data, the mean stress value, K_0, was found to be virtually identical for both size beams (44.25 MPa$\sqrt{\text{m}}$ and 43.58 MPa$\sqrt{\text{m}}$ for the large and small beams respectively).

Despite the mean stress intensity fractures at failure being very close for both sizes, the distributions themselves were clearly noticeably different, with the smaller beam exhibiting significantly more scatter than the larger beam. This manifested itself both as a wider range of K_{I} values at failure, and so consequently as as shallower sloped Weibull curve. The slope is governed by the Weibull modulus, m_1, which due to the increased scatter was larger for the small beam (5.58 and 4.71 for the small and large beams respectively).

Being from the same material, one might have expected that if the fracture toughness at both sizes was the same, that the material would behave similarly in terms of scatter. It was not only the Weibull modulus that differed from large to small however, but also the third parameter, K_{min}, which produced the closest fit for the small beam when it was equal to 0.

The physical meaning behind K_{min} is a lower threshold, below which the probability of a load (and its corresponding stress intensity factor) causing failure is said said to be 0. The fact that the large beam has a threshold of 32.08 MPa$\sqrt{\text{m}}$, whereas the smaller beam does not have one, might suggest that despite on average failing at the stresses predicted by the scaling law, the smaller beams, given a sufficiently high number of fracture experiments, might fail at a substantially lower scaled load than the large beams. Having a K_{min} value of 0 MPa$\sqrt{\text{m}}$ is not in itself unreasonable, and past experiments on aluminium have produced the same results (Holland and Zaretsky, 1990), however such a large difference in the properties of the two different size specimens does seem unusual.

What seems more probable however, is that errors in the carrying out of the experiment had a much bigger impact on the results of the small specimens than the large specimens. Errors made could include misalignment of the specimen in the bending rig, or an angular misalignment of the bending rig in the crosshead grips, both of which could have happened in both sets of experiments. These errors would have been independent of the size of the beam, and consequently have had a larger impact on the smaller specimens, as these finite misalignments or rotations would have been three times the relative size for the small beams compared to the large ones.

Any error in the measurement of the loads would have had a greater effect on the small beams too. This type of error could have come from a number of sources, of which the most obvious are the load cells on both of the loading rigs, from which the applied forces were measured, and from

incorrectly identifying the failure load. Addressing the second point first, it seems unlikely that this would have been an issue; while there may be ambiguity in some materials in determining exactly where yield has occurred, or the exact gradient of a curve to determine the Young's modulus, the failures in these cases were sudden, and consisted of an immediate reduction in load to essentially 0 kN, as shown back in Fig. 5.2, leaving little room for misinterpretation.

Potential errors arising from the load cells are also unlikely to explain the spread of data; the smallest load to cause failure in the small beams was approximately 6.51 kN, with the largest load being 9.54 kN. The load cells were both calibrated, and found to produce errors of no more than ±1%, which does not account for the difference in failure loads of over 3 kN.

The relatively small sample sizes used here, particularly in the case of the smaller beam, make it hard to draw definitive conclusions as to the differences in behaviour between the two sizes. The mean value of fracture toughness, K_0, was essentially the same, validating the scaling law, however the large increase in scatter associated with the smaller beam would require further research.

The residual stress experiment results

The purpose of the residual stress experiments were to examine the effect of scaling on stress fields in the presence of cracks and stress concentrators. The scaling law associated with scaling stress fields, discussed in Section 3.1, was also straightforward, and these experiments also served as validation.

As mentioned above in the discussion on the design of the experiments in Section 7.1.1, some further thought is needed here on the widths of the cracks that were used, as they were also scaled along with the lengths. One of the assumptions that was being looked at with this experiment was that the plastic zone ahead of the crack tip scaled proportionally with the specimen, if the loads were scaled such that the rest of the stress fields were the same in both specimens. The plastic zone occurs as a result of the notch or crack concentrating the loads ahead of the tip, so that the stresses exceed the yield stress; as this area cannot bear any load, it results in a further redistribution of stresses, extending the plastic zone. The size of this plastic zone is dependent on how the stresses are concentrated, and the general expressions for the plastic zone are a function of the stress intensity factor, K_{I}.

As was mentioned in Section 4.3, research suggested that a notch with a radius of up to 140 µm can be considered to act as if it were a crack (Kamat, 1991). Both notches used in this experiment were thin enough to be considered cracks, however the radius of the larger specimen was clearly approaching the limit. If the experiment were to be scaled up so that the large specimen were even larger, this assumption would cease to be valid

very quickly. Were this experiment to be carried out, the effect that a larger notch would have on the plastic zone would be worth considering.

The actual bending of the beams, and the generation of the residual stress fields, was reasonably straightforward, with the load-displacement curves showing good agreement with their finite element prediction counterparts. As discussed in Chapter 5, the residual stresses measurements from the neutron diffraction experiment also showed excellent agreement with their finite element analysis counterparts.

The differences in the results were discussed earlier, but to summarise, the most noticeable difference between the two different size beams was a large compressive stress (in the order of approximately 100 MPa), present in the y and z directions. The benefit of carrying out the measurements twice was that they could be compared to see whether these features appeared consistently across both sets of results, which they did not.

This presented two obvious possibilities: either this compressive stress was really present at the surface, but for an unknown reason was not being detected when using the radial collimator, or alternatively that something about the way in which the slits were being used was causing this non existent stress to be detected in the two orientations. It was of course possible that residual stresses had been introduced due to the machining processes, and that they were only detected in the smaller beam due to the smaller gauge volume. However, if this had been the case, then it would have been expected that they would be visible using the radial collimators, which provided a higher resolution view of the strains in the material.

What was instead deemed more likely, was that it was a measurement error, attributed to the gauge volume not being completely contained within the specimen. As mentioned earlier, the specimens were very carefully aligned, and there was nothing to suggest that the alignment of either specimen was at all inaccurate. When describing the gauge volumes earlier in Chapter 5, the dimensions given were for cuboid approximations, however in reality they tend to resemble parallelopipeds (Reimers et al., 1998), whose elongated shape is defined by the diffraction angles and beam divergence. With the measurements taking place right at the surface of the specimen, it is probable that this elongated volume overlapped the surface of the specimen, extending into the surrounding air. This "edge effect" is known to cause a peak shift, resulting in a corresponding error in strain measurement at that point (Spooner and Wang, 1997; Wang et al., 1998b), and so could well have been responsible for the unexplained compressive stress measurement.

Experimental results overall

The experiments examined the two scaling laws considered in Chapter 3, describing the scaling of stress fields and stress intensity factors, with results

demonstrating that in simple scenarios, such as a straightforward four point bend, they are valid.

The scaling laws do not account for any potential interaction between the two effects however. For many materials, this is not a problem, as only one type of failure mechanism dominates, and consequently the other scaling law will have no bearing on it. For the many other materials for which both types of failure mechanism are a concern however, the way in which these scaling laws interact is critical.

As discussed in Chapter 3, in order to maintain the same stress field in a scaled component, the applied load has to be scaled by λ^2. Similarly for the stress intensity factor to be maintained in a scaled component, the applied load must be scaled by $\lambda^{1.5}$. The result is that for components made from materials capable of elastic-plastic fracture, the size of the component is going to have an effect on the manner in which it fails.

For simple components, such as the beams used in both sets of experiments, the incompatibility in scaling laws is manageable and can be taken into account in both the analysis and the experiments One of the objectives of this work however, was to consider the feasibility of conducting scaled tests of complex structural components.

The fact that these scaling laws are incompatible has the potential to complicate the problem when dealing with specimens that are not as idealised as the beams used up till now, and with potentially much more complicated loading methods applied. A complex structure with potentially complex boundary conditions, when scaled down, is going to require a larger load in order to obtain the same stress intensity factor, than if the objective were to replicate the stress strain field. While this change in the stress strain field may not be sufficient in itself to cause failure, it may well be sufficient as to mean that the scaled test does not accurately indicate how the full sized component would behave in similar conditions.

7.1.2 The complex case study

The complex case study addressed this exact issue, examining a more complex component, subjected to a combination of loading mechanisms, and imposing the type of constraints that might be imposed by a real life problem. The failure criteria that was measured in the original NESC-I experiment, and used in the subsequent models, was unobtainable in the scaled models using the imposed boundary conditions, so non-uniform scaling was explored.

A suitable set of parameters was eventually found, however as mentioned earlier, it raises the question of what constitutes a scaled model. It replicated the features of the original component, however its geometry was entirely different to how it originally started.

This method also relied on working backwards, i.e. the results (the time

dependent stress strain field and temperature distributions) were already known beforehand for the large original component, and the aim was to replicate these conditions in the smaller version. The results obtained from this did not provide a unifying theory, or a framework which would allow for another scaled model to be produced in the original boundary conditions or properties were changed, in the way that the simple scaling laws described in Chapter 3 did. On the contrary, it actually required many hours of computational processing in order to eventually reproduce results that were already known.

This method is not without its merits though. Were the original experiment required to be carried out again, it could now be carried out with much less difficulty and expense than the first time round; provided of course that it was the J values that were of interest, and not the temperature distributions or stress-strain fields.

Similarly, had the original experiment not been carried out, but the specifications and material characterisation still exist, then the reverse could be performed. A scaled model could be produced using the described approach, working from a full size model and its predicted stress fields and failure criteria, rather than from the experimental values. Carrying out this scaled down experiment would serve to validate the scaled down finite element model, which in turn would add confidence the finite element methods used across both size models.

This approach may not add the degree of confidence that a straight forward, full size, physical validation would add to modelling, however in a scenario where this was not possible, then validating a scaled down simulation would add a substantial amount more confidence than no experimental data.

7.2 Conclusions

7.2.1 Summary of conclusions, in relation to the objectives

Referring back to the original objectives, originally listed back in Chapter 1, the points have all been addressed:

- Determine the current start of scaling research in a structural integrity context.

- Develop simple scaling laws, which can be used in structural tests, highlighting any shortcomings.

- Investigate the feasibility of producing a scaled complex model that can be used in the structural integrity evaluation of a large component.

The conclusions which follow, are in answer to these objectives. They by no means provide a comprehensive study of the entire topic of "scaling", and the findings and conclusions produced as a result of this work lead to further questions. A number of suggestions are provided in Section 7.4, for the direction that future work could take, based on this research.

1. The scaling of simple components in laboratory conditions is not only possible, but relatively straightforward. Scaling laws governing stress fields, stress intensity factors, and J-integrals, were all described.

2. Having described these scaling laws, it was also implicitly shown that the parameters considered in this work do not scale in proportion with each other. Depending on the specifics in which these scaling laws are being used, some or all of the parameters may be of interest, in which case compromises have to be made when producing a scaled model.

3. By extrapolating results and with the use of failure assessment diagrams to visualise this, it is possible to see that depending on the geometry, material properties, and loading regime, there will come a point with which the failure mechanisms will change. The results using the described scaling laws will not be directly applicable in these cases, and therefore the results harder to translate from one scale to another.

4. The fracture experiments appeared to validate the scaling law, describing how to scale loads so as to obtain the same stress intensity factors in scaled specimens, along with how to calculate the stress intensity factor when the loads is not scaled proportionally. A larger sample size is needed in order to draw meaningful conclusions from the scatter however.

5. While a crack may behave as if it were a singularity when dealing with fracture, this assumption is not necessarily valid in all scenarios. As the introduction of the residual stress field show, despite the notches being thin enough that they could be considered cracks from a fracture perspective, they required appropriate scaling to enable the same residual stress fields to be introduced into both specimens.

6. The scaling of complex models, i.e. one that might be required in a real life scenario, is much more complicated than when using idealised small specimens. It is possible to work backwards from results, be they experimental or derived numerically, to produce a model that replicates some of the parameters of interest. The different scaling laws mean that the whole model is not able to be accurately scaled however, and so careful thought is required as to what the requirements are and what the purpose of the model is. This approach can definitely add

a degree of confidence to modelling that would undoubtedly be useful should full size experimental validation not be an option, however ultimately it is not a replacement for full scale modelling.

7. There are certain conditions however, in which scaling is an appropriate and useful tool. For specimens where fracture occurs, if the small scale yielding conditions at the crack tip are maintained across the sizes, then scaled models can be reliably used to produce a model that accurately replicates the fracture conditions, and from which results from the scaled model can be transferred across to the full size. For the small scale yielding conditions to be maintained, the limitation will be on how small the scaled model can be made.

   Similarly for models where failure is due to the global stress field, scaling can be used provided this remains the dominant contributor to failure. Where there are stress concentrating features, care must be taken if the scaled model is larger in sizes than the original specimen, as this can tend towards small scale yielding conditions, and consequently a change in failure mechanism. Where these conditions are met however, then scaled models may confidently be used to replicate and further investigate the failure conditions of the original specimens.

8. This research was limited to scenarios where the material can be treated as a continuum. This is not an assumption that can be made lightly, as the microstructure and grain sizes of a material can easily be large enough to become significant. As such, care must be taken to ensure that the continuum assumption is appropriate.

7.3 Contribution to field

As was mentioned early on, the topic of scaling is a broad one, and which is already used extensively in other engineering disciplines. In the field of structural integrity, however, its use is limited, and largely focussed on scaling structural test specimens rather than engineering components.

This work has contributed to the discussion around scaling in a practical structural context, demonstrating how simple scaled models can be achieved, as well as their shortcomings and when it is appropriate to use them.

Furthermore, a methodology has been developed for designing scaled complex components, for use in structural experiments. This methodology is not without its limitations, requiring careful thought as to what its desired purpose is, and what outputs are required. It cannot necessarily provide the level of confidence that a full scale model provides, however, with that in mind, in a scenario where a full scale test is not possible, a scaled model

might be used to add substantially more confidence than no physical validation at all.

7.4 Future work

After careful consideration of the results and conclusions drawn from this work, the following areas preent themselves for future work and exploration.

Additional experiments, focussing on the simple scaling laws, would add confidence and could be used to validate the interaction between them, as opposed to separately as they were considered in the experiments described in Chapters 4 and 5. Using larger sample numbers this time, so as to obtain additional confidence in the resultant distributions, specimens could be designed such that the same fracture tests could be carried out at varying sizes, but scaled such that the smaller specimens undergo plasticity before fracture. This would highlight how in that case, neither scaling law by itself could be used to completely account for failure when scaling.

Another area highlighted for further work, is in the complex case study, where physical validation has yet to be carried out. Physical validation for the methodology of developing a scaled model would not require the specific case study used in this example, which might prove to be technically challenging, but could instead focus on a component subjected to a simpler loading regime. Utilising the parametric scaling methodology described here, the physical validation could be carried out for both scaled, thereby adding confidence to this technique and demonstrating its utility, as well as drawing attention to the limitations that were discussed when using this methodology.

Bibliography

Ainsworth, M. and Oden, J. T. (1997). A posteriori error estimation in finite element analysis. *Computer methods in applied mechanics and engineering*, 142(1-2):1–88.

Ainsworth, R., Sharples, J., and Smith, S. (2000). Effects of residual stresses on fracture behaviour – experimental results and assessment methods. *J. of Strain Analysis for Engineering Design*, 35(4):307–316.

Aluminum Association (2000). *Aluminum standards and data*. Aluminum Association.

Anderson, T. L. (2017). *Fracture mechanics: fundamentals and applications*. CRC press.

Ávila, J. A., Lima, V., Ruchert, C. O., Mei, P. R., and Ramirez, A. J. (2016). Guide for recommended practices to perform crack tip opening displacement tests in high strength low alloy steels. *Soldagem & Inspeção*, 21(3):290–302.

Baratta, F. I. and Fett, T. (2000). The effect of load and crack misalignment on stress intensity factors for bend-type fracture toughness specimens. *Journal of testing and evaluation*, 28(2):96–102.

Bass, B., Wintle, J., and Hurst, R. (2001). NESC-I Project Overview. European Commission.

Bažant, Z. P. (1984). Size effect in blunt fracture: Concrete, rock, metal. *Journal of Engineering Mechanics*, 110(4):518–535.

Bažant, Z. P. (2000). Size effect. *International Journal of Solids and Structures*, 37(1):69–80.

Bažant, Z. P. (2005). *Scaling of structural strength*. Butterworth-Heinemann.

Bažant, Z. P. and Chen, E.-P. (1997). Scaling of structural failure. *Applied Mechanics Reviews*, 50(10):593–627.

Bažant, Z. P., Gattu, M., and Vorel, J. (2012). Work conjugacy error in commercial finite-element codes: its magnitude and how to compensate for it. In *Proc. R. Soc. A*, page rspa20120167. The Royal Society.

Bažant, Z. P., Kim, J.-K., and Pfeiffer, P. A. (1986). Nonlinear fracture properties from size effect tests. *Journal of Structural Engineering*, 112(2):289–307.

Beachem, C. D. and Meyn, D. A. (1968). Fracture by microscopic plastic deformation processes. In *Electron Fractography*, pages 59–88. ASTM International.

Becker, T., Mostafavi, M., Tait, R., and Marrow, T. (2012). An approach to calculate the j-integral by digital image correlation displacement field measurement. *Fatigue & Fracture of Engineering Materials & Structures*, 35(10):971–984.

Begley, J. and Landes, J. (1972). The J integral as a fracture criterion. In *Fracture Toughness: Part II*. ASTM International.

Booker, J. D., Raines, M., and Swift, K. G. (2001). *Designing Capable and Reliable Products*. Butterworth-Heinemann.

Bottasso, C. L., Campagnolo, F., and Petrović, V. (2014). Wind tunnel testing of scaled wind turbine models: Beyond aerodynamics. *Journal of wind engineering and industrial aerodynamics*, 127:11–28.

Bower, A. (2009). *Applied Mechanics of Solids*. CRC Press.

British Energy Generation Ltd. (2000). R6, revision 4: Assessment of the integrity of structures containing defects.

Broek, D. (1986). *Elementary Engineering Fracture Mechanics*. Kluwer Academic Publishers, 4th edition.

BS EN ISO 6892-1 (2016). Metallic materials. tensile testing. part 1. method of test at room temperature. Standard, British Standards Institution.

Budden, P. J. (2006). Failure assessment diagram methods for strain-based fracture. *Engineering Fracture Mechanics*, 73(5):537–552.

Bueckner, H. (1970). Novel principle for the computation of stress intensity factors. *Zeitschrift fuer Angewandte Mathematik & Mechanik*, 50(9).

Chapuliot, S. (2000). K i formula for pipes with a semi-elliptical longitudinal or circumferential, internal or external surface crack. Technical report, CEA/Saclay.

Coules, H., Orrock, P., and Truman, C. (2017a). Feasibility of reduced-size spinning cylinder specimens for pressurised thermal shock testing. In *ASME 2017 Pressure Vessels and Piping Conference*. American Society of Mechanical Engineers.

Coules, H., Orrock, P., and Truman, C. (2017b). Parametric design of scaled-down pressurised thermal shock test specimens using inelastic analysis. *Engineering Fracture Mechanics*, 176:308–325.

Danzer, R. (2006). Some notes on the correlation between fracture and defect statistics: Are Weibull statistics valid for very small specimens? *Journal of the European Ceramic Society*, 26(15):3043–3049.

Dassault Systémes. Vélizy-Villacoublay (2013). Software for finite element analysis abaqus/complete abaqus environment, version 6.12.

Daymond, M. and Priesmeyer, H. (2002). Elastoplastic deformation of ferritic steel and cementite studied by neutron diffraction and self-consistent modelling. *Acta materialia*, 50(6):1613–1626.

Denkena, B. and De Leon, L. (2008). Milling induced residual stresses in structural parts out of forged aluminium alloys. *International Journal of Machining and Machinability of Materials*, 4(4):335–344.

Dieter, G. E. and Bacon, D. J. (1986). *Mechanical metallurgy*, volume 3. McGraw-hill New York.

Eik, K. and Marchenko, A. (2010). Model tests of iceberg towing. *Cold Regions Science and Technology*, 61(1):13–28.

Engelen, R., Fleck, N., Peerlings, R., and Geers, M. (2006). An evaluation of higher-order plasticity theories for predicting size effects and localisation. *International journal of solids and structures*, 43(7):1857–1877.

Farrell, S., MacGregor, L., and Porter, J. (2010). Stress analysis on canadian naval platforms using a portable miniature x-ray diffractometer. *Powder Diffraction*, 25(2):119–124.

Fitzpatrick, M. E. and Lodini, A. (2003). *Analysis of residual stress by diffraction using neutron and synchrotron radiation*. CRC Press.

Fleck, N. and Hutchinson, J. (1997). Strain gradient plasticity. *Advances in applied mechanics*, 33:296–361.

Fleck, N., Muller, G., Ashby, M., and Hutchinson, J. (1994). Strain gradient plasticity: theory and experiment. *Acta Metallurgica et Materialia*, 42(2):475–487.

Griffith, A. A. (1921). The phenomena of rupture and flow in solids. *Philosophical transactions of the royal society of london. Series A, containing papers of a mathematical or physical character*, 221:163–198.

Gronet, M., Crawley, E., and Allen, B. (1989). Design, analysis, and testing of a hybrid scale structural dynamic model of a space station. In *30th Structures, Structural Dynamics and Materials Conference*, page 1340.

Gy, R. (2008). Ion exchange for glass strengthening. *Materials Science and Engineering: B*, 149(2):159–165.

Hauk, V. (1997). *Structural and residual stress analysis by nondestructive methods: Evaluation-Application-Assessment*. Elsevier.

Hayes, D. (1975). Origins of the stress intensity factor approach to fracture. *Journal of Strain Analysis*, 10(4):198–200.

Hearn, E. J. (1997). *Mechanics of Materials 2: The mechanics of elastic and plastic deformation of solids and structural materials*. Butterworth-Heinemann.

Heyer, R. (1973). Crack growth resistance curves (R-curves)-literature review. In *Fracture Toughness Evaluation by R-Curve Methods*. ASTM International.

Ho, K. and Newman, S. (2003). State of the art electrical discharge machining (edm). *International Journal of Machine Tools and Manufacture*, 43(13):1287–1300.

Holland, F. and Zaretsky, E. (1990). Investigation of weibull statistics in fracture analysis of cast aluminum. *Journal of Mechanical Design*, 112(2):246–254.

Hossain, A. and Zimmer, W. (2003). Comparison of estimation methods for weibull parameters: complete and censored samples. *Journal of statistical computation and simulation*, 73(2):145–153.

Hossain, S., Truman, C., Smith, D., and Daymond, M. (2006). Application of quenching to create highly triaxial residual stresses in type 316h stainless steels. *International journal of mechanical sciences*, 48(3):235–243.

Hosseinzadeh, F., Mahmoudi, A., Truman, C., and Smith, D. (2009). Prediction and measurement of through thickness residual stresses in large quenched components. In *Proceedings of the world congress on engineering*, volume 2.

Hutchings, M. T., Withers, P. J., Holden, T. M., and Lorentzen, T. (2005). *Introduction to the characterization of residual stress by neutron diffraction*. CRC press.

Inglis, C. (1913). Stresses in a plate due to the presence of cracks and sharp corners. *Trans Nav Archit (London)*, 60:213.

Instron (2009 (accessed August 24, 2017)). *Bluehill® Software*.

Irwin, G. R. (1956). Onset of fast crack propagation in high strength steel and aluminum alloys. Technical report, Naval Research Lab, Washington DC.

Irwin, G. R. (1957). Analysis of stresses and strains near the end of a crack traversing a plate. *Journal of applied mechanics*, 24(3):361–364.

Irwin, G. R. and Kies, J. (1954). Welding research supplement 19.

Jayatilaka, A. d. S. and Trustrum, K. (1977). Statistical approach to brittle fracture. *Journal of Materials Science*, 12(7):1426–1430.

Kamat, S. (1991). Effect of notch root radius on fracture toughness of an 8090 aluminium - lithium alloy. 25(c):1519–1523.

Kamp, N., Sinclair, I., and Starink, M. (2002). Toughness-strength relations in the overaged 7449 al-based alloy. *Metallurgical and Materials Transactions A*, 33(4):1125–1136.

Kao, J. H. (1958). Computer methods for estimating weibull parameters in reliability studies. *IRE Transactions on Reliability and Quality Control*, pages 15–22.

Kobayashi, A., Chiu, S., and Beeuwkes, R. (1973). A numerical and experimental investigation on the use of j-integral. *Engineering Fracture Mechanics*, 5(2):293–305.

Labuz, J. and Biolzi, L. (1998). Characteristic strength of quasi-brittle materials. *International journal of solids and structures*, 35(31-32):4191–4203.

Le, J., Bažant, Z. P., and Yu, Q. (2010). Scaling of strength of metal-composite joints—part II: Interface fracture analysis. *Journal of Applied Mechanics*, 77(1).

Leitz, C. and Koban, J. (1989). Development of reactor pressure vessel design, neutron fluence calculation, and material specification to minimize irradiation effects. In *Radiation Embrittlement of Nuclear Reactor Pressure Vessel Steels: An International Review (Third Volume)*. ASTM International.

Maddox, S. (1974). Assessing the significance of flaws in welds subject to fatigue. *Welding journal*, 53(9).

Mahmoudi, A., Hossain, S., Truman, C., Smith, D., and Pavier, M. (2009). A new procedure to measure near yield residual stresses using the deep hole drilling technique. *Experimental mechanics*, 49(4):595–604.

Mahmoudi, A. H., Aird, C., Truman, C. E., Mirzaee-Sisan, A., and Smith, D. J. (2006). Generating well defined residual stresses in laboratory specimens. In *Proceedings of the ASME pressure vessels and piping conference*, volume 6, pages 631–639.

Mendez, P. F. and Eagar, T. W. (2003). Penetration and defect formation in high-current arc welding. *Welding Journal*, 82(10):296.

Morel, S. (2007). R-curve and size effect in quasibrittle fractures: Case of notched structures. *International journal of solids and structures*, 44(13):4272–4290.

Mura, T. (1987). *Micromechanics of defects in solids*. Martinus Nijhoff Publishers, 2nd edition.

Newman, J. and Raju, I. (1981). An empirical stress-intensity factor equation for the surface crack. *Engineering fracture mechanics*, 15(1-2):185–192.

Novovic, D., Dewes, R., Aspinwall, D., Voice, W., and Bowen, P. (2004). The effect of machined topography and integrity on fatigue life. *International Journal of Machine Tools and Manufacture*, 44(2):125–134.

Odette, G. and Lucas, G. (2001). Embrittlement of nuclear reactor pressure vessels. *JOM*, 53(7):18.

Orowan, E. (1949). Fracture and strength of solids. *Reports on Progress in Physics*, 12(1):185.

Orrock, P., Booker, J., and Truman, C. E. (2017). Scaled four point bend specimens and the transferability of their results. In *Proc. 14th International Conference on Fracture (ICF)*.

Orrock, P., Smith, D. J., and Truman, C. E. (2015). A study of the effects of scaling on structural integrity assessment. In *ASME 2015 Pressure Vessels and Piping Conference*. American Society of Mechanical Engineers.

Orrock, P. and Truman, C. E. (2016). A study of the effects of scaling on structural integrity assessment and feasibility of physical validation. In *ASME 2016 Pressure Vessels and Piping Conference*. American Society of Mechanical Engineers.

Panontin, T. and Hill, M. (1996). The effect of residual stresses on brittle and ductile fracture initiation predicted by micromechanical models. *International Journal of Fracture*, 82(4):317–333.

Pedersen, P. (2006). On shrink fit analysis and design. *Computational Mechanics*, 37(2):121–130.

Price, J. W., Ziara-Paradowska, A., Joshi, S., Finlayson, T., Semetay, C., and Nied, H. (2008). Comparison of experimental and theoretical residual stresses in welds: The issue of gauge volume. *International Journal of Mechanical Sciences*, 50(3):513–521.

Randau, C., Garbe, U., and Brokmeier, H.-G. (2011). StressTextureCalculator: a software tool to extract texture, strain and microstructure information from area-detector measurements. *Journal of Applied Crystallography*, 44(3):641–646.

Reimers, W., Broda, M., Brusch, G., Dantz, D., Liss, K.-D., Pyzalla, A., Schmackers, T., and Tschentscher, T. (1998). Evaluation of residual stresses in the bulk of materials by high energy synchrotron diffraction. *Journal of Nondestructive Evaluation*, 17(3):129–140.

Rice, J. R. (1967). A path independent integral and the approximate analysis of strain concentration by notches and cracks. *Journal of Applied Mechanics*, 35(2):379–386.

Rice, J. R. (1968). Mathematical analysis in the mechanics of fracture. *Fracture: an advanced treatise*, 2:191–311.

Rice, J. R. (1972). Some remarks on elastic crack-tip stress fields. *International Journal of Solids and Structures*, 8(6):751–758.

Rice, J. R., Paris, P., and Merkle, J. (1973). Some further results of j-integral analysis and estimates. In *Progress in flaw growth and fracture toughness testing*. ASTM International.

Robinson, J., Hossain, S., Truman, C., Paradowska, A., Hughes, D. J., Wimpory, R., and Fox, M. (2010). Residual stress in 7449 aluminium alloy forgings. *Materials Science and Engineering: A*, 527(10):2603–2612.

Rossum, G. (1995). Python reference manual. Technical report, Amsterdam, The Netherlands, The Netherlands.

Silva, E. P., Pacheco, P. M. C. L., and Savi, M. A. (2004). On the thermomechanical coupling in austenite–martensite phase transformation related to the quenching process. *International Journal of Solids and Structures*, 41(3):1139–1155.

Smith, E. (2000). Normalised effective K_r versus L_r failure assessment diagrams as applied to a flaw in the vicinity of a stress concentration. *International journal of engineering science*, 38:1153–1159.

Smith, M. C. and Smith, A. C. (2017). Advances in weld residual stress prediction: A review of the net tg4 simulation round robin part 1, thermal analyses. *International Journal of Pressure Vessels and Piping*.

Spooner, S. and Wang, X.-L. (1997). Diffraction peak displacement in residual stress samples due to partial burial of the sampling volume. *Journal of applied crystallography*, 30(4):449–455.

Tada, H., Paris, P., and Irwin, G. R. (2000). *The Stress Analysis Of Cracks Handbook*. ASME Press, 3rd edition.

Takahashi, Y. (2002). Evaluation of leak-before-break assessment methodology for pipes with a circumferential through-wall crack. Part I: stress intensity factor and limit load solutions. *International Journal of Pressure Vessels and Piping*, 79(6):385–392.

Taylor, G. I. (1934). The mechanism of plastic deformation of crystals. part I. theoretical. *Proceedings of the Royal Society of London. Series A, Containing Papers of a Mathematical and Physical Character*, 145(855):362–387.

Timoshenko, S. P. (1956). *Strength of Materials: Part II Advanced Theory and Problems*. D. Van Nostrand, third edition.

Towers, O. L. and Dawes, M. G. (1985). Welding institute research on the fatigue precracking of fracture toughness specimens. In *Elastic-Plastic Fracture Test Methods: The User's Experience*. ASTM International.

Truman, C. and Booker, J. (2007). Analysis of a shrink-fit failure on a gear hub/shaft assembly. *Engineering Failure Analysis*, 14(4):557–572.

Wallin, K. (1985). The size effect in K_{IC} results. *Engineering Fracture Mechanics*, 22(1):149–163.

Walpole, R., Myers, R., Myers, S., and Ye, K. (2002). *Probability & statistics for engineers & scientists*. Prentice Hall, 7th edition.

Walsh, P. F. (1979). Fracture of plain concrete. *Indian Concrete Journal*, 46(11).

Wang, S., Li, Y., Yao, M., and Wang, R. (1998a). Compressive residual stress introduced by shot peening. *Journal of Materials Processing Technology*, 73(1):64–73.

Wang, X.-L., Spooner, S., and Hubbard, C. (1998b). Theory of the peak shift anomaly due to partial burial of the sampling volume in neutron diffraction residual stress measurements. *Journal of applied crystallography*, 31(1):52–59.

Webster, G. and Ezeilo, A. (2001). Residual stress distributions and their influence on fatigue lifetimes. *International Journal of Fatigue*, 23:375–383.

Weibull, W. (1939). A statistical theory of the strength of materials. *Ingeniörsvetenskapsakademiens Handlingar. Stockholm: Generalstabens Litografiska anstalts förlag*, (151).

Westergaard, H. (1939). Bearing pressures and cracks. *Journal of applied mechanics*, 18:49–53.

Williams, E. (1957). Some observations of Leonardo, Galileo, Mariotte and others relative to size effect. *Annals of Science*, 13(1):23–29.

Wimpory, R., Ohms, C., Hofmann, M., Schneider, R., and Youtsos, A. (2009). Statistical analysis of residual stress determinations using neutron diffraction. *International Journal of Pressure Vessels and Piping*, 86(1):48–62.

Withers, P. (2007). Residual stress and its role in failure. *Reports on Progress in Physics*, 70(12):2211–2264.

Withers, P. and Bhadeshia, H. (2001). Residual stress. Part 1 – measurement techniques. *Materials Science and Technology*, 17(4):355–365.

Withers, P. J. (2004). Depth capabilities of neutron and synchrotron diffraction strain measurement instruments. ii. practical implications. *Journal of applied crystallography*, 37(4):607–612.